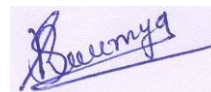


*Dedicated to all my teachers and
beloved family members*

Declaration

I hereby declare that the work embodied in the thesis entitled “**MORPHOLOGICALLY DIVERSE CERIUM OXIDE NANOSTRUCTURES AND NANOFUIDS FOR MULTIFUNCTIONAL APPLICATIONS**” is the result of the investigations carried out by me, at the Materials Science and Technology Division, National Institute for Interdisciplinary Science and Technology (formerly Regional Research Laboratory), CSIR, Thiruvananthapuram, under the supervision of Dr. Swapankumar Ghosh and the same has not been submitted elsewhere for any other degree.



Sree Remya T. S.

Thiruvananthapuram

February 2015



February 2015

Certificate

This is to certify that the work embodied in the thesis entitled “**MORPHOLOGICALLY DIVERSE CERIUM OXIDE NANOSTRUCTURES AND NANOFUIDS FOR MULTIFUNCTIONAL APPLICATIONS**” has been carried out by **Ms. Sree Remya T. S.** under my supervision at Materials Science and Technology Division, National Institute for Interdisciplinary Science and Technology, CSIR, Thiruvananthapuram, in partial fulfilment of the requirements for the award of the Degree of Doctor of Philosophy in Chemistry, under the Faculty of Science, Cochin University of Science and Technology, Thiruvananthapuram and the same has not been submitted elsewhere for any other degree. All the relevant corrections and modifications suggested by the audience at the pre-synopsis viva voce and recommended by the doctoral committee are incorporated in the thesis.

Swapankumar Ghosh

Thesis supervisor
(Former Scientist, NIIST)



Acknowledgements

During the period I have been working for this thesis, a lot of people helped me and supported me in a variety of ways. I am indebted to all of them. Here, I would like to distinguish and express my special thanks.

First of all, I would like to express my appreciation to Dr. Swapankumar Ghosh, my research supervisor, Senior Principal Scientist, CG&CRI, Kolkata-700032 (formerly at NIIST, Thiruvananthapuram) for his constant encouragement, expertise, support and understanding throughout my PhD and his ability to always approach things from a different angle. I especially want to thank him for helping me realise that I have the potential to execute high notch research assignments in Nanotechnology, and for allowing me to learn from him as much as I could. I am always indebted to him.

I am extremely thankful to Dr. Suresh Das, present Director and former Directors of NIIST for providing the facilities to carry out this research work.

I would like to say a special word of thanks to Dr. K. G. K. Warriar for his valuable suggestions and encouragement during the course of my doctoral studies. I also would like to remember with great gratitude Dr. U. S. Hareesh for all the support he has given to me during this study.

I would like to acknowledge the contributions of Ms. Remani K. C. for initial work, Ms. Renjusha Nambiar and Ms. Malini to some of the data presented in this thesis.

I extend my thanks to Dr. S. Shukla, Dr. S. Ananthakumar and Dr. Balagopal N. Nair for their critical suggestions and advices during the course of my work. I am immensely thankful to Mr. A. Peer Mohamed for most of the characterisation presented in this thesis. Thanks are also due to Mr. P. Perumal for his support. I wish to acknowledge all scientists and technical staffs of NIIST for their kind co-operation.

I am indebted to Ms. Asha Krishnan for her invaluable contributions in terms of fruitful discussions, memorable companionship and above all she was always ready to hear my doubts, queries and share my anxieties.

I thankfully acknowledge the contributions of SEM, TEM and XRD groups to this work. I also thank Mr. Krishnan Kartha for the AFM studies.

I always cherish the sincere support and warm friendship of my former colleagues Dr. Shajesh P., Dr. Smitha Sasidharan, Dr. Anas S., Dr. Smitha V. S., Ms. Manjumol K. A. and Dr. Akhil K. Nair which made my days at NIIST memorable. I extend my thanks to Dr. Rony Rajan Paul for his friendship and support.

Ms. Jaimy K. B. requires special mention for the warm friendship and its comfort which has helped in molding the thesis in the final stages. I am thankful to Mr. Mathew

Joy and Ms. Srividhya J. Iyengar for their friendship and support throughout their stay at NIIST.

I wish to thank my present colleagues Mr. Mahesh., Ms. Babitha K. B., Ms. Harsha N., Mr. Manu Jose, Mr. Sankar Sasidharan, Ms. Suyana, Ms. Mega, Ms. Minju Thomas, Ms. Swetha S., Ms. Sumina, Ms. Subha P. V., Ms. Shijina, Mr. Midhun Mohan, Mr. Firoz Khan, Mr. Arun and Dr. Seethalekshmi Sunil. In different ways, their support has been crucial for the completion of the thesis, and their humour and friendship have made working at NIIST very enjoyable. I also thank other group members Mr. Sujith S., Mr. Vaisakh S. S., Mr. Balanand Santhosh, Mr. Reymond Rozario, Ms. Linsha V., Ms. Soumya S., Ms. Jeen Maria Mathews, Ms. Minju N. and Ms. Suhailath K. A. for their support.

I wish to remember Mr. Mirash, Mr. Divish and Mr. Senguttuvan for their support during the initial stages of this work. I would also like to thank Ms Salini P. S., Ms. Derry Holaday, Ms. Aiswarya, Ms. Vidya Kattoor, Ms. Anaswara, Ms. Mini, Ms. Dhanya and Ms. Cincy for their warm friendship during my stay at NIIST.

I acknowledge the Council of Scientific & Industrial Research, New Delhi, for the Research Fellowship and Financial assistance from the IRELTDC and the BHEL.

Finally on a personal note, I remember with gratitude my parents for all their support and I am very thankful that they were always there for me. Finally, to my best friend and husband, Sreejesh K. V. for always believing in me and supporting me in everything I do. Without you by my side, I could not have completed this. At this moment I would also like to remember Nivedhitha, my dearest daughter who missed my presence and affection during the final stages of my thesis.

*Above all I bow before '**The Almighty**' for his immense blessings.*

Thiruvananthapuram
26/02/2015

Sree Remya T. S.

CONTENTS	PAGE
Declaration	i
Certificate	ii
Acknowledgements	iii
Contents	v
Preface	ix
Abbreviations	xvi
Chapter 1 Introduction to Nanotechnology, Cerium dioxide and its Functional Applications	1-53
1.1 Nanotechnology	1
1.2 Cerium dioxide (CeO ₂)	2
1.2.1 Structure of cerium dioxide	3
1.2.2 Variable oxidation state /Mixed valence in ceria	4
1.2.3 Oxygen storage capacity of ceria	6
1.3 Significance of size/shape controlled synthesis	8
1.3.1 Synthesis of ceria nanoparticles	8
1.3.1.1 Precipitation method	9
1.3.1.2 Hydrothermal / Solvothermal method	11
1.3.1.3 Surfactant assisted synthesis	14
1.3.1.4 Other methods	16
1.4 Various applications of cerium dioxide	19
1.4.1 Glass polishing	20
1.4.1.1 Chemical Mechanical Polishing (CMP)	22
1.4.2 Ceria nanocatalysts	26
1.4.2.1 Combustion of particulate matter	27
1.4.2.2 Factors affecting catalysis	29
1.4.3 Nanofluid	34
1.4.3.1 The concept of nanofluids for thermal management	36
1.4.3.2 Oil based heat transport fluid	37

1.4.3.3	Hydrophobic modification of NP surface	39
1.5	Scope of the present thesis	40
1.6	References	42
	Definition of the present problem	52
Chapter 2	Architecture tuned synthesis of cerium oxide nanoparticles and application in chemical mechanical polishing of glass	54-83
2.1	Abstract	54
2.2	Introduction	56
2.3	Experimental	59
2.3.1	Synthesis	60
2.3.2	Slurry preparation	62
2.3.3	Surface treatment of microscopic glass	62
2.3.4	Polishing study on glass substrate	62
2.4	Results and discussion	63
2.4.1	Electron microscopy	63
2.4.2	X-Ray diffraction analysis	65
2.4.3	Dispersant optimization and stability of slurry	66
2.4.4	Polishing studies on glass	67
2.4.4.1	Surface treatment of microscopic glass	67
2.4.4.2	Characterization of polished glass surface	68
2.4.5	Role of Ce ³⁺ /defects: XPS and Raman spectral analysis	71
2.4.6	Mechanism of glass polishing	73
2.4.7	Hydrophilicity of nanoabrasives	74
2.4.8	Effect of solid content of abrasive	77
2.4.9	Effect of pH of slurry	78
2.5	Conclusions	80
2.6	References	81

Chapter 3	Morphology dependant catalytic activity of cerium oxide nanoparticles in high temperature oxidation	84-115
3.1	Abstract	84
3.2	Introduction	85
3.3	Experimental section	88
3.3.1	Synthesis	88
3.3.2	Catalytic activity tests	89
3.3.3	Oxygen Storage Capacity Measurements	90
3.3.4	Temperature Programmed Reduction using H ₂ (H ₂ -TPR)	90
3.4	Results and Discussion	90
3.4.1	Primary sample characterisation	90
3.4.2	Detailed X-ray diffraction analysis	92
3.4.3	Electron microscopy	95
3.4.4	XPS and Raman spectral analyses	100
3.4.5	Overview of physical properties	103
3.4.6	Catalytic activity evaluation	105
3.4.6.1	Diesel soot oxidation	105
3.4.6.2	From H ₂ -TPR profiles of ceria nanocatalysts	110
3.5	Conclusions	112
3.6	References	113
Chapter 4	Cerium oxide based nanofluid as efficient coolant in transformers - A comparative study with alumina and zirconia	116-162
4.1	Abstract	116
4.2	Introduction	118
4.3	Experimental	121
4.3.1	Preparation of metal-oleates (M-oleates, M=Ce, Al and Zr)	122
4.3.2	Reflux synthesis of surface modified nanocrystals	122
4.4	Results and discussions	123
4.4.1	Characterisation of precursor oleates	123
4.4.1.1	IR spectral investigation of precursor oleates	123

4.4.2	Thermogravimetric analysis of surface modified NPs	124
4.4.3	Ceria fluid	126
4.4.3.1	Powder characterisation	126
4.4.3.2	Mechanism of thermolysis	130
4.4.3.3	Rheological properties of nanofluids	132
4.4.3.4	Thermal Conductivity of Nanofluids	134
4.4.4	Alumina Nanofluid	136
4.4.4.1	Powder characterisation	137
4.4.4.2	Formation mechanism	142
4.4.4.3	Viscosity measurements	143
4.4.4.4	Thermal Conductivity of Nanofluids	144
4.4.5	Zirconia nanofluid	146
4.4.5.1	Powder characterisation	147
4.4.5.2	Rheological Properties of Nanofluids	150
4.4.5.3	Thermal Conductivity of Nanofluids	152
4.4.6	Stability of nanofluid systems	154
4.4.7	Compilation of data on selected samples	156
4.5	Conclusions	157
4.6	References	159
	Instrumental methods	163-172
	Summary of investigation	173-178
	List of publications	179-180

Preface

The prospective impact of nanomaterials in science and technology has followed an increasing trend due to their unique chemical and physical properties compared to bulk. Significant advances in current technologies in areas such as clean energy production, electronics, medicine, and environment have fuelled major research and development efforts in nanotechnology around the world. This leads to the opportunity to use such nanostructured materials in novel applications and devices. Ceria, zirconia, alumina and titania are some of the major oxides which find vast applications as a nanomaterial on a wider side.

Cerium oxide (CeO_2) commonly known as ceria, is one of the most important and abundant rare-earth materials possessing stable face-centred cubic fluorite-type crystal structure. Nanoscale cerium oxide has many properties which make them attractive materials in applications such as direct electrochemical oxidation of methane in solid oxide fuel cells, oxygen sensing/ storage, UV absorbent, as oxidation catalyst in automobile exhaust and in glass-polishing. Most of the applications are derived from the facile conversion of Ce^{4+} to Ce^{3+} and vice versa which endows it with a high oxygen storage capacity (OSC). The fundamental structures of the ceria nanomaterials appear to constructively dominate their properties and applications. The redox activity of the cerium ions, and the possibility of tuning the physical and chemical properties through doping or by varying grain size and shape make CeO_2 attractive for easy adaptation as in the case of catalysts where the crystallite size, the presence and number of oxygen vacancies and the resulting lattice strain are critical. The shape of CeO_2 nanocrystals is

correlated with the predominance of particular crystal facets which exhibit selective reactivity in different catalytic processes. Hence methods that give control over crystal shape may provide a means to understand and optimize the catalytic activity. This makes size and shape selective synthesis of ceria nanostructures important. However, creating these favorable defects and understanding their roles in the reducibility and activity of nanosized ceria at the atomic level is still lacking.

The surface modification of nanoparticles is another interesting area of research which produces monodisperse nanoparticles of desired size and shape by proper tuning of synthetic conditions. By attaching suitable surfactants on nanoparticle surface, the dispersibility of nanoparticles in various solvents can be tailored. However, the applications of surface modified ceria nanoparticles have scarcely been reported.

The present thesis addresses the size and shape selective synthesis of ceria nanoparticles by facile ammonia precipitation and hydrothermal methods, all starting from the cerium nitrate hexahydrate as precursor. The crystal morphology dependent polishing efficiency of ceria nanoparticles in glass polishing and catalytic activity in oxidation reaction were studied in detail. A simple reflux method was adopted for the synthesis of surface modified oleophilic/hydrophobic ceria nanoparticles. The surface modified ceria nanoparticles were further utilised for the preparation of stable nanofluids in transformer oil. The suitability of the nanofluids in heat transport was evaluated by measuring the colloid sizes, the stability, viscosity and the thermal conductivity of the nanofluid. The rate of heat transfer of the ceria nanofluid was further compared with alumina and zirconia fluids prepared by a similar reflux procedure, possessing highest and lowest material thermal conductivity among ceramic oxides respectively.

The thesis contains four chapters in total. The first chapter provides introduction to nanomaterials, nanocrystalline ceria and its applications in a broad way. A brief and updated literature review on ceria nanoparticles, with special emphasis on size and shape selective properties and its multi functional applications are covered. Various synthetic procedures adopted for the synthesis of ceria nanoparticles are described in detail. Based on critical assessment of the reported information, the present research problem has been defined.

The second chapter describes architecture tuned synthesis of ceria nanoparticles of rod+cube, cube and spherical shape by hydrothermal and ammonia precipitation methods respectively. The hydrothermal temperature and base concentration were found to be the key parameters that determine the morphology of the crystal produced. The ceria nanoparticles of different morphology thus obtained have been characterised in detail using X-ray diffraction, BET surface area, transmission electron microscopy, X-ray photoelectron spectroscopy, Raman spectra and powder contact angle measurements. Aqueous slurry of the prepared nanoparticles, stabilised using carboxy methyl cellulose was further utilised for polishing silicate glass with an initial average surface roughness of ~40 nm. The surface roughness of the polished glass substrates was characterised using Atomic Force Microscopy (AFM) and profilometry. The mixed morphology of ceria rod and cube was found to be very effective in polishing glass by reducing the initial surface roughness from 40 to 3 nm in 10 minute polishing. Polishing efficiency of the nanopowders was compared with a commercial ceria abrasive used in glass polishing industry under identical conditions. Important parameters such as morphology of abrasive, solid content of slurry, pH of medium, etc. needed for achieving nanolevel

polishing were optimised. The efficiency of the abrasives in terms of surface quality followed the order Rod+Cube > Cube > Spheres > Commercial ceria. The amount of Ce^{3+} in the abrasive was found to vary with the morphology of the abrasive as evidenced by XPS and was found to be 42.1, 31.4 and 22.2% in rod+cube, cube and spheres respectively. More Ce^{3+} on the surface of abrasive in slurry was found to be beneficial for the polishing process due to the ease of forming a $Ce(OH)_3$ hydration layer which would accelerate the process of polishing. The hydrophilicity of the powders was evaluated by dynamic water contact angle measurements as it is known that chemical reaction at a liquid–solid interface depends on their contact angle. The contact angle value was found to be 60° , 79° , 87° and 90° in the case of rod+cube, cube, sphere and commercial ceria respectively. This variation in contact angle is due to i) change in morphology ii) which in turn change $[Ce^{3+}]$ and iii) predominance of polar 200 surface. The mixed morphology of rod+cube containing $\sim 42\%$ Ce^{3+} , and powder contact angle of 60° was found to be the best for polishing. An optimum solid content of 5 wt% of abrasive and a slurry pH of 10 was found to be essential for achieving nanolevel smoothness. The improved polishing efficiency in alkaline media may be due to a simultaneous chemical etching which involves the hydrolysis of the glass surface. Hydroxyl radicals break the O–Si–O bonds on the glass surface and form relatively weaker Si–OH bonds. The removal of this weakened film surface through abrasion is relatively easy. So the pH of the slurry plays an important role in nanolevel polishing of glass substrates.

The third chapter describes morphology dependent catalytic activity of nanoceria. Ceria nanoparticles of different morphology were synthesized by the same procedure adopted in chapter two except that concentration of precursor was decreased from 0.5 to

0.05 M. Lowering the precursor concentration was found to decrease the particle size which in turn increased the specific surface area of the product. The effect of morphology and BET surface area of fine CeO₂ nanocrystals on catalytic activity were investigated by diesel soot combustion and temperature-programmed reduction (TPR) with H₂. The peak temperature during carbon combustion in presence of CeO₂ catalyst is expressed as one of the indices of catalytic activity. The reduction temperature of the catalysts in H₂-TPR is a prominent index of catalytic activity. The soot oxidation temperature of various nanocatalysts decrease in the order commercial CeO₂ > sphere > cube > rod+cube. To understand the morphology dependent catalytic activity, the nanopowders were characterised in detail using XRD, TEM, XPS, Raman spectroscopy and thermogravimetry. Catalytic activity of CeO₂ crystals of different shapes have been correlated to the “texture coefficient” (an index of active crystal planes) estimated from XRD of the nanopowders. The defects /oxygen vacancy in the nanopowders due to the presence of Ce³⁺ as evidenced by XPS and Raman spectral analysis was found to be one of the key parameters that determine catalytic activity. A mixed morphology catalyst comprising of nanorods and nanocubes was found to be more effective in soot oxidation when compared to that of a commercial ceria powder. This catalyst could lower the soot oxidation temperature by ~165°C. The enhanced activity of mixed morphology catalyst was due to the predominance of highly active crystal facets {(200) and (220)} and ~44% of Ce³⁺ in the sample. CeO₂ possesses a high oxygen storage capacity (OSC) because of the rapid formation and elimination of oxygen vacancy defects in it. The higher Ce³⁺ concentration ensuing in defects and exposure of more reactive (100) surfaces, followed by (110) surfaces, can facilitate the formation of oxygen vacancies in them and introduce

enhanced OSC in the crystal. The OSC results determined by thermogravimetry follow an order rod+cube > cube > spherical > commercial ceria. The highest value obtained was 420.6 $\mu\text{mole O}_2/\text{g}$ for rod+cube. A remarkable feature which makes the mixed morphology catalyst promising candidate in high temperature oxidation is that they offer better catalytic activity even after thermal ageing at a high temperature of $\sim 1000^\circ\text{C}$.

The fourth chapter describes preparation of surface modified ceria nanoparticles and its subsequent application as a heat transport fluid in transformers. Heat transport driven failures are quite often in high voltage power transformers. Dielectric oils in these transformers provide efficient cooling extending its life. These transformer oils require excellent nanoparticle (NP) dispersion, high heat conduction, with simultaneous electrical insulation. The surface modification of the nanoparticle is a prerequisite to make it compatible with the transformer oil and also to prevent the aggregation of the nanoparticles due to their high surface energy leading to precipitating out of the suspension. Surface modified oleophilic ceria nanoparticles were prepared by a reflux method in presence of oleic acid which was easily dispersed in transformer oil for the preparation of stable nanofluids. The suitability of the nanofluids thus obtained as heat transfer fluid was evaluated by measuring the stability of nanofluids, thermal conductivity, viscosity and particle size. The effect of particle loading and temperature on the thermal conductivity of the oil based nanofluids was studied. Oil-based nanofluids containing ceria nanoparticles showed shear-thinning behavior and produced $\sim 14.6\%$ enhancement in thermal conductivity at 50°C with 0.7 vol% nanoparticle loading. A comparative study was performed with alumina and zirconia nanofluids prepared by a similar method. The thermal conductivity enhancement followed the order alumina >

ceria > zirconia. The lower processing time (4 h reflux) and low viscosity of ceria nanofluid compared to that of alumina makes it a much better candidate in heat transport application.

In summary, cerium dioxide nanostructures of different morphology is successfully synthesized by precipitation method followed by hydrothermal treatment and were found to show morphology dependent properties in applications such as glass polishing, and oxidation catalysis of particulate matter (soot). Surface modified ceria nanoparticles were prepared using a solvothermal method and subsequently phase transferred into apolar solvents for the preparation of stable nanofluids/coolant. The efficacy of the nanofluids was evaluated by measuring thermal conductivity enhancement, viscosity and stability.

Abbreviations

AFM	Atomic Force Microscopy
AP	Ammonia Precipitated Ceria
BET	Brunauer Emmett Teller
CC	Commercial Ceria
Ce	Cerium
CMC	Carboxy Methyl Cellulose
CMP	Chemical Mechanical Polishing
CN	Cerium nitrate hexahydrate
CRT	Cathode Ray Tube
CTAB	Cetyl trimethyl ammonium bromide
DTA	Differential thermal analysis
FFT	Fast Fourier Transform
FT-IR	Fourier Transform Infrared Spectroscopy
HT1	Hydrothermally synthesized ceria at 120°C
HT2	Hydrothermally synthesized ceria at 180°C
IEP	Isoelectric point
IUPAC	International Union of Pure and Applied Chemistry
LCD	Liquid Crystal Display
NP's	Nanoparticles
OA	Oleic acid
OSC	Oxygen Storage Capacity
PCS	Photon correlation spectroscopy
PDI	Polydispersity Index
PEG	Polyethylene glycol
PIS	Precipitant Into Salt
PVP	Polyvinylpyrrolidone
SEM	Scanning Electron Microscopy
SIP	Salt Into Precipitant
TBAB	Tetrabutylammonium bromide
TC	Thermal Conductivity
TEM	Transmission Electron Microscopy
TGA	Thermogravimetric Analysis
TWCs	Three-way catalysts
T _p	Peak temperature
TPR	Temperature Programmed Reduction
WGS	Water Gas Shift reaction
XPS	X-Ray Photoelectron Spectroscopy
XRD	X-ray Diffraction

Introduction to Nanotechnology, Cerium dioxide and its Functional Applications

1.1 Nanotechnology

Nanotechnology was first introduced in the famous lecture of Nobel laureate Richard P. Feynman, “There’s Plenty of Room at the Bottom”, given in 1959 at California Institute of Technology. Literally, nanotechnology means the technology performed at nanoscale that has major implications in real world. The concept of nanostructured materials has its origin in physics and dates back 30 years approximately. Nanostructured materials are defined as being assembled of ultra fine particles with a dimension below 100 nm. They exhibit properties that are usually rather different to those of bulk materials and their local solid-state structure is often of prime importance. Significant advances in current technologies and the potential for more revolutionary impacts in areas such as clean energy production, electronics, medicine, and environment have fueled major research and development efforts in nanotechnology around the world. The prospective impact of nanomaterials in science and technology is high, and stems from their unique properties, such as novel optical, chemical, mechanical, magnetic and electrical properties. These properties can be controlled by engineering the size, morphology and composition of the particles. Further such novel properties of the nanoparticles (NP’s) can be exploited and combined to allow industries to re-engineer and enhance existing products and to develop novel and innovative products that function at unprecedented levels. This leads to the opportunity to use such nanostructured materials in novel applications and devices.

In the family of inorganic oxides, ceria, zirconia, alumina, zinc oxide and titania are some of the major ceramic oxides which find vast applications as nanomaterials. The high abundance, low cost and vast applications are some of the noteworthy characteristic features which make ceria attractive for academic and industrial people. Other notable quality of CeO₂ which has not been claimed in many other semiconducting materials is the simplicity in its fabrication into 1, 2 and 3-dimensional nanostructures.^[1] Worldwide many research groups were actively involved in the basic to advanced research in CeO₂, including the theoretical simulations for understanding the mechanism involved in the growth of various morphologies, related physico chemical characteristics and its device fabrication. The present thesis is focused on the synthesis of ceria nanostructures of diverse morphology and its subsequent application in glass polishing and oxidation catalysis. Further, an attempt was made to adopt surface modified oleophilic ceria nanoparticles prepared by a facile reflux technique in heat transport fluid. In the succeeding sections, special emphasis is given to discuss the structure, physico-chemical properties, processing techniques and some of the potential applications of this magnificent inorganic oxide.

1.2 Cerium dioxide (CeO₂)

First isolated as an impure oxide in 1803, the element was named after the earliest recognized asteroid 'Ceres' that in turn was named for the patron saint of Sicily, the Roman goddess of food plants. It is found in a number of minerals, the most important being monazite and bastnasite.^[2] Important deposits of monazite are located in the US, Australia, Brazil, India, and South Africa. Among the rare earth family, cerium (Ce) is the most abundant element in the Earth's crust ~66.5 ppm.^[3] Cerium is the most attractive

rare earth to researchers especially in the field of catalysis. Cerium possess an electronic configuration of $[\text{Xe}]4f^26s^2$ with two common valence state Ce^{4+} and Ce^{3+} and can flip-flop between these two oxidation states in a redox reaction. This is partially due to the similar energy of the 4f and 5d electronic states and low potential energy barrier (1.72 eV) to electron density distribution between them.^[3, 4] Interestingly it is the only rare earth element that can be easily separated from a mixture of other rare earth elements by simple chemical methods.

With a high abundance, cerium oxide (CeO_2) is a technologically important material due to its wide applications as a promoter in three-way catalysts (TWCs) for the elimination of toxic automobile-exhaust gases, low-temperature water-gas shift (WGS) reaction, oxygen sensors, oxygen permeation membrane systems, fuel cells, glass-polishing materials, electrochromic thin-film application, ultraviolet absorbent, as well as in biotechnology, environmental chemistry, and medicine.^[3]

1.2.1 Structure of cerium dioxide

Ceria is a pale yellow colour solid due to $\text{O}^{2-} \rightarrow \text{Ce}^{4+}$ charge transfer and is known to crystallize in fluorite structure (CaF_2) with a space group of $Fm\bar{3}m$. The unit cell of ceria is shown in Fig.1.1. In the face centred cubic (FCC) structure of ceria, Ce^{4+} ions form a cubic close packing arrangement and all the tetrahedral sites are occupied by the oxide ions whereas the octahedral sites remain vacant.

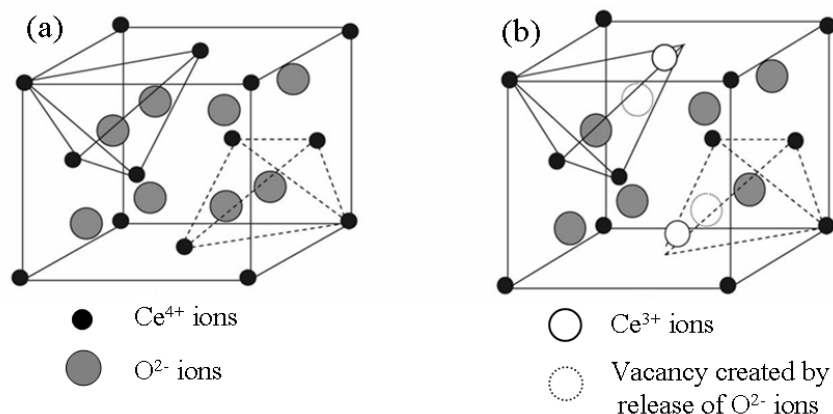


Fig. 1.1 (a) Cartoon diagram of bulk ceria crystal structure showing intact CaF₂ structure and (b) Distorted crystal structure of nanoceria due to oxygen vacancy creation and replacement of Ce⁴⁺ ions by Ce³⁺ ions.

The structure of cerium oxide is well documented in the literature.^[5, 6] Cerium oxide NPs (also known as nanoceria) can act as excellent oxygen buffers, due to their redox capacity.

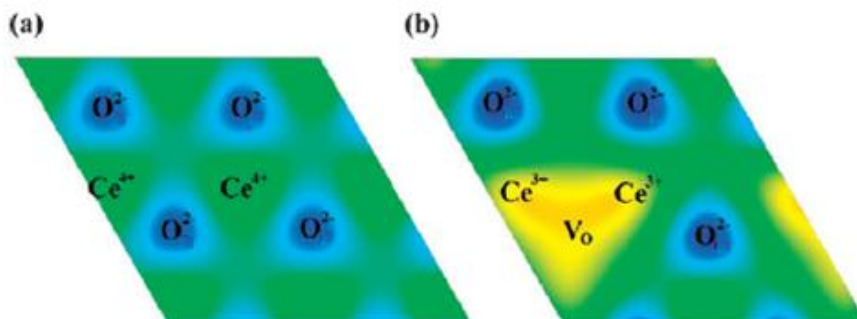


Fig. 1.2 Schematic diagram showing the formation of oxygen vacancy (V_o) in (a) pure CeO₂ and (b) CeO_{2-γ} in which some of the Ce⁴⁺ changed to Ce³⁺.

The ionic radius of Ce³⁺ (1.034 Å) is higher than that of Ce⁴⁺ (0.92 Å). Hence the introduction of the oxygen vacancies and the associated Ce³⁺ ions leads to a distortion of the local symmetry. Oxygen vacancy formation is demonstrated in Fig. 1.2. This causes the change in the Ce–O bond length (lattice distortion) and the overall lattice parameter.

1.2.2 Variable oxidation state /Mixed valence in ceria

While CeO_2 is the stable form of bulk cerium oxide, ceria NP's exhibit a nonstoichiometric composition, $\text{CeO}_{2-\gamma}$ (Fig. 1.2b), due to the presence of oxygen vacancies and the formation of Ce_2O_3 at the grain boundaries. The Ce^{3+} ions, which are more reactive and therefore more desirable for various applications, are created by oxygen vacancies, which act as defects in the $\text{CeO}_{2-\gamma}$ crystal lattice. Most of the applications of nanoceria are related to the rapid formation and elimination of oxygen vacancy in CeO_2 that endows it with a high oxygen storage capacity (OSC). The valence of cerium (Ce) and the resultant defect structure of cerium oxide are dynamic and may change spontaneously or in response to physical parameters like temperature, presence of other ions, and oxygen partial pressure. Based on theoretical calculations it has been suggested that, the segregation of Ce^{3+} species to the surface is driven by a change in the oxidation enthalpy.^[7, 8]

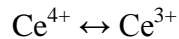
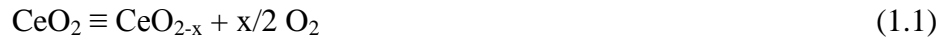
Table 1.1 Some physical properties of pure stoichiometric ceria.^[3]

Property	Value/unit
Molar mass	172.12 g.mol ⁻¹
Lattice parameter	5.41 Å
Density	7.22 g.cm ⁻³
Melting point	2750 K
Boiling point	3773 K
Solubility in water	Insoluble
Thermal conductivity	12 W.m ⁻¹ .K ⁻¹
Hardness	5-6
Electronic conductivity	2.48×10 ⁻⁸ S.cm ⁻¹
Refractive index	2.1 (visible) 2.2 (infrared)

Again, thermodynamic measurement suggests that this remarkable stability of the surface 3+ oxidation state occurs because the partial molar entropy of oxygen of the reduced surface is larger than that of the oxidized bulk. The combined high concentration and stability of the reactive Ce^{3+} species strongly suggests that the surface's significantly altered redox thermodynamics plays a decisive role in the high activity of ceria-based oxides.^[8] Some of the important physical properties of CeO_2 are listed in Table 1.1.^[3]

1.2.3 Oxygen storage capacity of ceria

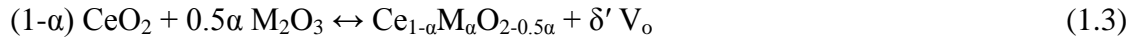
The ability of the cerium ion to switch between the Ce^{4+} and Ce^{3+} oxidation states depending on the ambient oxygen partial pressure is represented as:



The amount of oxygen released in the forward reaction and the oxygen consumed in the reverse reaction is generally referred as the oxygen storage capacity (OSC) of ceria material.^[5, 9, 10] It is worth recalling that of the two processes (reduction/oxidation), oxidation is fast,^[11] and occurs deep into the bulk even at room temperature (RT), whereas reduction typically occurs above 473 K.^[12] Thermally induced defects can be broadly categorized into two, one cationic type ($\Delta E = 11.11$ eV) and the other anionic type ($\Delta E = 3.2$ eV). From variation in ΔE , it is evident that the predominant defect category is the anion type, which leads to the formation of pairs of oxygen vacancies.^[13] According to Cho, two types of oxygen vacancies can be created in ceria namely, intrinsic and extrinsic.^[14] Intrinsic vacancies are created on reduction of ceria according to the following process (equation 1.2).



Extrinsic vacancies are defects that are formed by a charge-compensating mechanism when a bivalent or trivalent cation M is introduced into the CeO₂ lattice according to these two mechanisms (equations 1.3 and 1.4), where δ' and δ'' are the created extrinsic oxygen vacancies in the modified ceria:



The oxygen storage capacity of ceria can be benefited from either type of defect. Two types of measurements of OSC were distinguished by Yao and Yu Yao.^[15] The so-called complete or ultimate oxygen storage capacity (total OSC), i.e., an oxygen storage measured under thermodynamic control, and the kinetic oxygen storage, (dynamic OSC), i.e., measured under kinetic control. The total OSC represents the widest 'limiting' amount of oxygen transferable from the catalyst at a given temperature and generally is limited in the case of CeO₂ by the formation of some non-stoichiometric CeO_{2-x} compounds. The capability of CeO₂-based materials to release/absorb oxygen at the catalytic site is perhaps a better description of this OSC functionality, where spillover properties, creation and annihilation of oxygen vacancies and complex network of reaction/interactions play a vital role. Oxygen diffusion in ceria and related systems is of interest for several reduction and oxidation reactions. The rate of several catalytic oxidation reactions which occur anaerobically, i.e., without oxygen from the gas phase, but using oxygen from the solid, depends on oxygen diffusion parameters.

1.3 Significance of size/shape controlled synthesis

The surface oxygen mobility through the lattice of the ceria is treated as an oxygen buffer and provides ceria an ultimate choice for an application based on the enhancement of the electrochemical phenomenon. In addition, enchantment of the oxygen mobility also varies with particle size and shape of the nanostructures. From the very beginning of nanomaterial research, it has been recognized that the size of the components is controllable. Additionally, shape and structure differences are attractive for several activities. The catalytic activity of many materials has been observed as structurally sensitive. Therefore, several industrially important reactions, including low-temperature CO oxidation, UV absorption, partial oxidation of hydrocarbons, hydrogenation of carbon oxides, and waste water treatment, are exclusively affected by the structure of the nanomaterials.

1.3.1 Synthesis of ceria nanoparticles

Since Matijevic et al. first reported the preparation of polycrystalline CeO₂ colloids by forced hydrolysis of cerium salts in 1988,^[16] various techniques or synthetic routes have been developed for obtaining CeO₂ nanocrystals with varying morphologies and sizes. The methods include hydrolysis,^[17] precipitation,^[18-20] thermal deposition,^[21] combustion or flame-synthesis,^[22, 23] sol-gel,^[24] hydrothermal or solvothermal,^[25, 26] microemulsion,^[27, 28] gas condensation,^[29] sonochemical,^[30] electrochemical techniques^[31] and so on. From the published literature, it is established that the fundamental structures of the ceria nanomaterials constructively dominate their properties and applications. This makes size and shape selective synthesis of ceria nanostructures important.

1.3.1.1 *Precipitation method*

Owing to the advantages of simple process, easy scale-up and low cost, the aqueous precipitation technique has attracted the most extensive attentions.^[32] In a typical precipitation procedure, oxide powders or their precursors are obtained by adding a ligand, say ammonia, directly to a solution containing metal cations. An insoluble salt is precipitated once its solubility limit is exceeded. For example, Zhou et al. produced CeO₂ particles of about 4 nm from cerium nitrate and ammonia.^[33] Matijević and Hsu prepared sub-micron Ce₂O-(CO₃)₂H₂O particles from the reaction of cerium nitrate with urea.^[34] Chen and Chen prepared CeO₂ particles from cerium nitrate with hexamethylenetetramine,^[35] whereas Li et al. used ammonium carbonate and diethylamine as the precipitating agents.^[36] Yamashita et al. produced CeO₂ particles from cerium chloride and sodium hydroxide with the presence of hydrogen peroxide under various pH conditions from 6 to 12.^[37] Uekawa et al. obtained 7–9 nm CeO₂ particles starting from cerium nitrate in the polyethylene glycol solution.^[38]

Nucleation and growth

Growth of bulk- or nanometer-sized crystal structures of different dimensions is inherently related to the process of precipitation of solid phase from solution. Simultaneous process of nucleation followed by growth phenomena governs the crystal morphology (including the size and shape) in the precipitation reaction. At the initial stage, numerous small crystallites are formed. Consequently, the small crystallites are aggregated together to form thermodynamically stable structures and this is referred to as a growth process.^[39] An effective process control leads to the formation of the desired crystal structure. Initially, surface energy plays an important role to increase the size of

the nuclei by lowering the surface free energy where nucleation is a spontaneous process. Nucleation process is readily involved in heterogeneous nucleation, secondary nucleation and homogeneous nucleation. Presence of suspended particles may provide the start of the nucleation, and thus insists the heterogeneous nucleation with the requirement of less energy. Heterogeneous nucleation occurs more often than homogeneous nucleation. Secondary nucleation is involved in the formation of nuclei with the recombination of existing crystal.^[39] On the other hand, homogeneous nucleation occurs spontaneously and randomly in the absence of solid interface by a combination of solute molecules. The growth process of crystal occurs for dissolving the solute in the solution at higher temperatures and then cooling to low temperature or by adding the necessary reactants to produce a supersaturated solution during the reaction. This overall crystal growth phenomenon occurs by the consumption of smaller particle by larger particle to form still larger stabilized structures. This growth process is referred to as Ostwald ripening, also known as coarsening. Lifshitz and Slyozov first developed mathematical derivation for the Ostwald ripening process and independently by Wagner; their combined models today are referred to as LSW theory. Nuclei formation that precedes crystal growth can occur by solid-state restructuring of the gel or precipitation from the supersaturated solution.^[40]

Homogeneous precipitation

In the precipitation process, if the ligand, and hence precipitates, are generated simultaneously and uniformly throughout the solution, then the process is termed as a homogeneous precipitation method.^[35] Precipitation from homogeneous solution can be done in two different ways namely SIP (salt into precipitant) and PIS (precipitant into

salt). Zhou *et al.* reported that feeding the cation solution into the precipitant, the SIP process, resulted in the finest size and least agglomeration.^[41] They have explained the same in terms of the initial pH of the reaction medium. In the case of PIS, the pH value in the reactor will be initially very low (pH 3.8-4.3 for the cerium nitrate solution), and increase rapidly with just a few drops of ammonium hydroxide to a value of 7.2. The solubility product of $[\text{Ce}^{3+}][\text{OH}^-]^3$ is less than the critical solubility constant of $\text{Ce}(\text{OH})_3$, which is $\sim 7 \times 10^{-21}$. Under these conditions, though a nucleus may form at the interface, it is in an unstable state because of the low pH value of the bulk solution. During the SIP process, the pH value always remains higher than 9 (i.e., $[\text{OH}^-]$ higher than 10^{-5} mol/L).^[41] Under these basic conditions, the solubility product is much higher than the solubility constant, meaning the supersaturation value, $S = [\text{Ce}^{3+}][\text{OH}^-]^3/K_{\text{sp}}$, is very large. This results in homogeneous nucleation. Compared to other methods this is more favourable because of inexpensive salt precursors, simple operation and mild synthetic conditions.^[42] The preparation of nanocrystalline CeO_2 by precipitation has received considerable attention because it is the simplest experimental approach and is therefore well-suited to large scale production.^[32]

1.3.1.2 Hydrothermal / Solvothermal method

A proper control over morphology, crystal size and dispersability in various solvents is possible through the use of surface modifiers/ surfactants during synthesis. However, a negative aspect of using such chemical additives is the limited use of as-synthesized NP's in applications that require clean CeO_2 surfaces with maximum reactive sites. In such instances, surfactant and template free routes like hydrothermal method is highly appreciated.

The hydrothermal process is generally performed in an autoclave at temperatures between the boiling and critical points of water (100 to 374°C). In a sealed vessel (bomb, autoclave, etc.), solvents can be brought to temperatures well above their boiling points by the increasing autogenous pressure resulting from heating. Performing a chemical reaction under such conditions is referred to as hydrothermal processing or, solvothermal processing in the case of nonpolar solvents.^[43] In addition, during the solvothermal treatment, the pressure in the autoclave can be readily adjusted to some extent by using various solvents, which have varying vapor pressure at a given temperature. For instance, at 100°C, the pressures in the autoclave when water and ethanol are used as the solvents are about 1.0 and 2.5 kg cm², respectively, as the temperature is elevated to 180°C, the corresponding pressures reach about 10 and 20 kg cm², respectively.^[44]

During this synthesis, the reaction equilibrium of the aqueous metal salt solution changes with temperature, which results in the formation of metal hydroxide or metal oxides. During the heating up period, above reaction takes place to produce monomers, followed by nucleation and crystal growth. Because of the variation of the equilibrium with temperature, particles formed at lower temperatures dissolve again to re-crystallize at higher temperatures during the heating up period or the ageing period at a constant temperature. Therefore, it takes a long time to obtain the crystals of equilibrium composition by this method.

Advantages of hydrothermal method

1. As a robust technique, hydrothermal/solvothermal synthesis has extraordinary advantages of single step low temperature synthesis, superior composition and

morphological control, and powder reactivity over the other techniques in preparing lowly aggregated and highly crystallized nanomaterials.^[45]

2. The product powders have excellent homogeneity and particle uniformity.
3. Ability to create crystalline phases which are not stable at the melting point.
4. Materials which have a high vapor pressure near their melting points can also be grown by the hydrothermal method.
5. The method is also particularly suitable for the growth of large good-quality crystals while maintaining good control over their composition.

Hence hydrothermal treatment has been regarded as one of the most effective and economical routes for nanocrystal synthesis.

Tani *et al.* studied the effect of mineralizers on the crystal growth of CeO₂ under hydrothermal conditions at 500–600°C and 100 MPa.^[46] Further, the studies performed by Hirano and Kato in 1996 has shown that controlling the growth of CeO₂ particles was possible, and ultrafine ceria particles could be hydrothermally prepared from Ce(IV) sources.^[47] Inoue *et al.* prepared a colloidal solution of 2 nm ceria particles by oxidation of cerium metal in 2-methoxyethanol under solvothermal condition.^[48]

Recent studies in CeO₂ system have focused on the development of robust synthetic approaches toward size/shape-controlled nanostructures e.g., dots, rods, wires, and tubes and the investigation of their size/shape-dependent properties.^[49, 50] CeO₂ nanowires/rods first synthesized by using hard templates, such as porous anodic alumina membranes.^[51, 52] CeO₂ nanorods were also prepared by solvothermal methods.^[53-55] Large-scale well-crystallized CeO₂ nanorods with uniform diameters in the range of 20–30 nm and lengths up to tens of micrometers are first synthesized through a

hydrothermal route in 5 M KOH solution at 180°C for 45 h without any templates and surfactants. The nanorod formation involves dehydration of CeO₂ NP's and orientation growth along the <110> direction in KOH solution. Subsequently, gold NP's with crystallite sizes between 10 and 20 nm are loaded on the surface of CeO₂ nanorods using HAuCl₄ solution as the gold source and NaBH₄ solution as a reducing agent. The synthesized Au/CeO₂ nanorods demonstrate a higher catalytic activity in CO oxidation than the pure CeO₂ nanorods.^[56]

Single-crystalline CeO₂ nanocubes were synthesized through a hydrothermal treatment. By varying reaction temperature and the alkali concentration, the size control of CeO₂ nanocrystals has been achieved, which produces the nanocubes with a controllable edge length in the 20–360 nm regime. HRTEM studies reveal that the CeO₂ nanocubes expose their high energy {001} planes.^[45] Pan *et al.* hydrothermally synthesized ceria nanoplates, tubes and rods in the presence of CTAB as surfactant.^[57] Consequently, it is demonstrated that the CeO₂ nanocubes exhibit excellent reducibility and high oxygen storage capacity, indicating they are potential novel catalytic materials.^[58] The literature survey indicates that the product powders can be controlled in size and shape by changing the preparation conditions, such as hydrothermal temperature, reaction time, solution concentration, and precursor type.

1.3.1.3 *Surfactant assisted synthesis*

Surfactant plays an important role in the preparation of 1D nanostructures and has been adversely observed in the past decades.^[39] Surfactants can control size and shape of the NP's, can prevent aggregation and can also make nanoparticle surface hydrophilic/hydrophobic to make them compatible with various solvents. The stability of

nanoparticle dispersions and their tendency to agglomerate can be considered in the context of electrostatic, steric, and van der Waals forces among the particles using Derjaguin-Landau-Verwey-Overbeek (DLVO) theory.^[59] Aggregation of NP's due to attractive forces can be prevented by applying an electrostatic double layer, or by use of a surfactant functioning as a steric stabiliser (Fig.1.3).^[60]

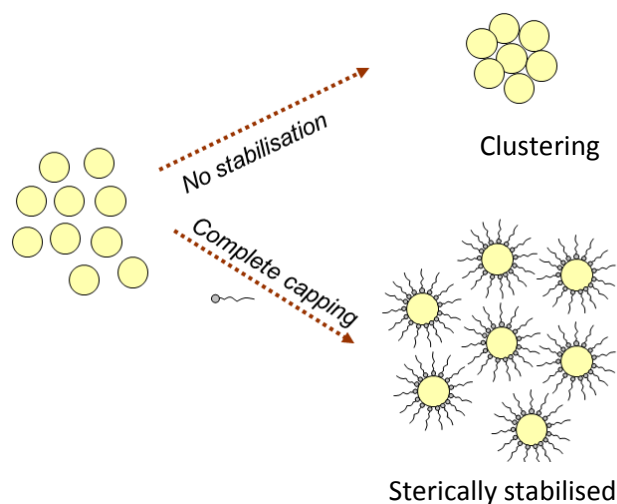


Fig. 1.3 Schematic diagram showing stabilization of NPs by long chain fatty acids by virtue of steric hindrance.

The Electrostatic stabilization is induced by charge and so is a pH sensitive method. NP's in suspension can be sterically stabilized by chemisorbed surfactants preventing the aggregation between colloidal NP's due to its steric hindrance effect (so-called bumper effect of polymers in the colloidal dispersion)^[61] or it is due to a rather entropy effect resulting from reducing polymer configurational freedom instead of a physical force.^[59] Surfactants such as cetyl trimethyl ammonium bromide (CTAB), polyvinylpyrrolidone (PVP), tetrabutylammonium bromide (TBAB), and polyethylene glycol (PEG), oleic acid, decanoic acid etc. are the commonly used surfactants in synthesis of ceria NP's.^[54, 57, 62]

Hyeon and co-workers have developed a new procedure for the synthesis of monodisperse nanocrystals of metals, metal oxides, and metal sulfides without going through a size-selecting process.^[63] In these syntheses, metal-surfactant complexes generated in situ are thermally decomposed to form monodisperse such as 6-13 nm iron oxide NP's. In addition, they reported that large quantities 40 g batches of uniform-sized magnetite (Fe₃O₄) NP's and other materials such as MnO and CoO NP's can be prepared in a single reaction without a size-sorting step. Instead of using toxic and expensive organometallic compounds, the metal-oleate complex can be prepared by reacting inexpensive and environmentally friendly compounds, namely, metal chlorides and sodium oleate.^[63] When such material is heated slowly in a solvent with high boiling point, the complexes decompose and form nanocrystals.

1.3.1.4 Other methods

Microemulsion method: Microemulsions have been widely used as an ideal liquid-phase method to prepare inorganic NP's.^[64] Microemulsions are transparent and isotropic liquids with nanosized water pools dispersed in a continuous phase and stabilized by surfactant and co-surfactant molecules at the water/oil interface. Compared to other techniques, the emulsion method has several advantages in producing particles with a spherical shape and narrow size distribution.^[65] However, the synthesis of rare earth compounds such as ceria has rarely been reported by the emulsion method. On the other hand, the BET specific surface area and the overall catalytic activity are affected by the preparation method of the catalyst.^[27] Masui *et al.* reported that the CeO₂/Al₂O₃ catalyst prepared by the microemulsion method shows higher activity for carbon monoxide oxidation, despite the fact that the CeO₂/Al₂O₃ catalyst surface area is as low

as that prepared by the co-precipitation method.^[66] Adachi et al. obtained 2.6 and 4.1 nm ceria particles using reverse micelles.

Sonochemical method: Sonochemistry is the application of ultrasound to chemical reactions and processes. Sonochemical synthesis of ceria NP's has been well documented in literature.^[30, 50] Ultrasound irradiation can induce the formation of particles with much smaller size and higher surface area than those produced with other methods.^[67] The physical effects of ultrasound arise from acoustic cavitation, that is, the formation, growth, and implosive collapse of bubbles occurring in a liquid medium.^[68] During acoustic cavitation, an equivalent temperature up to 5000°C, a pressure of ~20 MPa, and a very high cooling rate of 109°C/s could be attained at the location of the microbubbles. The ultrasound-induced impactive force can break the larger particles and sheets, and hinder the formation of hollow nanostructure.^[69] Gedanken et al. synthesized 3.3 nm CeO₂ ultrafine particles by sonochemical treatment. Zhu et al. also fabricated 2.6 and 2.8 nm nanocrystalline ceria particles using sonochemical and microwave assisted heating methods.^[44]

Sol-gel method: Sol-gel process is a colloidal route used to synthesise ceramics with an intermediate stage including a sol and/or gel state. This process involves precipitation of metal chlorides, followed by the removal of the reaction by-products. The precipitate is converted into colloidal sol by the addition of an electrolyte (normally acids). The sol gets converted in to a gel by aging. Gel is a three dimensional structure of solid enclosing the liquid (solvent) which on further removal of liquid results in the final material in the hydroxylated state. Typical precursors are metal alkoxides and metal chlorides, which undergo various forms of hydrolysis and polycondensation reactions.

$Ce_xZr_{1-x}O_2$ ($x = 1, 0.7, 0.4, 0.2, 0$) solid solution powders were successfully synthesized by a modified sol-gel method using simple metal nitrate precursors as sources for cerium and zirconium.^[70] The formation of a metal oxide involves connecting the metal centers with oxo (M-O-M) or hydroxo (M-OH-M) bridges, therefore generating metal-oxo or metal-hydroxo polymers in solution. Lin et al. prepared ceric and cerous sol by conventional precipitation-peptisation method for preparing membranes.^[71]

Combustion synthesis: Nano-structured catalysts with high surface area can be prepared by solution combustion synthesis (SCS).^[72] This synthesis method involves a self-sustaining strongly exothermal reaction between a sacrificial fuel and nitrates, that act as precursors of the final product. All the reactants are dissolved in water and the resulting solution is heated up to a temperature (between 300 and 700°C) suitable for the ignition of the whole reaction mass process. After ignition the reaction quickly goes on spontaneously, due to the heat evolved by the chemical reaction itself. In this way a ceramic powder made of agglomerates of very small particles (less than 1 μm in size), showing high porosity and high specific surface area, can be rapidly obtained. The combustion synthesis of fine particles of ceria was investigated since 1990,^[73] but only more recently a method suitable for the simultaneous synthesis and deposition of ceria on a ceramic honeycomb (and then for processing catalytic traps) has been developed.^[74]

Thus taking into account of the easiness and advantages of the solution techniques, this thesis employed a hydrothermal cum precipitation approach for morphology controlled synthesis. Prepared ceria NP's were further utilized to study the effect of particle morphology on glass polishing and high temperature oxidation catalysis. Further, a reflux synthesis in presence of the oleic acid surfactant has been utilized to

prepare monodisperse oleophilic NP's of ceria. These NP's were stably dispersed in transformer oil for its usage as heat transport fluid. The rate of heat transfer of the ceria nanofluid was further compared with alumina and zirconia fluids possessing the highest and the lowest thermal conductivities respectively among ceramic oxides. Pertaining to these objectives, brief introduction is discussed on the applications of ceria with special emphasis on the topics of glass polishing, oxidation catalysis, and nanofluid for heat transport.

1.4 Various applications of cerium dioxide

Cerium dioxide (CeO_2) commonly called as ceria is a versatile material which shows size/shape selective properties which make them suitable in various applications. As a well-known functional rare earth material, ceria has wide applications in fields such as catalysis, electrochemistry, and optics due to its unique properties. Nanoceria with face-centered cubic fluorite-type structure, has found many applications mainly in solid oxide fuel cells,^[75] oxidation catalysis,^[74] gas sensors,^[32] oxygen storage,^[45] as key components in automobile exhaust catalysts, in chemical mechanical planarization (CMP)^[76] and also as nanofluids for heat transfer.^[77] CeO_2 also has strong absorption in the ultraviolet (UV) range and is hence used as UV blocking and shielding materials. In those applications, CeO_2 NP's have significant impact not only due to their considerably small sizes and high surface areas but also due to the general improvements in their material properties with respect to their microsized or bulk like materials.

CeO_2 is also found to be an efficient candidate in photocatalysis although the vast majority of the studies are carried out with modified/pure TiO_2 . A novel efficient CeO_2 -based photocatalyst with visible-light activity has been developed recently by Primo et al.

with comparable or higher efficiency than those currently known.^[78] CeO₂ nanostructures have also been used in photocatalytic hydrogen production.^[79] Oriented hexagonal CeO₂ nanorods (NRs) with {110} planes as the main exposed surfaces were directly grown on Ti substrates via a simple template-free electrochemical method.^[80] The photocatalytic activity of CeO₂ NRs was studied in water splitting reaction and compared with that of commercial CeO₂, CdS and TiO₂ (P25). It was found that the activity of CeO₂ NRs is higher than those of commercial CeO₂ and CdS.^[80] The hydrogen evolution rate of CeO₂ NRs reached 741 μmol g⁻¹.

For instance, CeO₂ is adopted into three-way catalysts (TWCs) for reducing the emission of the toxic pollutants (CO, NO_x, and hydrocarbons, etc.) from automobile exhaust, because of its high oxygen storage capacity (OSC), associated with its rich oxygen vacancies and low redox potential between Ce³⁺ and Ce⁴⁺. Sintered CeO₂ doped with other rare earth ions has high oxide ion conductivity at a comparable low temperature (about 600 °C) and thus has been applied as electrode in solid oxide fuel cells.

1.4.1 Glass polishing

Polishing is considered to be an expensive machining process, in terms of time and labour costs depending on the required surface finish, optic size, and amount of surface roughness from preceding machining operations. A material could remain on the polishing system for hours to days. Thus, understanding the underlying mechanisms and basic science associated with the polishing process is crucial which in turn, builds up methods and procedures to reduce cost, trim schedule, and bolster performance. With an increased need for low surface roughness optics, as in X-ray and enhanced ultra-violet

applications, it is imperative to understand the impacts of changing system variables. Lu, et al., examined highly polished corundum axe fragments found at an ancient Chinese settlement at Zhejiang Yuhang Wujiabu, circa 2500 BC.^[81] They found through Atomic Force Microscopy (AFM) that the surface roughness was on the order of a few nanometers. Over the past 4500 years, humankind has only increased in polishing ability on the order of several nanometers.

Some of the methods used earlier to finish the optical surfaces includes polishing abrasive in suspension,^[82] float polishing,^[83] magnetic field assisted fine finishing,^[82] elastic emission polishing^[84] and laser polishing.^[85] Since then, significant advancement has been made in both the technology of polishing and in the understanding of polishing mechanisms. Much of the coverage of this technology is found in optics and optical engineering publications. These publications are not often read by the glass scientist because polishing is commonly regarded as a mechanical art rather than a scientific discipline. In reality glass polishing and glass surface science are primarily interrelated by their dependence on an understanding of aqueous corrosion chemistry and fracture mechanics processes.^[86]

With the miniaturisation of device scale and higher performance requirement of integrated circuits, the utilisation of the advanced photolithography and anisotropic etching techniques are essential. An evenly polished surface satisfies two requirements, specifically to ensure the good metal step coverage and to afford a field within the lithography depth of focus, that metal wires can be well patterned. Several methods are known to achieve a higher level of planarization: chemical-mechanical planarization,

laser reflow, coating with spin-on glasses, polymers, and resists, thermally reflowing materials, dielectric deposition.^[87]

1.4.1.1 Chemical Mechanical Planarization/ Polishing (CMP)

Chemical-mechanical polishing commonly abbreviated as CMP is a process that uses slurry of an abrasive in a corrosive chemical to physically grind flat and chemically remove the microscopic topographic features on a wafer so that subsequent processes can begin from a flat surface.^[88] The process of material removal is not simply that of abrasive scraping, like sandpaper on wood. The chemicals in the slurry also react with and/or weaken the material to be removed. The abrasive accelerates this weakening process and a polishing pad helps to wipe the reacted materials from the surface. The experimental setup of chemical mechanical planarization is as shown in Fig. 1.4.

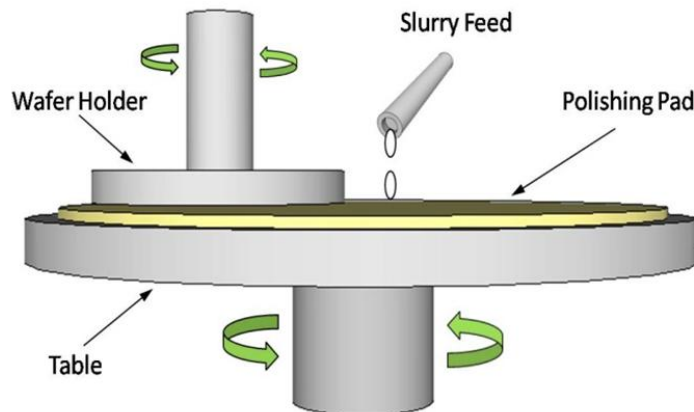


Fig. 1.4 Experimental setup of CMP

CMP is mostly used in the optical industry; this technique is influenced by a great number of technological parameters. The two most important are the type of polishing pad and the polishing abrasive.^[89] Only a few materials act as efficient polishing

compounds. For glasses, the best material by far is CeO_2 , followed by ZrO_2 , ThO_2 , TiO_2 and Fe_2O_3 .^[86] A small number of other oxides are also known to polish glass, but at substantially lower rates. CMP is also being used to form shallow trench isolation, metallization gates, Cu-based interconnect and low “ k ” dielectrics in the manufacturing of integrated circuits.^[90] The processes of CMP and Cu-CMP are widely used to achieve global planarization for the next generation integrated circuits.^[91] Ceria particles-based dispersions are used to polish/planarize silicon dioxide at a high rate while protecting the underlying silicon nitride in shallow trench isolation structure formation.^[92]

In 1984, Brown and Cook first proposed the concept of ‘tooth’ to explain the removal of material in the polishing regime.^[93] An analogy is the act of brushing one's teeth. The toothbrush is the mechanical part and the toothpaste is the chemical part. Using either the toothbrush or the toothpaste alone will get one's teeth somewhat clean, but using the toothbrush and toothpaste together makes a superior process. CMP can be used to planarize both insulating and conducting materials used in device wiring. Insulating materials include various silicon dioxides and low dielectric constant materials (low K materials), typically polymeric materials. The conducting materials include tungsten, aluminium, and copper. The CMP of insulators uses silica or ceria as the abrasives while the CMP of conductors uses alumina in most cases.^[94] The stability of the slurry is an important issue in slurry development for CMP because the rapid settling abrasives may clog the slurry distribution lines and cause unpredictable problems during semiconductor manufacturing. In addition, the coagulation of the abrasive particles is extremely detrimental to wafer polishing because it increases the defects on the polished wafers and reduces the yield.

Chemical-mechanical-planarization (CMP) has become an important process technology for centuries in semiconductor manufacturing to planarize the surface in and the topography on the wafer and facilitate further processing.^[95, 96] CMP has been widely studied in recent decades due to its critical role to form precise optics and in the microelectronics industry.^[97]

Before about 1990 CMP was looked on as too “dirty” to be included in high-precision fabrication processes. Unlike most semiconductor processes, CMP covers the wafer with particles, both from the polishing slurry and from the wafer itself. These particles must be removed before the wafer can proceed to the next process step.^[98] Lack of planarity may lead to severe problems for lithography (insufficient focus depth) and dry etching in sub 0.5 μm IC processes.^[99]

Why Ceria?

Mass transport during polishing is determined by the relative rates of the following processes:^[86]

- (1) Movement of solvent into the surface layer under the load imposed by the polishing particle;
- (2) Surface dissolution under load;
- (3) Adsorption of dissolution products onto the surface of the polishing particle;
- (4) The rate of back-deposition of dissolution products onto the surface;
- (5) Surface dissolution which occurs between particle impacts.

It is suggested that polishing compounds such as CeO_2 or ZrO_2 possess a chemical tooth that expedites both bond shearing at the substrate surface and transport of reaction products away from the surface faster than their rate of redeposition. Cerium

oxide (ceria) has the cubic fluorite crystal structure that is stable from room temperature to its melting point as compared with other pure oxides such as zirconia and bismuth oxides having oxygen ion conductivity.^[100] Surfaces of ceria particles are not the same as the interiors and that such differences can be brought about by several different mechanisms. At the surface of the particles Ce^{3+} is present. Cation impurities detected in the particles, such as La, are enriched at the surface with Ce^{3+} .^[101] Ceria based CMP is also used to finish CRT screens and LCDs and is used in the ophthalmic industry for prescription lens polishing.^[86, 102]

It is quite evident from the literature that ceria based CMP slurries are potential material for future planarisation of substrate/devices in integrated circuits for which the most critical part is the preparation of monomodal nanosized ceria. CMP offers utilization of the advanced and anisotropic etching technique to achieve evenly polished surface for high tech applications. As engineers struggle with today's gritty demands: new formulations for lowering defectivity, low-k insulators, and next-generation problems, such as premetal dielectric polish for inlaid gates, the market for slurries will see ~29% compound annual growth as per US survey. There is no reports available about any indigenous manufacturer of ceria based CMP in India. Cabot Microelectronics Corporation in US and Hitachi Chemical Co. Ltd. Japan have recently (2005) developed high-performance CMP slurry product for STI (Shallow Trench Isolation) that can decrease scratches from polishing by two-thirds and provide a twofold increase of surface flatness over existing products.

1.4.2 Ceria nanocatalysts

Rare Earth (RE) oxides have been used widely as catalysts for automotive emission control, since catalysts containing RE materials were developed to reduce automotive emissions by Libby in 1971.^[103] The most significant of the oxides of rare earth elements in industrial catalysis is certainly CeO₂.^[104] The importance of CeO₂ in catalysis is also demonstrated by the number of industrial and academic publications which have appeared on the topic over the last few years as shown in Fig. 1.5.

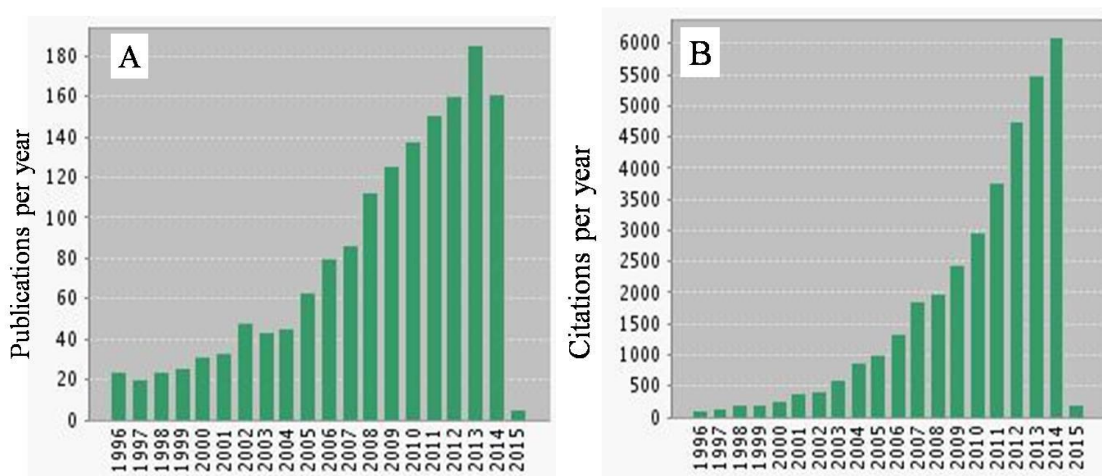


Fig. 1.5 Annual growths in A) numbers and B) citations of cerium oxide nanocatalysts according to the literature database ISI Web of knowledge as on January 30, 2015.

In the developing world of rapid industrialization and growing population, it is essential to address the issues in pollution control and renewable energy due to rapidly depleting fossil fuels and heavy pollution of the environment by combustion-based technologies. An increased need for a global green economy in the energy and transportation sectors has made catalytic applications of CeO₂ relevant. Automobile and industrial exhausts such as carcinogenic soot particles/particulate matter and poisonous

CO molecules are major environmental concerns and the major challenge is the efficient abatement of soot and CO by catalytic oxidation.

There are several emerging catalytic processes for which cerium oxide is being actively investigated. Some of them are outlined below with special emphasis on combustion of particulate matter.

i) Three-way catalysts (TWCs)

The worldwide motor vehicle production has been increasing dramatically during the last decades, environment has been contaminated with the exhaust gases of the automobiles, the most common of which are HCs, CO and NO_x. In turn, demand for modern technologies and devices which can efficiently lower the levels of pollutant gases and/or convert them to environmentally harmless products has risen. Increasingly stringent environmental legislations, on the reduction of NO_x and soot from the various sources of exhaust gases require the development of new devices/technologies that can abate these pollutants.^[105] Good examples of such devices are the three-way catalytic converters that rapidly convert CO and C_xH_y to CO₂ and H₂O and simultaneously reduce NO_x to molecular nitrogen even in highly fluctuating emission concentrations.

ii) Combustion of particulate matter

iii) In Fuel cell processes

iv) Fluid cracking catalysis

1.4.2.1 Combustion of particulate matter

The catalytic activity of cerium oxide towards the combustion of carbonaceous materials at low temperature has been widely investigated.^[74, 106] The main reason for the

generation of particulate matter (PM) is the extensive use of diesel engines, meanwhile stationary sources may also contribute.^[105] PM is mainly constituted by carbonaceous particles (often called soot), originated from the incomplete in-cylinder combustion of the fuel, with diameters ranging from few nanometers (10–20 nm) to up to hundreds of nanometers (the particles exceeding few μm are a negligible fraction), and the most common ones are around 100–200 nm.^[107] The soot particles can cause serious risks to human health and pollutes the atmosphere. Hence removal of PM is a topic of ongoing research. Soot mainly consists of chains or clusters of carbon spherules on which hydrocarbons, SO_3 and water are adsorbed.^[108]

Various emission-reduction technologies have been developed. The direct oxidation of these soot particulates needs high temperatures (around 600°C), and when the engine is fitted with non-catalytic traps frequent high temperature regenerations are required.^[105] These regenerations are inefficient and inconvenient. Besides improving engines and fuel quality, filtering followed by catalytic oxidation is considered to be the most direct and efficient solution to reduce PM.^[109] One way to circumvent the emission of soot produced by diesel vehicles is to trap the particles on a Diesel Particulate Filter (DPF) and burn the soot periodically to prevent a pressure increase in the exhaust line.^[74] Catalysts appropriate for promoting low temperature combustion of carbonaceous materials may indeed be applied in these traps. The exhaust gases may cool down to 180– 400°C along the pathway from the engine to the silencer, hence it is mandatory to develop catalysts active enough to ignite soot within the above temperature range.^[108] These catalysts can be either deposited on a ceramic support (honeycomb or foam filtering devices) thus obtaining a catalytic trap, or generated inside the combustion

chamber by using a proper metal-organic catalyst precursor that must be added to the fuel. In this last case the catalyst particles get in tight contact with soot and are carried by exhausts towards the filtering device where soot combustion occurs.

Several kinds of catalysts have been tested in soot oxidation which includes, perovskite type oxides,^[110] spinel type oxides,^[111] alkaline or heavy metal oxides,^[111-113] mixtures of halides with vanadates or molybdates,^[114, 115] precious metals.^[116] Ceria is commonly believed to display appreciable oxidation activity, fair thermal stability, poor chemical reactivity with respect to many ceramic supports and the main diesel emission components (water vapour, carbon and nitrogen oxides). Hence CeO₂ has been proposed as a promising soot oxidation catalyst to accelerate the soot-O₂ reaction by involving the participation of ‘active oxygen’ and thereby lower the onset temperature of the soot oxidation. Ceria is actually worldwide adopted as a promoter of most automotive catalysts.^[74] Ceria is of great significance as a basic catalytic material for soot combustion because of its appreciable oxygen storage capacity (OSC) and excellent redox properties. However, the temperature window of soot oxidation under pure ceria is much higher than the temperature of diesel exhaust (< 400°C). Further, significant deactivation of CeO₂ occurs at high temperature because the particles are sintered.

1.4.2.2 Factors affecting catalysis

One of the widely accepted scenarios behind catalysis is the influence of surface area of the catalyst. In catalytic reactions involving ceria, the redox chemistry of ceria is highly influential which can be tailored through size/shape selective syntheses.

1. Size / Surface area: Regarding particle size, it has been known for many years that the rates of some reactions depend on particle size (structure sensitive reactions) and some do

not (structure insensitive).^[117] The common method for maximizing the number of active sites and efficiently utilizing expensive metals is to reduce the catalyst particle domain size as far as possible. As a result, active catalysts typically contain small particles; these are often single or polycrystals with sizes less than 10 nm and even as small as 1 nm. Therefore, the particle size effect is often used to describe the relationship between the reaction rate and the catalyst particle size, especially in the size range from 1 to 10 nm. Gold NPs are a classic example of this topic.^[118] Bulk gold has long been viewed as being catalytically inert; however, 2–5 nm particles dispersed on reducible oxides are highly active towards CO oxidation at low temperatures. This prominent size dependent effect has been interpreted on the basis of the variations in the geometric and/or electronic properties of the active gold atoms at smaller particle sizes.^[118] The catalytic combustion of diesel particulate is a process based on a heterogeneous reaction involving solid particles of soot, gaseous oxygen and, of course, the solid catalyst.

Observing the soot oxidation temperature (T_{50} or T_p) while subjecting mixture of soot and ceria catalyst in fixed ratios to thermogravimetric analysis is one of the methods used widely to assess the catalytic activity.^[109, 119-122] Palmisano et al. reported that the adoption of small particles of catalyst can be quite convenient as it increases the number of contact points between the two counter parts.^[74] They have observed ~27% reduction in soot oxidation temperature in presence of 8 nm ceria NPs prepared by solution combustion method.^[74] The structural features and physicochemical characteristics, especially the redox capacity of CeO_2 are inevitably changed by doping. In recent years, doping of CeO_2 with transition, rare earth, or alkali metals to form ceria based solid solutions has proved to be a convenient and effective approach to improve the catalytic

activity and thermal stability of CeO_2 . This is because of the fact that doping confers interesting properties to soot combustion catalysts due to high availability of surface oxygen and high surface reducibility.^[121, 123-125] A very well known dopant for ceria is zirconium, which promotes bulk oxygen mobility in ceria–zirconia solid solutions.^[126] Lopez et al. reported a reduction in soot combustion temperature of ~7% and 26% with CeO_2 and $\text{Ce}_{0.69}\text{Zr}_{0.31}\text{O}_2$ respectively.^[120] The effect of rare earth doped ceria in soot oxidation has been studied by Makkee et al. and reported ~24% reduction in soot combustion temperature with 10 mol% La doped ceria calcined at 1000°C .^[105]

2. Structure/morphology of the catalyst: The interaction between the catalyst and the oxygen contained in diesel exhausts is also believed to play an important role in the combustion of soot, in particular when the catalyst acts as an oxygen pump or even promotes oxygen spill-over. Precise control of the nanostructure of solid catalysts widely used in a variety of industrially important reactions and to deepen the mechanistic understanding of the catalytic process at the atomic, molecular, and nanometre scales.^[118] In this way, the concept of morphology-dependent nanocatalysts provides a new strategy for finely tuning catalytically active sites and significant progress has been made.^[121] However, several critical issues related to the application of nanostructured catalysts to practical processes need to be further addressed.

The shape of CeO_2 nanocrystals is correlated with the predominance of particular crystal facets which exhibit selective reactivity in different catalytic processes.^[127, 128] The analysis of active/exposed planes in nanostructures is qualitatively done through HR-TEM technique.^[45, 129] The quantitative analysis of active planes/preferential orientation of facets by performing Harris analysis on XRD data is reported in ceria,^[130] zinc oxide

,^[131] tin oxide,^[132, 133] and cobalt nanostructures.^[134] In Harris analysis, the preferential orientation of the crystallites along a crystal plane (hkl) in nanocrystals is measured as texture coefficient, $C(hkl)$. A sample with randomly oriented crystallites presents a $C(hkl)$ of 1, while a larger value indicates an abundance of crystallites oriented to that (hkl) plane.^[130, 135] More details on Harris analysis is discussed in chapter 2 and 3. The {100} and {110} facets of ceria are reported to be catalytically more active than the stable {111} facet due to the ease of formation of oxygen vacancies on them.^[136] The presence of defects/oxygen vacancies is another factor which affects catalysis. The concentration of defects/Ce³⁺/oxygen vacancies vary with size and also with shape of the catalyst.^[6] Deshpande et al. reported that the concentration of Ce³⁺ increased from 17 to 44% as the particle size reduced from 30 to 3 nm.^[6] Ceria nanorods are reported to possess ~60% Ce³⁺. The presence of kinks, edges etc are the favoured sites for defects. Whereas the Ce⁴⁺ atoms prefer to reside at highly coordinated positions, the reduced cations tend to occupy corner and edge sites and thus are more likely to affect the reactivity of the NP's.

The studies performed by Zhou et al. showed that interaction of CO with ceria rods (exposing preferentially the {1 1 0} and {1 0 0} faces) is stronger than with ceria nanoparticles resulting in a greater conversion rate for CO to CO₂.^[55] This activity dependence is also observed on different ceria nanoshapes like cubes and octahedral exposing preferentially the {1 0 0} and {1 1 1} surface planes^[137] and more recently in 3D flower-like ceria microspheres.^[138] The {1 0 0} and {1 1 0} dominant surface structures are also shown to affect the catalytic properties of Rh supported on ceria nanorods in ethanol reforming reaction^[139] and of Pd-loaded 1D ceria in water gas shift reaction.^[140] The more reactive planes are also responsible for shape dependent OSC

behavior that has been observed over ceria nanostructures.^[55] Morphology dependant soot oxidation study has been performed by Fino et al. with ceria nanofibers, self-assembled stars and nanopowders obtained by SCS. They observed better activity ~30% reduction in soot oxidation temperature with star shaped ceria crystals of high SSA (105 m²/g).^[141]

Hence, the catalytic activity is related to the chemical composition and the structure of the catalyst as well as to the size of the catalyst particles and their specific surface area. One very characteristic feature, and the main reason that ceria is so useful in many of these applications, is ceria's high oxygen storage capacity (OSC). The OSC is a measure of how much oxygen a material can store and release. Ceria's high OSC makes it a powerful catalyst for reduction-oxidation (redox) chemistry, where it mediates reduction through the uptake of oxygen, and oxidation through the release of oxygen. It is well-known that once Ce³⁺ appears in the fluorite lattice, oxygen vacancies are generated to maintain electrostatic balance.^[142] However, while the rate of cerium oxidation is much faster, reduction of ceria is generally sluggish. Thus, great effort has been made to promote its reducibility. As discussed in these studies, the reduction of ceria is proposed to be controlled by the nature of the oxygen vacancies, since oxygen diffusion, the rate-controlling step, depends on the type, size, and concentration of oxygen vacancies. This indicates that any processing condition which favors the formation of more desired oxygen vacancies will result in enhanced reducibility. However, creating these favorable defects and understanding their roles in the reducibility and activity of nanosized ceria at the atomic level is still lacking.

In all of the above mentioned applications, the ability of cerium to cycle between Ce^{3+} and Ce^{4+} is crucial; however, the mechanisms by which ceria promotes reactions are complex. Understanding these mechanisms is technologically important because the properties of ceria are strongly affected by its morphology, pre-treatment conditions, and presence of dopants. However, not many fundamental studies are reported in the open literature on morphology dependant soot oxidation using CeO_2 or CeO_2 containing materials.

1.4.3 Nanofluid

Nanocrystalline materials represent a bridge between molecules and solid state and exhibit properties that are unique.^[143] New coatings and dispersions will take advantage of the huge surface areas and the enhanced chemical reactivity at the surfaces of nanocrystalline materials. These surfaces can be modified with ligands, can be consolidated into porous solids, or can be incorporated into fluids or plastics. One such emerging area is the use of nanoparticulate stable fluid for heat transfer, an innovative concept developed by Dr. Choi of Argonne National Laboratory, US in 1995.^[77, 144] Present applications of nanofluids have an estimated total market size of ~\$30-60 million with a scope phenomenal growth.^[145] There are some indications that basic and applied research in nanofluid is growing and significant. First, the new, young nanofluid community has published more than 250 research articles since 1995. In 2006 alone, the number of publications in this area in Science Citation Index (SCI) journals topped 100. Second, prestigious institutions worldwide have established research groups or interdisciplinary centres with a focus on nanofluids. Several universities have graduated Ph.D.s in this new area. Third, small businesses and large multinational companies in

different parts of the world are working on nanofluid for their specific applications. As a result, the study of nanofluids has emerged as a new field of scientific research and innovative applications.^[146]

The term nanofluid is used to describe a fluid consisting of solid NPs with size less than 100 nm suspended in it with solid volume fractions typically less than 4%.^[147] The majority of NPs, used in such suspensions, are based on iron or copper or aluminium metals as well as their oxides. The size and volume fraction of the NPs in suspension, the thermal properties and conductivities of the NPs and the suspending media and most importantly the overall thermal conductivity, flow dynamics and stability of the suspension decides the suitability of a nanofluid in a cooling process. The rheology of the fluid as a function of temperature is also a very important issue. The flow patterns of a nanofluid changes with the change in temperature of the fluid, as the viscosity and consequently the thermal motions of NPs are proportional to the temperature of the fluid. Nanofluids give rise to unusual fluid mechanical phenomena and thermal behaviour.^[148]

NPs, whether metallic or oxidic, need to be in a stable suspension to be used as heat transfer fluids with consistent thermal properties with time. Particles over 200 nm size, with no surface charge, normally settles down in a suspension due to gravitational forces acting on them. The kinetics of motion of NPs smaller than 100 nm is dominated by thermal energy. NPs tend to agglomerate to reduce their surface energy due to the high surface area to volume ratio. There are two major ways to prevent small NPs from agglomeration, e.g., steric and electrostatic stabilization of the particle surfaces as mentioned in section 1.3.1.3.

1.4.3.1 *The concept of nanofluid for thermal management*

In the development of energy-efficient heat transfer equipment, the thermal conductivity of the heat transfer fluid plays a vital role.^[149] However, traditional heat transfer fluids such as water, engine /transformer oil, and ethylene glycol mixtures, have inherent poor thermal conductivities.^[150] With increasing global competition, industries have a strong need to develop advanced heat transfer fluids with significantly higher thermal conductivities than are presently available. Despite considerable previous research and development efforts on heat transfer enhancement major improvements in cooling capabilities have been constrained because of the low thermal conductivity of conventional heat transfer fluids. However, it is well known that at room temperature, metals in solid form have orders-of-magnitude higher thermal conductivities than those of fluids. For example, the thermal conductivity of copper at room temperature is about 700 times greater than that of water and about 3000 times greater than that of engine oil. The thermal conductivity of metallic liquids is much greater than that of non-metallic liquids. Therefore, the thermal conductivities of fluids that contain suspended solid metallic particles could be expected to be significantly higher than those of conventional heat transfer fluids. In fact, numerous theoretical and experimental studies of the effective thermal conductivity of dispersions that contain solid particles have been conducted since Maxwell's theoretical work was published more than 100 years ago.^[151] However, all of the studies on thermal conductivity of suspensions have been confined to millimeter- or micrometer-sized particles. The major problem with suspensions containing millimeter- or micrometer-sized particles is the rapid settling of these particles. Furthermore, such particles are too large for micro systems.

Earlier reports indicate that the nanofluids can be fabricated by two major approaches: formation of the NPs in presence of the medium in which they are to be dispersed, for example, metal NPs by evaporation/ gas condensation techniques. The other approach is to prepare NPs first and then disperse the NPs in the fluid medium uniformly and in stable manner. The solid particle and size content, the shape of the particles, the surface charge of the particles and the stability of the particles in the medium (reactivity), all influence in the preparation of successful nanofluid. Oxides such as titania, alumina and zinc oxide are reported to be made by plasma arc method and directly dispersed from the formation stage in order to prevent atmospheric contamination as well as surface passivation.

1.4.3.2 Oil based heat transport fluid

Nanofluid-based heat transfer plays an important role in diverse fields such as microelectronics, high voltage power transmission systems, automobiles, solar cells, biopharmaceuticals, medical therapy/diagnosis, and nuclear cooling.^[150] An important aspect in the preparation of nanofluid is the selection of the NPs for a specific application. Metal particles are generally conducting and therefore the effective thermal conductivity of the dispersed liquid increases. However, it has been well reported that ceramic particles such as alumina, titania and silica also has been effective in thermal management. Heat transport driven failures are quite often in high voltage power transformers. Dielectric oils in high voltage transformers provide efficient cooling which can extend the life of transformers.^[152] These transformer oils require excellent nanoparticle (NP) dispersion, high heat conduction, as well as electrical insulation at the same time. In this context, the use of insulating/semiconducting ceramic oxides such as

alumina, silica, ceria etc. can be beneficial. Further, some commercial oxides such as alumina and ceria manifest a tremendous price advantage compared to metal and carbon materials. On the other hand preparation of stable suspension of metal oxides in oil based coolants will be a challenge in view of the hydrophilic-hydrophobic nature of the particulates and the fluid. Various efforts including ultrasonication,^[153] using dispersants/surfactants^[154] and chemical surface modification have been extensively made to enhance stability of the suspension.^[147] However, it is still challenging to produce non-agglomerated nanofluids with the two-step method. Most of the recent studies were focused on the preparation of water/EG based nanofluids and very few reports are available on the preparation of oil based fluids. A brief literature survey on the physico-chemical properties of non aqueous fluids reported during the last few years is presented in **Table 1.2**.

Table 1.2 A summary on non aqueous nanofluid systems reported in literature

Entry	System Studied	Particle size (nm)	TC enhancement (%) / Vol%	TC vs vol %	TC vs temp	Viscosity vs Temp	Stability (Time)
1.	Poly α -olefin oil based CNT fluid ^[155]	Dia~ 25 nm and a length ~50 μ m	150/1	Increases	-	-	-
2.	Transformer oil based alumina nanofluid ^[152]	13	20/4	Increases	-	-	30 days
3.	Gear oil based Cu nanofluids ^[156]	40-60		Increases	Increases	Decreases	
4.	Silicon oil based multiwalled carbon nanotubes nanofluids ^[157]	500		-	Increases	Decreases	-
5.	Kerosene based Fe ₃ O ₄	15		Increases	Constant	-	7 h

	nanofluids ^[158]						
6.	Kerosene based silver nanofluid ^[159]	5-6	17/0.5	Increases	Decreases	-	-
7	Silicon oil based CNT fluid ^[160]	150 -200		-	-	Decreases	
8.	Transformer oil based Ag supported on silica nanofluid ^[161]	-	15/0.1	Increases	Increases	Decreases	Unstable
9.	Oil based Boron nitride nanosheet fluid ^[150]	5-6 atomic layer thick	~76/0.1 wt%	Increases	Increases	Decreases	~3 months
10.	Transformer oil based alumina nanofluid ^[162]	25	~4 /0.3	Increases	Increases	Decreases	-
11.	Gear oil based Cu nanofluid ^[163]	40	~24 /2	Increases	Increases	Decreases	20 days

A lot of studies were performed with the highly thermal conductive carbon nanotubes (2000 W/mK).^[164] The highest TC enhancement reported so far is 150% with 1 vol% of CNT dispersed in engine oil.^[155] However, later researchers could not obtain the same magnitude of the thermal conductivity enhancement of CNT nanofluids. The TC enhancement reported with metallic nanoparticles such as Ag and Cu lies within 15-25%, but the stability of the nanofluids reported was not much promising.^[161, 163] A good TC enhancement of 76% and reasonable stability of three months has been accomplished with boron nitride nanosheets.^[150]

1.4.3.3 *Hydrophobic modification of NP surface*

It is well known that most ceramic nanoparticles possess slight hydrophilic surface properties. Hence preparation of stable oil-based nanofluids requires hydrophobic modification of the NP surface by suitable methods. Steric stabilisation with the help of

an **amphiphilic** surfactant is the most widely used technique for preparing stable nanoparticle dispersions.^[130, 165, 166] Long chain fatty acids such as decanoic acid,^[167] stearic acid and oleic acid are some of the amphiphilic surfactants that have been reported earlier.^[130, 152, 159, 168, 169] Oleic acid is one of the most widely employed surfactants as it possesses a C18 tail with a *cis*-double bond in the middle, forming a kink which have been postulated as necessary for effective stabilization as shown in Fig. 1.6.

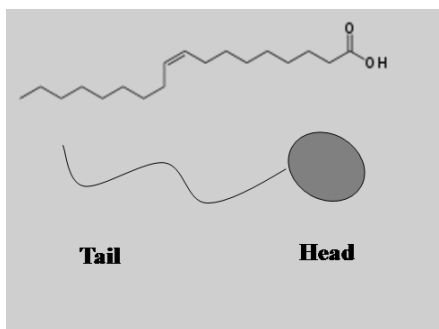


Fig. 1.6 Structure of long chain fatty acid oleic acid.

Oleic acid is also reported to form a dense protective monolayer, thereby producing highly uniform and monodisperse particles for the synthesis of various NCs from metals, metal oxides, and II-VI, IV-VI, and III-V group semiconductors.^[149] The presence of a carboxylic group with significant affinity to various surfaces together with a nonpolar tail group for sterical hindering is the base for the excellent stabilizing function of this ligand.

In short, nanofluid is a new field of scientific research that has grown enormously in the past few years. Still, it is a field in its adolescence, and there are a number of issues which have not been fully addressed yet.

1.5 Scope of the present thesis

The exhaustive literature provided above indicates the wide scope of nanostructured CeO₂ in the energy sector in the near future. Chemical, chemic-

mechanical and catalytic are the key areas where the CeO₂ based nanomaterials are continued to be investigated. Such applications depend on the production of nanostructured CeO₂ particles, it is important therefore to fabricate the CeO₂ nanoparticles by different techniques and characterize them. In this thesis three important fields of research pertaining to CeO₂ nanostructures are mainly addressed. Firstly, the morphology dependent polishing of silicate glass and its mechanism is studied in detail. Precipitation cum hydrothermal synthesis was utilized for preparing ceria NPs of spherical, rod, and cubical morphology and utilised as abrasive in CMP and the effect of surface properties of abrasive particles in polishing was studied in detail. In the subsequent chapter, the development of nanostructured CeO₂ in the forms of rods, cubes, and spheres of enhanced surface area was carried out by controlling the precursor concentration. These nanostructures were further utilised as catalyst in high temperature oxidation reactions. The third section of the thesis devotes to the development of surface modified/oleophilic ceria nanostructures through a simple reflux synthesis for phase transfer into oils for the development of heat transfer fluids. Therefore, the thesis epitomizes simple low temperature chemical syntheses for obtaining CeO₂ nanostructures for the novel applications in energy and environment applications.

1.6 References

- [1] Y. Gao, W. Wang, S. Chang, W. Huang, *Chemcatchem* **2013**, 5, 3610.
- [2] D. R. Lide, *CRC handbook of chemistry and physics*. 86th edition. Boca Raton, FL: CRC Press, Taylor & Francis; pp. 4-9, 4-48. (2005).
- [3] C. Sun, H. Li, L. Chen, *Energy Environ. Sci.* **2005**, 5, 8475.
- [4] A. Krishnan, T. S. Sreeremya, E. Murray, S. Ghosh, *J. Colloid Interface Sci.* **2013**, 389, 16.
- [5] G. R. Rao, B. G. Mishra, *Bull. Catal. Soc. India* **2003**, 2, 122.
- [6] S. Deshpande, S. Patil, S. Kuchibhatla, S. Seal, *Appl. Phys. Lett.* **2005**, 87.
- [7] M. P. Nolan, S.; Watson, G. W., *Phys. Chem. Chem. Phys.* **2005**, 8, 216.
- [8] W. C. Chueh, A. H. McDaniel, M. E. Grass, Y. Hao, N. Jabeen, Z. Liu, S. M. Haile, K. F. McCarty, H. Bluhm, F. El Gabaly, *Chem. Mater.* **2012**, 24, 1876.
- [9] A. Trovarelli, *Catal. Rev.-Sci. Eng.* **1996**, 38, 439.
- [10] G. R. Rao, *Bull. Mater. Sci.* **1999**, 22, 89.
- [11] A. Holmgren, B. Andersson, *J. Catal.* **1998**, 14, 178.
- [12] V. Perrichon, A. Laachir, G. Bergeret, R. Frety, L. Tournayan, O. Touret, *J. Chem. Soc. Faraday Trans.* **1994**, 90, 773.
- [13] T. J. Mazanec, *Solid State Ionics* **1994**, 11, 70.
- [14] A. Trovarelli, C. de Leitenburg, G. Dolcetti, *Chem. Tech.* **1997**, 27, 32.
- [15] H. C. Yao, Y.F. Yu Yao, *J. Catal.* **1984**, 86, 254.
- [16] W. P. Hsu, L. Ronnquist, E. Matijevic, *Langmuir* **1988**, 4, 31.
- [17] M. Hirano, M. Inagaki, *J. Mater. Chem.* **2000**, 10, 473.

- [18] J. E. Spanier, R. D. Robinson, F. Zheng, S. W. Chan, I. P. Herman, *Phys. Rev. B* **2001**, 64.
- [19] F. Zhang, S. W. Chan, J. E. Spanier, E. Apak, Q. Jin, R. D. Robinson, I. P. Herman, *Appl. Phys. Lett.* **2002**, 80, 127.
- [20] F. Zhang, Q. Jin, S. W. Chan, *J. Appl. Phys.* **2004**, 95, 4319.
- [21] M. Kamruddin, P. K. Ajikumar, R. Nithya, A. K. Tyagi, B. Raj, *Scr. Mater.* **2004**, 50, 417.
- [22] R. D. Purohit, B. P. Sharma, K. T. Pillai, A. K. Tyagi, *Mater. Res. Bull.* **2001**, 36, 2711.
- [23] L. Madler, W. J. Stark, S. E. Pratsinis, *J. Mater. Res.* **2002**, 17, 1356.
- [24] T. Y. Yu, J. Joo, Y. I. Park, T. Hyeon, *Angew. Chem. Int. Ed.* **2005**, 44, 7411.
- [25] M. Hirano, E. Kato, *J. Am. Ceram. Soc.* **1999**, 82, 786.
- [26] C. Sun, L. Chen, *Eur. J. Inorg. Chem.* **2009**, 3883.
- [27] T. Masui, K. Fujiwara, K. Machida, G. Adachi, T. Sakata, H. Mori, *Chem. Mater.* **1997**, 9, 2197.
- [28] Y. J. He, B. L. Yang, C. X. Cheng, *Mater. Lett.* **2003**, 57, 1880.
- [29] N. Guillou, L. C. Nistor, H. Fuess, H. Hahn, *Nanostruct. Mater.* **1997**, 8, 545.
- [30] L. X. Yin, Y. Q. Wang, G. S. Pang, Y. Koltypin, A. Gedanken, *J. Colloid Interface Sci.* **2002**, 246, 78.
- [31] Y. C. Zhou, R. J. Phillips, J. A. Switzer, *J. Am. Ceram. Soc.* **1995**, 78, 981.
- [32] H. I. Chen, H. Y. Chang, *Ceram. Int.* **2005**, 31, 795.
- [33] X. D. Zhou, W. Huebner, H. U. Anderson, *Appl. Phys. Lett.* **2002**, 80, 3814.
- [34] E. Matijevic, W. P. Hsu, *J. Colloid Interface Sci.* **1987**, 118, 506.
- [35] P. L. Chen, I. W. Chen, *J. Am. Ceram. Soc.* **1993**, 76, 1577.

- [36] J. G. Li, T. Ikegami, Y. R. Wang, T. Mori, *J. Am. Ceram. Soc.* **2002**, 85, 2376.
- [37] M. Yamashita, K. Kameyama, S. Yabe, S. Yoshida, Y. Fujishiro, T. Kawai, T. Sato, *J. Mater. Sci.* **2002**, 37, 683.
- [38] N. Uekawa, M. Ueta, Y. J. Wu, K. Kakegawa, *Chem. Lett.* **2002**, 854.
- [39] S. Chowdhury, K.-S. Lin, *J. Nanomater.* **2011**.
- [40] R. J. Hunter, *Clarendon, Oxford, UK* **1989**, vol. 1-2.
- [41] X. D. Zhou, W. Huebner, H. U. Anderson, *Chem. Mater.* **2003**, 15, 378.
- [42] T. Garcia, B. Solsona, S. H. Taylor, *Catal. Lett.* **2005**, 105, 183.
- [43] B. L. Cushing, V. L. Kolesnichenko, C. J. O'Connor, *Chem. Rev.* **2004**, 104, 3893.
- [44] Y. W. Zhang, R. Si, C. S. Liao, C. H. Yan, *J. Phys. Chem. B* **2003**, 107, 10159.
- [45] H. X. Mai, L. D. Sun, Y. W. Zhang, R. Si, W. Feng, H. P. Zhang, H. C. Liu, C. H. Yan, *J. Phys. Chem. B* **2005**, 109, 24380.
- [46] E. Tani, M. Yoshimura, S. Somiya, *J. Mater. Sci. Lett* **1982**, 1, 461.
- [47] M. Hirano, E. Kato, *J. Mater. Sci. Lett.* **1996**, 15, 1249.
- [48] M. Inoue, M. Kimura, T. Inui, *Chem. Commun.* **1999**, 957.
- [49] W. Q. Han, L. J. Wu, Y. M. Zhu, *J. Am. Chem. Soc.* **2005**, 127, 12814.
- [50] H. Wang, J. J. Zhu, J. M. Zhu, X. H. Liao, S. Xu, T. Ding, H. Y. Chen, *Phys. Chem. Chem. Phys.* **2002**, 4, 3794.
- [51] G. S. Wu, T. Xie, X. Y. Yuan, B. C. Cheng, L. D. Zhan, *Mater. Res. Bull.* **2004**, 39, 1023.
- [52] R. J. La, Z. A. Hu, H. L. Li, X. L. Shang, Y. Y. Yang, *Mat. Sci. Eng. A-Struct.* **2004**, 368, 145.
- [53] C. W. Sun, H. Li, H. R. Zhang, Z. X. Wang, L. Q. Chen, *Nanotechnology* **2005**, 16, 1454.

- [54] A. Vantomme, Z. Y. Yuan, G. H. Du, B. L. Su, *Langmuir* **2005**, *21*, 1132.
- [55] K. B. Zhou, X. Wang, X. M. Sun, Q. Peng, Y. D. Li, *J. Catal.* **2005**, *229*, 206.
- [56] P. X. Huang, F. Wu, B. L. Zhu, X. P. Gao, H. Y. Zhu, T. Y. Yan, W. P. Huang, S. H. Wu, D. Y. Song, *J. Phys. Chem. B* **2005**, *109*, 19169.
- [57] C. S. Pan, D. S. Zhang, L. Y. Shi, *J. Solid State Chem.* **2008**, *181*, 1298.
- [58] F. Dang, K. Kato, H. Imai, S. Wada, H. Haneda, M. Kuwabara, *Cryst. Growth Des.* **2010**, *10*, 4537.
- [59] J. Jiang, G. Oberdorster, P. Biswas, *J. Nanopart. Res.* **2009**, *11*, 77.
- [60] R. M. Cornell and U. Schertmann, *VCH: Weinheim* **1991**.
- [61] R. Si, Y. W. Zhang, L. P. You, C. H. Yan, *J. Phys. Chem. B* **2006**, *110*, 5994.
- [62] L. Zhang, R. He, H.-C. Gu, *Appl. Surf. Sci.* **2006**, *253*, 2611.
- [63] J. Joo, T. Yu, Y. W. Kim, H. M. Park, F. X. Wu, J. Z. Zhang, T. Hyeon, *J. Am. Chem. Soc.* **2003**, *125*, 6553.
- [64] P. Y. Feng, X. H. Bu, G. D. Stucky, D. J. Pine, *J. Am. Chem. Soc.* **2000**, *122*, 994.
- [65] J. Y. Bai, Z. D. Xu, Y. F. Zheng, H. Y. Yin, *Mater. Lett.* **2006**, *60*, 1287.
- [66] K.-S. Lin, S. Chowdhury, *Int. J. Mol. Sci.* **2010**, *11*, 3226.
- [67] J. X. Guo, X. Q. Xin, X. Zhang, S. S. Zhang, *J. Nanopart. Res.* **2009**, *11*, 737.
- [68] J. Kis-Csitari, Z. Konya, I. Kiricsi, *Functionalized Nanoscale Materials, Devices And Systems* **2008**, 369.
- [69] Y. Y. Zheng, T. J. Zhu, X. B. Zhao, J. P. Tu, G. S. Cao, *Mater. Lett.* **2005**, *59*, 2886.
- [70] J. H. Park, P. Muralidharan, D. K. Kim, *Mater. Lett.* **2009**, *63*, 1019.
- [71] N. Rane, H. Zou, G. Buelna, J. Y. S. Lin, *J. Membr. Sci.* **2005**, *256*, 89.

- [72] K. C. Patil, S. T. Aruna, S. Ekambaram, *Curr. Opin. Solid State Mater. Sci.* **1997**, 2, 158.
- [73] M. M. A. Sekar, S. S. Manoharan, K. C. Patil, *J. Mater. Sci. Lett.* **1990**, 9, 1205.
- [74] P. Palmisano, N. Russo, P. Fino, D. Fino, C. Badini, *Appl. Catal. B* **2006**, 69, 85.
- [75] D. Andreescu, E. Matijevic, D. V. Goia, *Colloids Surf. A* **2006**, 291, 93.
- [76] P. Supphantharida, K. Osseo-Asare, *J. Electrochem. Soc.* **2004**, 151, G658.
- [77] T. S. Sreeremya, A. Krishnan, A. P. Mohamed, U. S. Hareesh, S. Ghosh, *Chem. Eng. J.* **2014**, 255, 282.
- [78] A. Primo, T. Marino, A. Corma, R. Molinari, H. Garcia, *J. Am. Chem. Soc.* **2011**, 133, 6930.
- [79] C. Sun, H. Li, L. Chen, *Energy Environ. Sci.* **2012**, 5, 8475.
- [80] X. Lu, T. Zhai, H. Cui, J. Shi, S. Xie, Y. Huang, C. Liang, Y. Tong, *J. Mater. Chem.* **2011**, 21, 5569.
- [81] P. J. Lu, N. Yao, J. F. So, G. E. Harlow, J. F. Lu, G. F. Wang, P. M. Chaikin, *Archaeometry* **2005**, 47, 1.
- [82] D. Bouzid, N. Belkhie, T. Aliouane, *Iop, Materiaux 2010* **2012**, 28.
- [83] J. M. Bennett, J. J. Shaffer, Y. Shibano, Y. Namba, *Appl. Opt.* **1987**, 26, 696.
- [84] Y. K. Mori Y, Endo F., *6th INT. Conf. on Production Engineering Osaka* **1987**.
- [85] F. Vega, N. Lupon, J. A. Cebrian, F. Laguarda, *Opt. Eng.* **1998**, 37, 272.
- [86] L. M. Cook, *J. Non Cryst. Solids* **1990**, 120, 152.
- [87] G. Nanz, L. E. Camilletti, *IEEE T. Semiconduct. M.* **1995**, 8, 382.
- [88] Q. Luo, D. R. Campbell, S. V. Babu, *Langmuir* **1996**, 12, 3563.
- [89] D. Bouzid, S. Bouzid, M. Bouafia, U. Jungstand, V. Herold, *Glass Technol.* **1997**, 38, 18.

- [90] D. Pramanik, M. Weling, X. W. Lin, *CMP applications for sub-0.25 μm process technologies*, Vol. 98, **1998**.
- [91] C. H. Zhou, L. Shan, J. R. Hight, S. Danyluk, S. H. Ng, A. J. Paszkowski, *Tribology T.* **2002**, 45, 232.
- [92] V. P. R. Dandu, S. V. Babu, *Imaging Appl. Opt. Tech. Digest* **2012**.
- [93] N. Brown, L. Cook, *Paper TuB-A4, Tech. Digest, Topical Meeting on the Science of Polishing, Optical Society of America* **1984**.
- [94] Q. Luo, *Ind. Eng. Chem. Res.* **2000**, 39, 3249.
- [95] M. A. Fury, *Solid State Technol.* **1995**, 38, 47.
- [96] H. Landis, P. Burke, W. Cote, W. Hill, C. Hoffman, C. Kaanta, C. Koburger, W. Lange, M. Leach, S. Luce, *Thin Solid Films* **1992**, 220, 1.
- [97] G. B. Basim, J. J. Adler, U. Mahajan, R. K. Singh, B. M. Moudgil, *J. Electrochem. Soc.* **2000**, 147, 3523.
- [98] T. L. Myers, M. A. Fury, W. C. Krusell, *Solid State Technol.* **1995**, 38, 59.
- [99] H. C. Hong, Y. L. Huang, *IEEE T. Semiconduct. M.* **2004**, 17, 180.
- [100] S. Mochizuki, *Phys. Status Solidi B* **1982**, 114, 189.
- [101] S. R. Gilliss, J. Bentley, C. B. Carter, *Appl. Surf. Sci.* **2005**, 241, 61.
- [102] R. Sabia, Stevens, H. J., *The Glass Researcher* **1999**, 9, 16.
- [103] W. Zhan, Y. Guo, X. Gong, Y. Guo, Y. Wang, G. Lu, *Chinese J. Catal.* **2014**, 35, 1238.
- [104] M. Ozawa, C. K. Loong, *Catal. Today* **1999**, 50, 329.
- [105] K. Krishna, A. Bueno-Lopez, M. Makkee, J. A. Moulijn, *Appl. Catal. B* **2007**, 75, 189.
- [106] M. O'Connell, M. A. Morris, *Catal. Today* **2000**, 59, 387.

- [107] P. A. Kumar, M. D. Tanwar, S. Bensaid, N. Russo, D. Fino, *Chem. Eng. J.* **2012**, *207*, 258.
- [108] M. Issa, C. Petit, A. Brillard, J.-F. Brilhac, *Fuel* **2008**, *87*, 740.
- [109] Y. Sheng, Y. Zhou, H. Lu, Z. Zhang, Y. Chen, *Chinese J. Catal.* **2013**, *34*, 567.
- [110] Y. Teraoka, K. Nakano, W. Shangguan, S. Kagawa, *Catal. Today* **1996**, *27*, 107.
- [111] W. F. Shangguan, Y. Teraoka, S. Kagawa, *Appl. Catal. B* **1996**, *8*, 217.
- [112] A. F. Ahlstrom, C. U. I. Odenbrand, *Appl. Catal.* **1990**, *60*, 143.
- [113] M. L. Pisarello, V. Milt, M. A. Peralta, C. A. Querini, E. E. Miro, *Catal. Today* **2002**, *75*, 465.
- [114] C. Badini, G. Saracco, V. Serra, *Appl. Catal. B* **1997**, *11*, 307.
- [115] D. Fino, N. Russo, C. Badini, G. Saracco, V. Specchia, *Aiche Journal* **2003**, *49*, 2173.
- [116] R. E. Mariangeli, E. H. Homier, F. S. Molinaro, *Catalysis and Automotive Pollution Control, Amsterdam* **1987**, 457.
- [117] H. H. Kung, R. J. Pellet, R. L. Burwell, *J. Am. Chem. Soc.* **1976**, *98*, 5603.
- [118] Y. Li, W. Shen, *Chem. Soc. Rev.* **2014**, *43*, 1543.
- [119] M. Machida, Y. Murata, K. Kishikawa, D. Zhang, K. Ikeue, *Chem. Mater.* **2008**, *20*, 4489.
- [120] I. Atribak, A. Bueno-Lopez, A. Garcia-Garcia, *Catal. Commun.* **2008**, *9*, 250.
- [121] E. Aneggi, C. de Leitenburg, A. Trovarelli, *Catal. Today* **2012**, *181*, 108.
- [122] S. K. Meher, G. R. Rao, *J. Chem. Sci.* **2014**, *126*, 361.
- [123] J. Liu, Z. Zhao, J. Wang, C. Xu, A. Duan, G. Jiang, Q. Yang, *Appl. Catal. B* **2008**, *84*, 185.

- [124] M. A. Peralta, V. G. Milt, L. M. Cornaglia, C. A. Querini, *J. Catal.* **2006**, *242*, 118.
- [125] G. Zhang, Z. Zhao, J. Liu, G. Jiang, A. Duan, J. Zheng, S. Chen, R. Zhou, *Chem. Commun.* **2010**, *46*, 457.
- [126] A. Trovarelli, *Comment. Inorg. Chem.* **1999**, *20*, 263.
- [127] W. I. Hsiao, Y. S. Lin, Y. C. Chen, C. S. Lee, *Chem. Phys. Lett.* **2007**, *441*, 294.
- [128] W. Huang, *Top. Catal.* **2013**, *56*, 1363.
- [129] N. Du, H. Zhang, B. G. Chen, X. Y. Ma, D. R. Yang, *J. Phys. Chem. C* **2007**, *111*, 12677.
- [130] T. S. Sreeremya, K. M. Thulasi, A. Krishnan, S. Ghosh, *Ind. Eng. Chem. Res.* **2012**, *51*, 318.
- [131] D. Ariosa, F. Elhordoy, E. A. Dalchiele, R. E. Marotti, C. Stari, *J. Appl. Phys.* **2011**, *110*.
- [132] X. Mathew, J. P. Enriquez, C. Mejia-Garcia, G. Contreras-Puente, M. A. Cortes-Jacome, J. A. T. Antonio, J. Hays, A. Punnoose, *J. Appl. Phys.* **2006**, *100*.
- [133] N. S. Ramgir, I. S. Mulla, K. P. Vijayamohanan, *J. Phys. Chem. B* **2005**, *109*, 12297.
- [134] K. Maaz, S. Karim, M. Usman, A. Mumtaz, J. Liu, J. L. Duan, M. Maqbool, *Nanoscale Res. Lett.* **2010**, *5*, 1111.
- [135] S. Navaladian, B. Viswanathan, T. K. Varadarajan, R. P. Viswanath, *Nanoscale Res. Lett.* **2009**, *4*, 181.
- [136] S. W. Yang, L. Gao, *J. Am. Chem. Soc.* **2006**, *128*, 9330.
- [137] Z. Wu, M. Li, S. H. Overbury, *J. Catal.* **2012**, *285*, 61.
- [138] J. Li, G. Lu, H. Li, Y. Wang, Y. Guo, Y. Guo, *J. Colloid Interface Sci.* **2011**, *360*, 93.

- [139] S. Bernal, J. J. Calvino, M. A. Cauqui, J. M. Gatica, C. Larese, J. A. P. Omil, J. M. Pintado, *Catal. Today* **1999**, 50, 175.
- [140] R. J. Gorte, S. Zhao, *Catal. Today* **2005**, 104, 18.
- [141] P. Miceli, S. Bensaid, N. Russo, D. Fino, *Nanoscale Res. Lett.* **2014**, 9.
- [142] P. Bharali, P. Saikia, B. M. Reddy, *Catal. Sci. Technol.* **2012**, 2, 931.
- [143] K. C. Remani, S. Ghosh, *Trans. Indian Ceram. Soc.* **2009**, 68, 185.
- [144] B. Wang, J. Hao, H. Li, *Dalton Trans.* **2013**, 42, 5866.
- [145] Nanotechnology Research Directions: IWGN Workshop Report, Vision for Nanotechnology R&D in the Next Decade, Interagency Working Group on Nanoscience, Engineering and Technology (IWGN), US. **1999**.
- [146] S. U. S. Choi, *Heat Transfer Eng.* **2008**, 29, 429.
- [147] Q. Yu, Y. J. Kim, H. Ma, *Appl. Phys. Lett.* **2008**, 92.
- [148] R. E. Rosensweig, *New York: Cambridge University Press* **1985**.
- [149] V. Sridhara, L. N. Satapathy, *Nanoscale Res. Lett.* **2011**, 6, 1.
- [150] J. Taha-Tijerina, T. N. Narayanan, G. Gao, M. Rohde, D. A. Tsentalovich, M. Pasquali, P. M. Ajayan, *Acs Nano* **2012**, 6, 1214.
- [151] J. C. Maxwell, *Clarendon Press, Oxford* **1873**.
- [152] C. Choi, H. S. Yoo, J. M. Oh, *Curr. Appl. Phys.* **2008**, 8, 710.
- [153] S. K. Das, N. Putra, P. Thiesen, W. Roetzel, *J. Heat Trans.-T. ASME* **2003**, 125, 567.
- [154] X. Li, D. Zhu, X. Wang, *J. Colloid Interface Sci.* **2007**, 314, 749.
- [155] S. U. S. Choi, Z. G. Zhang, W. Yu, F. E. Lockwood, E. A. Grulke, *Appl. Phys. Lett.* **2001**, 79, 2252.
- [156] D. Li, W. Xie, W. Fang, *Nanoscale Res. Lett.* **2011**, 6.

- [157] L. Chen, H. Xie, *Colloids Surf. A* **2009**, 352, 136.
- [158] W. Yu, H. Xie, L. Chen, Y. Li, *Colloids Surf. A* **2010**, 355, 109.
- [159] D. Li, B. Hong, W. Fang, Y. Guo, R. Lin, *Ind. Eng. Chem. Res.* **2010**, 49, 1697.
- [160] J. Yin, X. Xia, L. Xiang, X. Zhao, *Carbon* **2010**, 48, 2958.
- [161] S. S. Botha, P. Ndungu, B. J. Bladergroen, *Ind. Eng. Chem. Res.* **2011**, 50, 3071.
- [162] M. S. L. Kundan, *Int. J. Theoretical Appl. Res. Mech. Eng.* **2013**, 2, 2319
- [163] M. Kole, T. K. Dey, *Appl. Therm. Eng.* **2013**, 56, 45.
- [164] H. E. Patel, K. B. Anoop, T. Sundararajan, S. K. Das, *Bull. Mater. Sci.* **2008**, 31, 387.
- [165] M. T. Lopez-Lopez, J. D. G. Duran, A. Delgado, F. Gonzalez-Caballero, *J. Colloid Interface Sci.* **2005**, 291, 144.
- [166] A. Ahniyaz, Y. Sakamoto, L. Bergstrom, *Cryst. Growth Des.* **2008**, 8, 1798.
- [167] Jaehoon Kim, Y. S. Park, Bambang Veriansyah, J. D. Kim, Y.W. Lee, *Chem. Mater.* **2008**, 20, 6301.
- [168] P. D. Shima, J. Philip, B. Raj, *J. Phys. Chem. C* **2010**, 114, 18825.
- [169] X. Xu, X. Wang, *Nano Res.* **2009**, 2, 891.

Definition of the present problem

Cerium dioxide due to its applications in a vivid landscape of areas by virtue of its unique properties made its own place among inorganic oxides and is really appreciated both by industry and academic people. As evidenced from the above scientific literature and other business reports, ceria nanostructures and surface modified oleophilic ceria NPs have great scope for application in various potential areas. Morphology controlled synthesis of ceria nanostructures and its application in catalysis and polishing of glass is well documented in the literature. But a proper understanding of the mechanism behind these applications is still lacking. As pointed out, the need to explore and understand the structure-property correlation in these nanomaterials inevitable for the wide scale commercial applications of this material. The preparation of surface modified monodisperse ceria NP's is also well covered in the open literature but the application studies of such NP's were seldom reported.

Summing up in brief the work under taken in this thesis can be divided as follows.

1. Morphology controlled synthesis of ceria nanostructures through simple wet chemical methods and development of a simple reflux method in presence of surfactant to prepare oleophilic NPs.
2. Two possible applications such as glass polishing and high temperature oxidation of soot have been probed thoroughly to study the effect of NP morphology and related parameters on these applications.

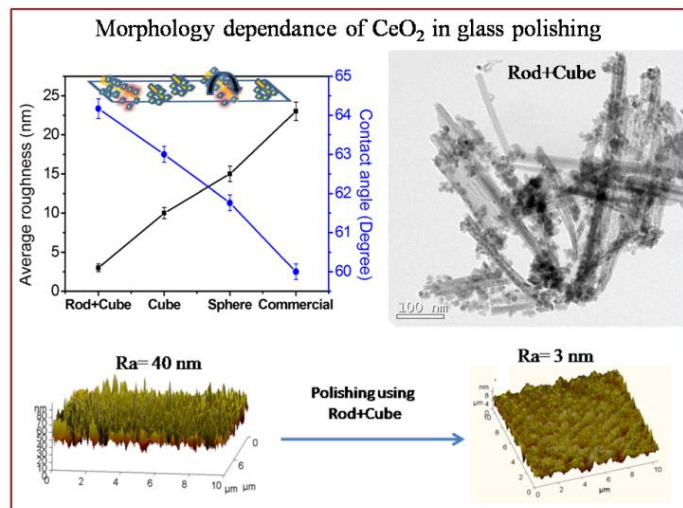
3. The surface modified oleophilic ceria NPs were used for the preparation of stable transformer oil based heat transfer nanofluids.

The thesis has been designed on the above objectives. The results obtained have been discussed and correlations have been derived between the experimental parameters and the properties.

Architecture tuned synthesis of cerium oxide nanoparticles and application in chemical mechanical polishing of glass

2.1 Abstract

Nanosized cerium oxide (CeO_2) particles possessing different morphologies like nanorod, nanocube and nanosphere have been successfully synthesized through facile single step, surfactant free, precipitation technique and by hydrothermal methods. The prepared NPs were further used for fine polishing of silicate glass with an initial surface roughness of 40 nm and observed a strong morphology dependence of abrasive in glass polishing. Polishing efficiency of nanoabrasives in terms of material removal and surface roughness achieved was monitored using a table top lapping machine. Surface roughness analysis as observed by atomic force microscopy reveals that the ceria nanostructure with mixed morphology of rods and cubes could produce a surface finish of $\sim 3 \text{ \AA}$. A summarised graphical abstract of the chapter is also presented below.



The surface properties of abrasive were found to play a key role in polishing as evidenced by X-ray photoelectron spectroscopy and Raman spectral analysis. The amount of Ce^{3+} was found to vary with the shape of ceria NPs attaining a maximum of 42% in mixed morphology abrasive. The preferred orientation of the crystallographic planes have been estimated and expressed as the texture coefficient (C_{hkl}) by performing Harris analysis on XRD data. The powder contact angle/hydrophilicity of the nanoceria abrasives was found to be proportional to the dipolar (200) plane content and concentration of Ce^{3+} . The presence of ~42% Ce^{3+} and (200) texture coefficient value of 1.34 in rod+cube mixed morphology abrasive, helps in efficient polishing. The pH of the polishing slurry was also found to play a key role in glass polishing. This work envisages polishing efficiency with nano CeO_2 slurry in achieving nanolevel planarity on glass substrates which is desirable for the global planarization of complex device topography.

2.2 Introduction

With the advent of nanotechnology, size/shape controlled synthesis of NPs has thrown open an entire field of research. Motivated by both the possible applications and the excellent properties, much attention has been directed to the size/shape controlled synthesis of cerium oxide, ceria (CeO_2) nanostructured materials. As mentioned in chapter I, this endowed inorganic oxide is finding myriad uses especially in glass polishing and catalysis. Currently, the polishing slurry accounts for ~40% of the worldwide nanoparticle market share. Chemically active polishing particles such as CeO_2 , having a large fraction of surface species bonding to the glass, will generate higher frictional forces and higher surface stresses than more inert materials such as diamond. Chemical Mechanical Planarization (CMP) slurries consist of abrasive particles $<3 \mu\text{m}$ in diameter suspended in deionised (DI) water.^[1] These suspended particles in the slurry are responsible for mechanical abrasion, the M in CMP. Highly reactive particles like ceria (CeO_2) and zirconia (ZrO_2) may also contribute to the chemical component via particle–substrate bonding.^[1]

Many technological applications of glass such as displays, microelectronics and advanced lithography are known to depend on the quality of the surface. In addition, clean, smooth, and compositionally reproducible specimen surfaces are desirable for various surface science studies of materials, e.g., corrosion, adsorption, film deposition, etc.^[2] Ceria is the most widely used abrasive for the CMP of silicate glasses and is also used to finish CRT screens, LCDs and also in ophthalmic industry for prescription lens polishing.^[3, 4] CMP appears to be the most promising technology in microelectronic fabrication for the global planarization of complex device surfaces.^[5] Ceria slurries have

stimulated widespread interest because of enhancements in material removal rate, surface finish, and selectivity over slurries formulated with silica abrasives.^[6]

In 1963, Cornish and Watt suggested that glass polishing critically depends upon the presence of water in the polishing slurry.^[7] They reviewed cerium polishing rates relative to water for a series of alcohols ranging from methanol to *n*-dodecanol. Polishing rates were found to increase directly with increasing hydroxyl reactivity, with water giving by far the highest rate. Similarly, in 1971 Silvernail and Goetzing studied cerium polishing rates in a series of ethylene glycol/water mixtures. Polishing rates were extremely low in pure ethylene glycol, increasing logarithmically with the molar concentration of water in solution.^[8] From the above, it is apparent that the interaction of the system with water is the primary chemical process in glass polishing. However, the stabilization of ceria in water is still a big issue to be tackled and use of dispersants is highly appreciated.^[9] The dispersion agents used by manufacturers for preparing commercial CMP slurry are considered to be proprietary and are not disclosed to the users. Luo et al. has studied the stabilization of alumina slurry using different dispersants and found out that addition of polyethylene glycol improves the slurry stability significantly, leading to a stable alumina slurry that can be utilized for the CMP of copper.^[9]

Conventional colloidal silica slurry widely used in the polishing of silicon wafer, contains lots of toxic chemicals and hence the chemical pollution after CMP is still a big concern.^[10] Though both ceria and alumina possess proper chemical and mechanical properties suitable for polishing, enhanced chemical reactivity of ceria make it a much better candidate in glass polishing. Only few papers related to the topic of glass polishing

using nanostructured ceria and their mechanisms have been published in the past decade.^[1, 4, 11-14]

The effect of concentration of ceria abrasive in optical glass polishing is studied by Wang et al. and they have concluded that the material removal rate increases with decrease of ceria concentration.^[3] Mixed abrasive slurry containing alumina/ceria particles evaluated for dielectric CMP performance by Jindal et al. at a slurry pH of 4 demonstrated excellent polish rate and selectivity of oxide over nitride as well as very low RMS surface roughness values of 1 nm, making them attractive candidates for the STI CMP process.^[15] In glass polishing, both polishing rates and surface smoothness are maximized in the pH range 9.5-10, where 50% of surface silanols are dissociated.^[16, 17]

Though few reports are available on the effect of pH,^[10] slurry consistency^[3] and particle size,^[5, 18] no detailed study was carried out on the morphology dependent polishing efficiency and mechanism of glass polishing using nanoceria. A number of researchers have studied the influence of abrasive particle size on the material removal rate and surface finish. Some have observed that the polishing rate increases with both particle size and concentration,^[19, 20] while others claim that a decreased particle size led to higher polishing rates,^[21] or have no effect on polishing rate.^[1] Though the effect of individual crystal shape of abrasive on polishing has been suggested by Kirk et al. no detailed study have been reported to unravel the mechanism of morphology dependant glass polishing.^[12]

Most of the research efforts in CMP are focused in the areas of slurry formulation and particle properties. A tremendous potential for commercialization exists in CMP slurry manufacturing. In less than ten years the CMP slurry market has grown from non-

existent to a billion dollar enterprise. Currently, the polishing slurry accounts for ~40% of the worldwide nano-particle market share. These facts are promising for industrial companies or the researchers who develop marketable CMP slurry. However, for the academic researcher, the tremendous profitability has led to reluctance to release proprietary information, which complicates efforts to understand CMP fundamentals. What is available in the open and patent literature does not sufficiently explain CMP mechanisms. Fundamental investigations into slurry properties are necessary, especially in a setting where a sustained effort can be maintained. Considerable room exists in the academic arena to contribute to the knowledge of CMP slurry development, particularly in areas like Shallow Trench Isolation (STI) that will be gaining attention in the near future.

In the present work, we have focused on the morphology dependent synthesis of anisotropic shapes of ceria such as rods, cubes and spherical shape by hydrothermal as well as precipitation methods all starting from cerium nitrate hexahydrate as the precursor. The prepared NPs were utilized as polishing slurry in glass polishing and a detailed study on the surface properties of the abrasives has been carried out. The effect of morphology of abrasive, pH and solid content of slurry in glass polishing have been systematically carried out. The present work gives new insight into the morphology dependent glass polishing mechanisms.

2.3 Experimental Section

Materials: The starting chemicals employed in the syntheses were $\text{Ce}(\text{NO}_3)_3 \cdot 6\text{H}_2\text{O}$ (>99.9%, Indian Rare Earths Ltd., India) and the precipitants NaOH (analytical grade, Qualigens Fine Chemicals, India), NH_4OH (25%, analytical grade, Qualigens Fine

Chemicals, India). A commercial ceria powder was procured from Kansal enterprises, New Delhi. All the chemicals were used as received without further purification. All the chemical syntheses and washings were carried out using double distilled water obtained from a quartz glass distillation unit.

2.3.1 Synthesis

Ceria NPs possessing different morphologies such as sphere, cube and rod were synthesized by means of simple ammonia precipitation and hydrothermal method respectively.

a) Precipitation using ammonia

Small crystals of spherical cerium oxide (**AP**) were synthesized by ammonia precipitation using 0.5 M $\text{Ce}(\text{NO}_3)_3 \cdot 6\text{H}_2\text{O}$ (CN) aqueous solutions by salt into precipitant (SIP) technique^[22, 23] in which ammonia is used as the precipitant. In a typical synthesis, CN solution (29 mmol) was added to 25% ammonia in a 2 L beaker so that the total volume of the reaction mixture was 580 mL. The net concentration of Ce-ion was 500 mM and the hydroxyl/cerium ratio (OH/Ce) in solution was greater than 10:1. The CN solution was added at a uniform rate in 1 min under vigorous mechanical stirring using a 1/8 hp mechanical stirrer at ~4000 rpm. The reaction was carried out at 30°C (room temperature). A purple coloured precipitate formed within minutes after the addition of CN solution. The precipitate turned to yellow on stirring further ~20 min indicating the formation of CeO_2 crystals. The stirring was continued for 3 h. The ceria precipitate was then collected by centrifugation and the excess ammonia was washed off with distilled water till the pH of the supernatant liquid was <8. The centrifuged mass was then washed

twice with dry ethanol and dried in an air oven overnight at 65°C and termed henceforth as **AP**.

b) Hydrothermal synthesis

Nanorods and nanocubes of ceria were prepared by hydrothermal method by varying the hydrothermal treatment temperature and concentration of precipitant. For the nanorod formation, cerium hydroxide was precipitated from 0.5 M cerium nitrate hexahydrate solution using 8 M sodium hydroxide solution. In this case, a cerium nitrate precursor solution was prepared by dissolving CN (0.29 mole) in distilled water (150 mL). A precipitant solution was also prepared by dissolving NaOH (4.65 mole) in distilled water (431 mL). The two aqueous solutions were then mixed and stirred strongly for 30 min in a 2 L polypropylene beaker. On mixing, the net Ce-ion concentration was ~500 mM. Subsequently, the milky reaction mixture was transferred into a 1 L Teflon lined autoclave vessel and the autoclave was sealed tightly. The precipitate was hydrothermally treated at 120°C. After 24 h hydrothermal treatment, the autoclave reactor was cooled and depressurised to room temperature naturally. The CeO₂ precipitate was then collected by centrifugation. The precipitate was washed with distilled water till the pH of the supernatant liquid was 7.5. The collected solid was then washed with ethanol twice. The washed precipitate was dried in an air oven at 65°C overnight and will henceforth be called as **HT1**.

Synthesis of ceria nanocubes: Cerium oxide nanocubes were synthesised by autoclaving the freshly precipitated slurry at 180°C, following a modified method described for synthesising CeO₂ nanorods. Three modifications were introduced: (i) use of 5 M concentration of NaOH in the reaction mixture; (ii) lower hydroxyl/cerium ratio

(OH/Ce) of 9.7:1 instead of 16:1; and (iii) autoclaving temperature was raised to 180 from 120°C. The final products were washed with distilled water until excess alkali was removed and dried at 65°C. This product is denoted as **HT2**.

A commercial ceria powder extensively used in glass polishing industry was also included in the present study for comparison which will be abbreviated as **CC**.

2.3.2 Slurry preparation

Previously weighed CeO₂ nanopowder and Carboxy methyl cellulose (CMC) as dispersant was added to 100 ml distilled water and stirred mechanically at 3000 rpm for 2h.

2.3.3 Surface treatment of microscopic glass

The microscopic glass slides were cut into small pieces of 1×1 cm² area and was cleaned by sonicating in water and ethanol alternatively for several times and dried. To induce a desired roughness on the glass substrate, chemical etching using 5% hydrofluoric acid (HF)^[24] has been carried out. This chemically etched rough glass surface was used for all further polishing studies.

2.3.4 Polishing study on glass substrate

A table top lapping machine (Buehler, Germany) was used for polishing purpose. The total mass removal from glass substrate by polishing against a rotating disc as a function of time when slurry containing nanosized CeO₂ abrasives is poured on the rotating disc uniformly was measured. The diameter of the rotating disc of the polishing machine is ~20 cm and was covered with a Selvyt Polishing Cloth. A new polishing pad was used for every different polishing slurry. No pre-treatment, such as diamond conditioning, was performed. Since the slurry was used for a single pass (as opposed to

recirculation), changes of particle size distribution (PSD) in the slurry with recirculation are not considered in this study. Microscope glass slides of thickness ~ 2 mm were used for polishing against wet cloth in presence of the slurry of nanosized CeO_2 . The speed of rotation used was kept constant at 150 rpm for all the polishing experiments. The glass substrate was held at a point close to the periphery of the polishing disc. Slurry of ceria powders with consistency 1-10 wt% was used as abrasive for polishing the glass substrate and was poured on to the disc (close to the point where the glass substrate is held) at a rate of $\sim 10 \text{ ml}\cdot\text{min}^{-1}$.

2.4 Results and discussion

2.4.1 Electron microscopy

Detailed morphological and structural analyses of the samples was undertaken using bright field high-resolution TEM, typical results are shown in Fig. 2.1. In the precipitation approach, the NPs are slightly agglomerated (Fig. 2.1E) compared to the hydrothermally synthesized one (Fig. 2.1A&C). This may be due to the formation of hydrogen bonds between water molecules adsorbed on approaching grains. As reported by Yang et al., the hydrothermal process at boiling temperature is effective to dehydrate the adsorbed water and decrease the hydrogen bonding effect leaving the weakly agglomerated powders of hydrated ceria.^[25] The CeO_2 NPs in AP are found to be almost spherical. The mean particle size (D_{TEM}) in AP is 8.2 nm ($D_{\text{XRD}} = 7$ nm) as shown in Fig. 2.1E-F. Mild hydrothermal treatment at 120°C with a high base concentration (8 M) produced predominantly nanorods (HT1) from anisotropic growth of unstable $\text{Ce}(\text{OH})_3$ nuclei, governed by dissolution recrystallisation mechanism.^[26] When the autoclave temperature was increased to 180°C (HT2) nanocubes were formed. The average sizes from TEM (D_{TEM}) for HT2 is 13.5 ± 2.5 nm.

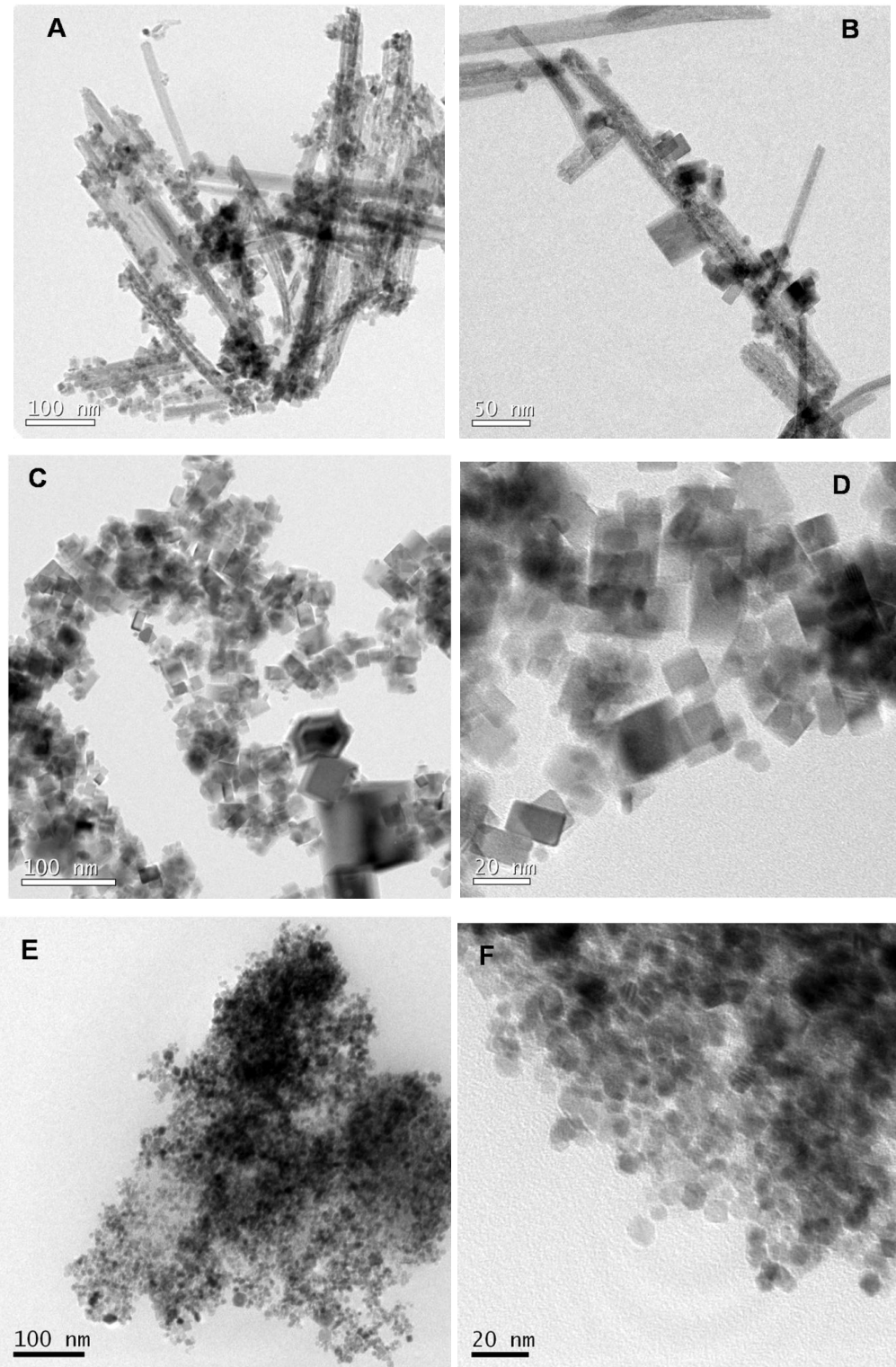


Fig. 2.1 TEM image of hydrothermally synthesised CeO₂ crystals. (A, B) HT1 containing nanorods and cubes autoclaved at 120°C. (C, D) HT2 containing cubes and (E, F) AP containing spheres.

The mixed morphology of HT1 is clear from the TEM analysis and detailed analysis of multiple images (e.g., Fig. 2.1A) reveals that it contains ~28.1% (number) nanorods with an average length of ~370 nm and diameter ~24 nm, that is, an aspect ratio of ~15. This equates to an average (equivalent sphere) diameter of 64.3 nm. The remaining 71.9% are nanocubes with an average edge length of ~20.2 nm. By volume (or mass) the sample is approximately 88.8% rods and 11.2% cubes.

2.4.2 X-Ray diffraction analysis

XRD patterns of the three samples HT1, HT2 and AP can be readily indexed to a pure fluorite cubic phase (space group: Fm3m) of CeO₂ with lattice constant of 0.5411 nm (JCPDS 34-0394)^[27] as shown in Fig. 2.2.

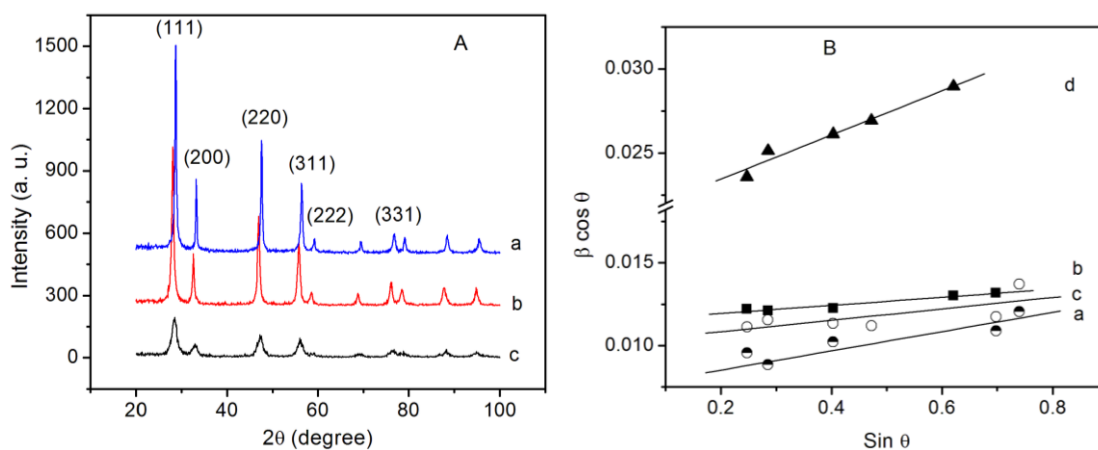


Fig. 2.2 A) X-ray diffraction patterns and B) Williamson-Hall plots of CeO₂ powders a) HT1, b) HT2 c) AP and d) CC.

The average crystallite size of the nanocrystalline ceria powders were evaluated from line-profiling of prominent X-ray diffraction peaks using the Williamson-Hall approach^[28] and was found to be 19, 14.1, 7 and 15.8 nm respectively in HT1, HT2, AP

and CC. There is moderate broadening of the diffraction peaks in AP, which suggests smaller crystals in this sample. Williamson-Hall plots for all the nanocrystalline CeO₂ powders are shown in Fig. 2.2B.

2.4.3 Dispersant optimization and stability of slurry

The change in apparent viscosity of 5 wt% ceria dispersions stabilized using CMC at natural pH of the slurry which was measured as 6.1 is presented in Fig. 2.3A. The viscosity was found to decrease initially, reaching a minimum value with 1 wt% CMC and further increases with increasing the concentration of dispersant.

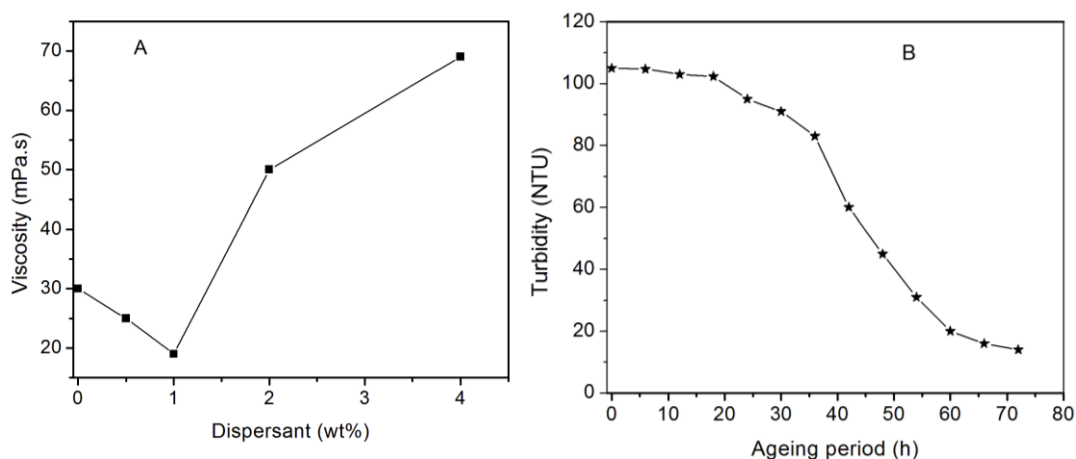


Fig. 2.3 A) Viscosity of ceria slurry as a function of concentration of CMC, B) Turbidity measurement of 1 wt% CMC added ceria slurry.

A similar effect was observed by Kuo et al. in silica based slurry in presence of several polymeric dispersants.^[29] The increase in viscosity beyond 1 wt% dispersant may be due the presence of large number of ions in the solution phase which enhances the charge shielding to compress the electrical double layer around the particles. The stability of the polishing slurry was monitored by performing ageing studies by measuring turbidity (transmittance of visible light) over a time period of 3 days and presented in Fig. 2.3B. The slurry was visibly stable at room temperature for ~1 day without changing their

appearance, and after this period settling was observed which is corroborated by the sharp fall in turbidity values as shown in Fig. 2.3B.

2.4.4 Polishing studies on glass

2.4.4.1 Surface treatment of microscopic glass

Chemical etching using hydrofluoric acid (HF) proved to be an efficient way to induce roughness on ceramic substrates.^[24] The surface topography of the glass substrate before and after chemical etching is presented as 3D AFM images shown in Fig. 2.4. The average surface roughness of microscopic glass slide was found to be 7 nm which increased to 40 nm, higher than that reported by Zogheib et al. on etching using 5% HF for 90 s. This may be due to a change in etching mechanisms according to the type of the ceramic microstructure and composition. HF reacts with the glass matrix that contains silica and forms hexafluorosilicates which is selectively removed and the crystalline structure gets exposed. As a result, the surface of the ceramic becomes rough.^[24]

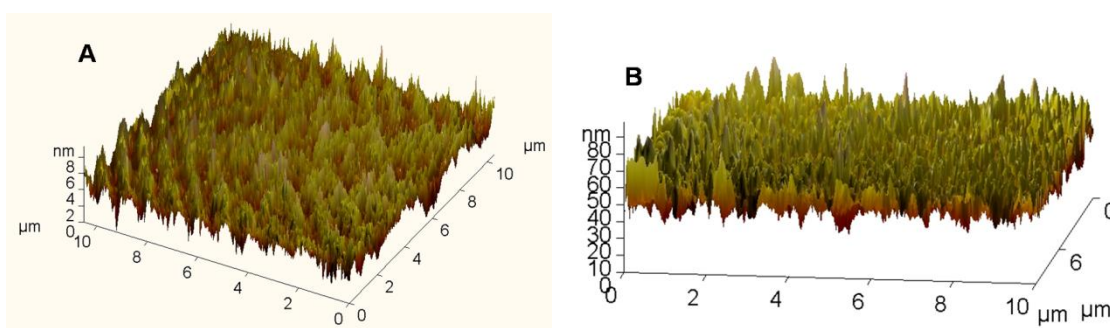


Fig. 2.4 AFM 3D images of microscopic glass A) before and B) after etching.

This chemically etched rough glass substrate (Fig. 2.4B) was used for all further polishing studies.

SEM analysis of etched glass substrate

The SEM micrographs clearly revealed the effect of the HF etching on the microstructure of the glass substrate (Fig. 2.5). Fig. 2.5B (glass etched for 90 s) clearly show minor

surface disruptions compared to Fig. 2.5A (glass without any acid treatment) which was corroborating the R_a values observed from the AFM images in Fig 2.4A &B.

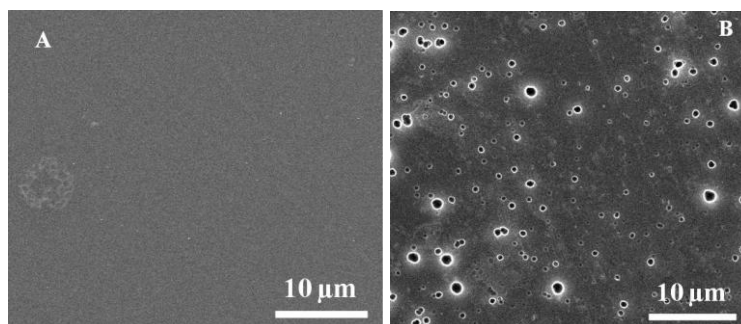


Fig. 2.5 SEM images of glass before and after HF etching (A and B) respectively.

2.4.4.2 Characterization of polished glass surface

Typical 3D AFM images of glass polished using ceria abrasive HT1, HT2, AP and a commercial ceria powder used for glass polishing (CC) is shown in Fig. 2.6 and the respective R_a values are graphically presented in Fig. 2.7A.

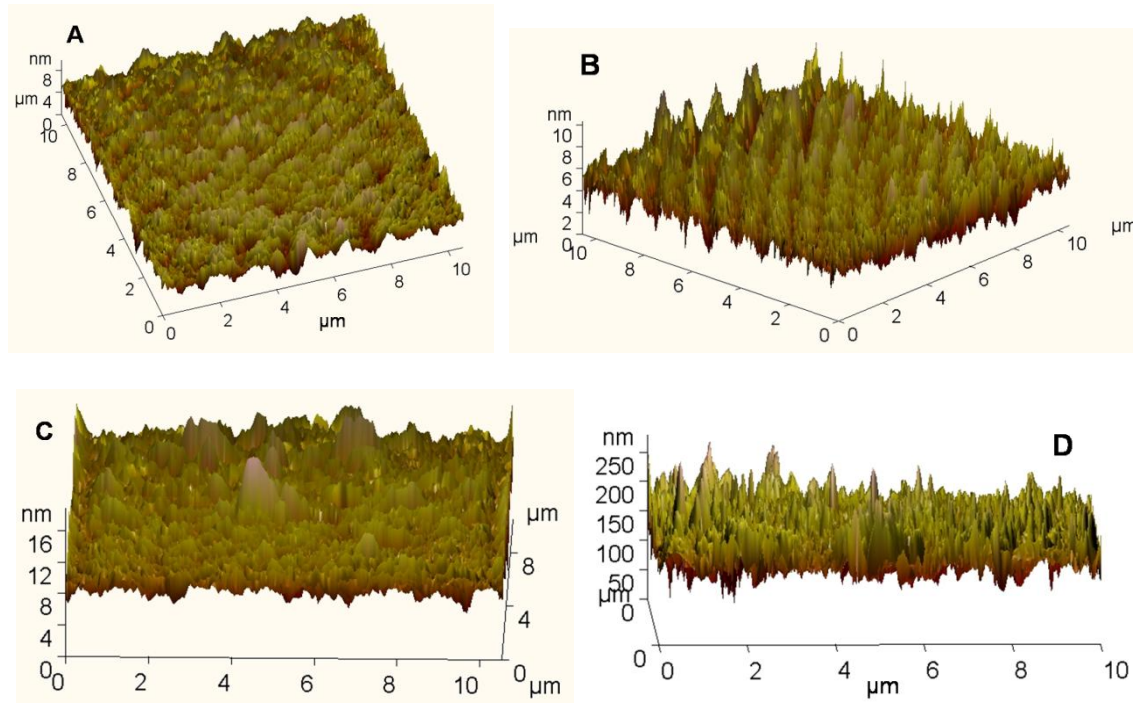


Fig. 2.6 AFM images of glass slides polished using 5 wt% slurry of A) HT1, B) HT2, C) AP and D) CC.

The "error bars" represent the spread in the results of five repeat experiments. HT1 having mixed morphology of rods and cubes seemed to be most efficient in producing smooth surface with an average surface roughness (Ra) of 3 nm followed by HT2 and AP.

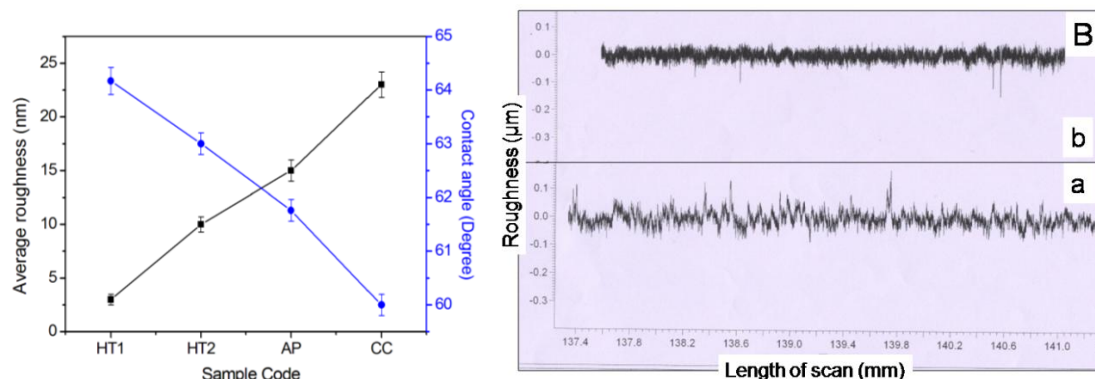


Fig. 2.7 A) Surface roughness analysis and water contact angle of glass slide polished using 5wt% slurry of ceria abrasives. A schematic of HT1 polishing a glass substrate is shown as inset. B) Surface profiles of glass a) before polishing showing a Ra value of 50 nm and b) after polishing using HT1 showing Ra value of 8 nm.

In terms of its high specific surface area of $134 \text{ m}^2 \cdot \text{g}^{-1}$, AP is expected to possess better polishing efficiency compared to the other abrasives included in the present study (Table 2.1). This may be explained in terms of the transient soft agglomerate formation in the CMP slurries which is expected to be higher in fine spherical particles in AP.^[30] Such agglomerates can cause defects on the substrate which is to be polished. Indeed, it was reported previously that the commercial CMP slurries tend to coagulate and partially disperse during the polishing process, confirming the presence of these agglomerates.^[30] The profilometry data (Fig. 2.7B) further supports the AFM results as evidenced by the Ra value of 50 nm for chemically etched glass and 8 nm for glass polished using HT1. The water contact angle values of the glass slides measured by dynamic contact angle

method presented in Fig. 2.7A further elucidates the increase in water contact angle values with reduction in surface roughness. The water contact angle value increases from 60 to 64° as we move from CC to HT1 which was in accordance with the Wensels law of contact angle as shown in Fig. 2.7A. According to the law, the effect of roughness on contact angle is to decrease the contact angle for a wettable/hydrophilic glass surface.^[31]

The material removal rate of different ceria abrasives is shown in Fig. 2.8. Next to CC, HT1 containing mixed morphology of rods and cubes exhibited the highest material removal rate of $0.18 \text{ mg.cm}^{-2}.\text{min}^{-1}$ which is followed by HT2 and finally AP.

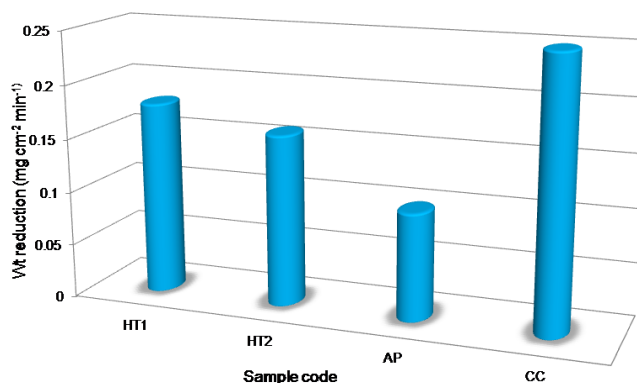


Fig. 2.8 Material removal rate in terms of weight reduction of the glass substrate as a function of morphology of ceria abrasive.

This can be attributed to the synergistic chemical and mechanical effect of ceria abrasive in polishing. Agglomerated commercial ceria powder due to the large effective particle size appeared to be better in material removal, though the surface finish was poor ($Ra \sim 26 \text{ nm}$).

2.4.5 Role of Ce^{3+} /defects: XPS and Raman spectral analysis

The morphology dependence of nanoceria abrasive in glass polishing is further supported by XPS and Raman spectral analysis as shown in Fig. 2.9 and 2.10 which gives new insight into the surface properties of the abrasive.

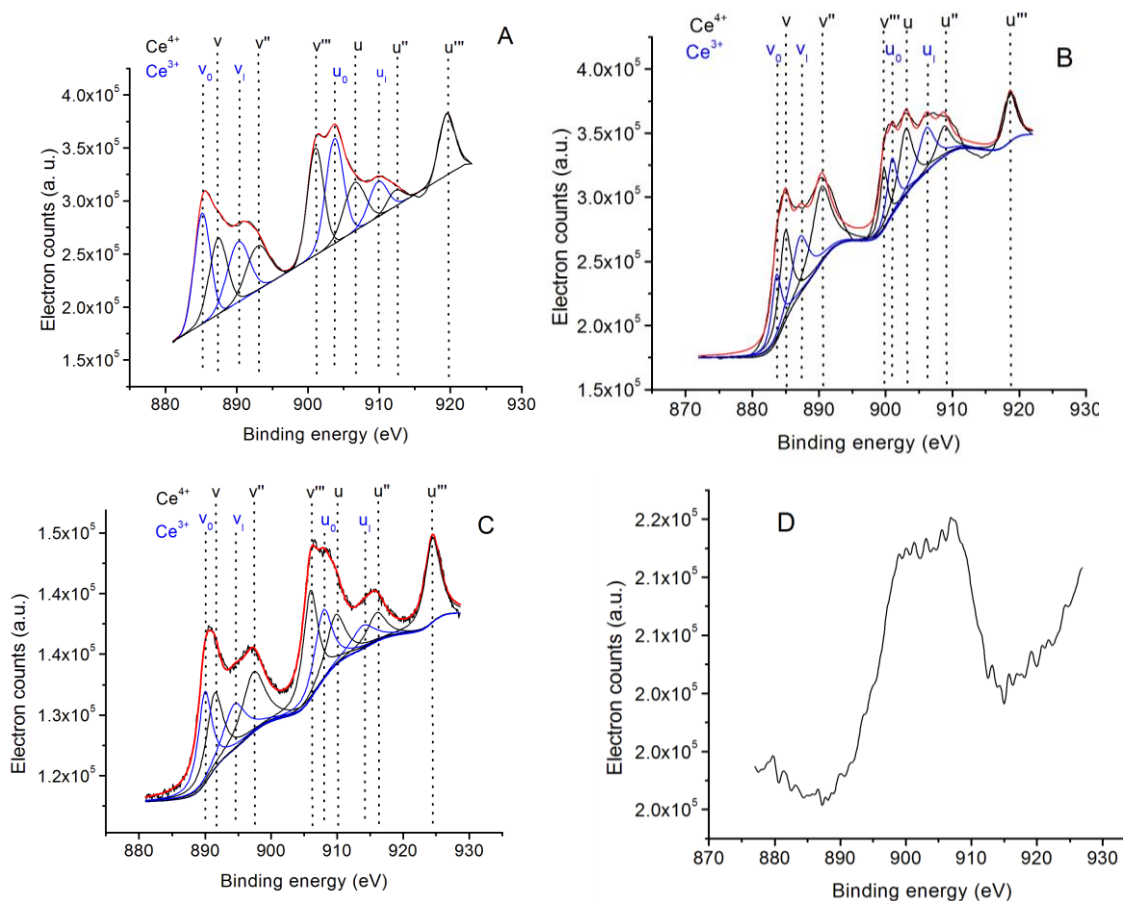
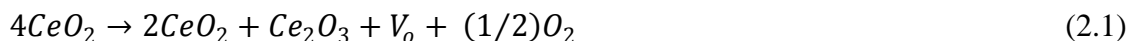


Fig. 2.9 Ce 3d XPS pattern of A) HT1, B) HT2, C) AP and D) CC.

In the Ce 3d spectrum of XPS (Fig. 2.9), v₀, v₁, u₀, and u₁ peaks are attributed to Ce^{3+} ; while v, v'', v''', u, u'' and u''' are the characteristic peaks of Ce^{4+} ions. The Ce^{3+} content is estimated using the integrated area of each peak in deconvoluted Ce 3d spectrum as 42.1, 31.4 and 22.2% in HT1, HT2 and AP respectively (Table 2.1). The Ce 3d spectrum of commercial ceria was not resolvable as it contains dopant cations as impurity (Fig. 2.9D).

It is well-known that the presence of Ce^{3+} in the fluorite lattice generates oxygen vacancies to maintain charge balance^[32, 33] as shown in equation 2.1.



where V_o is the vacancy generated by the presence of Ce^{3+}

The presence of surface oxygen vacancies in the materials was monitored by UV-Raman spectroscopy (Fig. 2.10) which shows the presence of peaks at 460, 560 and 600 cm^{-1} , marked as γ , α and β respectively. The main peak at ca. 460 cm^{-1} is due to the F_{2g} mode vibration of cubic fluorite structure in CeO_2 .^[34] The phonon modes at 560 and 600 cm^{-1} are characteristic of oxygen vacancies in ceria system.^[32, 34, 35]

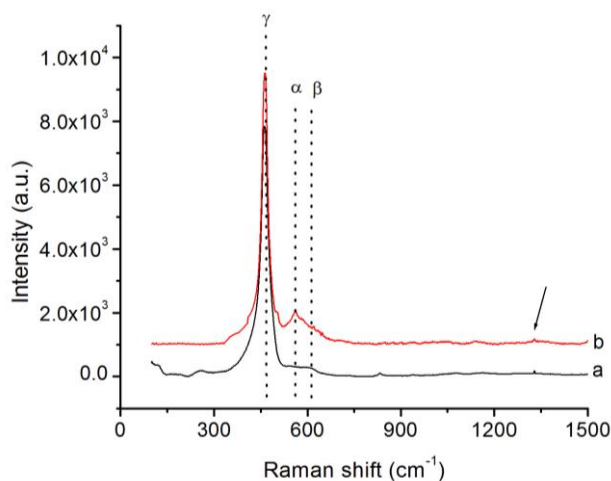


Fig. 2.10 Raman spectra of a) AP and b) HT1.

The relative density of defect sites ($\sim 560\text{ cm}^{-1}$) in nanoparticulate CeO_2 was higher in HT1 compared to that in AP.^[36] The peak at $\sim 1340\text{ cm}^{-1}$ was due to $O_2^{\delta-}$ ($0 < \delta < 1$) species as indicated with arrowhead in Fig. 2.10.

2.4.6 Mechanism of glass polishing

Material removal from the glass surface has been proposed to occur by three basic mechanisms: (1) fracturing, (2) plastic flow, and (3) chemical reaction.^[13] When the load

on the substrate is very low as in the present case, the material removal mechanism is predominantly chemical which proceeds through condensation and hydrolysis reactions as proposed initially by Cook.^[37] According to Cook, the hydration layer present on the ceria abrasives contains Ce–OH groups, which react with the active –Si–O– sites on the silicon dioxide surface to form Ce–O–Si structures. As the Si–O–Si links in silicon dioxide are weaker than the Ce–O–Si bonds, the formers are ruptured during polishing due to the mechanical action of the rotating pad. The general glass polishing mechanism is schematically represented in Fig. 2.11. Further, as suggested by Cook and Kelsall et al., more Ce³⁺ on the surface of abrasive in slurry could be beneficial for the CMP process due to the ease of forming a Ce(OH)₃ hydration layer which would accelerate the process of CMP.^[10, 38]

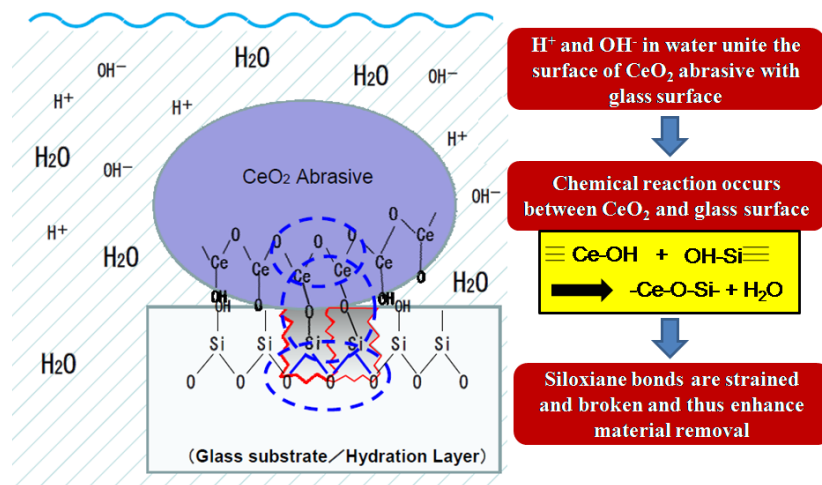


Fig. 2.11 Schematic diagram showing mechanism of glass polishing with ceria abrasives.

Later, Sabia and Stevens postulated that an increase in the number of active sites on the ceria abrasives due to the reduction of Ce⁴⁺ to Ce³⁺ might be responsible for the bonding between Ce³⁺ on the ceria abrasives and silicon dioxide.^[39] Recently Babu et al. observed that silicon nitride and silicon dioxide removal rates can be controlled by varying the

number of reactive Ce^{3+} species on the surface of ceria particles.^[38] We also observed a similar trend in which better polishing efficiency in terms of surface quality and material removal rate was observed with HT1 possessing 42% Ce^{3+} on the surface.

2.4.7 Hydrophilicity of nanoabrasives

Further we measured the contact angle of nanoabrasive powders as it is known that chemical reaction at a liquid–solid interface depends on their contact angle.^[10, 29] The wettability of the powders was evaluated by dynamic water contact angle measurements done in triplicate and the average value was found to be 60° , 79° , 87° and 90° in the case of rod-cube, cube, spheres and commercial ceria respectively. We attribute this variation in contact angle to i) change in morphology ii) which in turn change $[\text{Ce}^{3+}]$ and iii) predominance of polar (200) surface. The surface interaction with water is strongly dependent on the ceria oxidation state: no chemisorbed water is present above 300 K for fully oxidized ceria (Ce^{4+}), but chemisorbed water and hydroxyls persist up to 500 K for reduced ceria (Ce^{3+}).^[40] Hence a reduced ceria surface promotes dissociation of water, which in turn leads to enhanced formation of Si–OH bonds that break up the Si–O bonds at the glass surface.^[40] A similar report by Martinez et al. suggests that the overall positive charge of defective oxides allows water to be bounded to the structure which makes such systems more hydrophilic.^[41] In accordance with Bentley et al. and Martinez et al. we observed that HT1 containing 42% Ce^{3+} is relatively more hydrophilic as evidenced by a powder contact angle value of 60° . The (200) surface in ceria is a Type III dipolar surface as shown in Fig. 2.12.

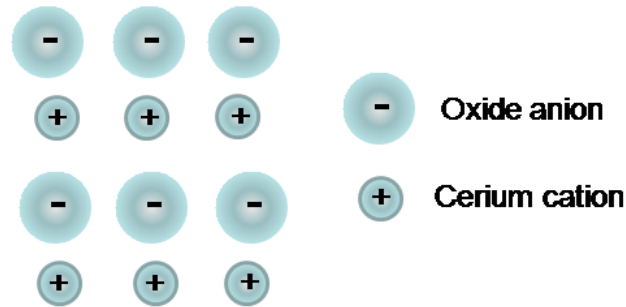


Fig. 2.12 A dipolar (200) surface of CeO_2 .

Type III surfaces consist of alternating layers of cerium cations and oxide anions. Consequently, irrespective of where along the unit cell the surface is terminated, there is a dipole in the z -direction. Datye et al. observed distinct $-\text{OH}$ stretching bands for nanoshapes such as rods, cubes and octahedra which they correlated with different surface terminations/ exposed planes of the nanostructures. Further, they observed that $\{100\}$ terminated nanostructures possess specific hydroxyl bands more strongly than $\{111\}$ terminated structures indicating their enhanced hydrophilicity.^[42]

The preferred orientation of the polar crystallographic plane (200) was estimated by performing Harris analysis on the XRD data of CeO_2 powders^[43, 44] and expressed as the texture coefficient $C(h_i k_i l_i)$, following the equation:

$$C(h_i k_i l_i) = \frac{I(h_i k_i l_i)}{I_o(h_i k_i l_i)} \left[\frac{1}{n} \sum \frac{I(h_i k_i l_i)}{I_o(h_i k_i l_i)} \right]^{-1} \quad (2.2)$$

where $I(h_i k_i l_i)$ is the diffraction intensity of the $(h_i k_i l_i)$ plane of the particular sample under investigation, $I_o(h_i k_i l_i)$ is the intensity of the $(h_i k_i l_i)$ plane from the standard JCPDS powder diffraction pattern for the corresponding peak i , and n is the number of reflections taken in to account. A sample with randomly oriented crystallites presents a $C(hkl)$ of 1, while a larger value indicates an abundance of crystallites oriented to that (hkl) plane.

The powder contact angle value of the nanopowders followed the same trend as that of $C(200)$ and $[Ce^{3+}]$ i.e., $HT1 > HT2 > AP > CC$ as tabulated in Table 2.1.

Table 2.1 Characteristics of ceria nanoabrasives used for glass polishing

Sample code	D_{XRD} (nm)	D_{TEM} (nm)	Surface area	Contact angle ($^{\circ}$)	(Ce^{3+}) (%)	I_{200}/I_{111}	$C(200)$
HT1	19	64	22.96	60 ± 1	42.1	0.538	1.34
HT2	14.1	13.5	25.87	79 ± 1.5	31.4	0.453	1.2496
AP	7	8.2	134.19	87 ± 0.7	22.2	0.363	1.0674
CC	15.8	20	5.12	90 ± 1.2	-	0.27 (0.3*)	0.9526

*JCPDS file 34-394

Additionally the I_{200}/I_{111} value calculated for HT1 (Table 2.1) using XRD data was ~79% higher than that for bulk ceria (JCPDS file:34-394) where as the commercial ceria powder followed the same trend as that of bulk ceria. The glass substrate being hydrophilic, a smaller powder contact angle value of 60° in mixed morphology abrasive HT1 accounts for a better interfacial wettability, which enhances the chemical reaction at the solid–liquid interface.^[10]

2.4.8 Effect of solid content of abrasive

The etched glass substrate was polished using HT1 of varying solid consistency from 1-10 wt% for a time period of 10 min. The respective Ra values and contact angle values of the polished glass substrate are graphically presented in Fig. 2.13A. Typical AFM images of glass polished using 1 and 5 wt% slurry is also shown in Fig. 2.13B. The Ra value was found to decrease with increase in solid content and attained a minimum value of 3 nm with 5 wt% slurry.

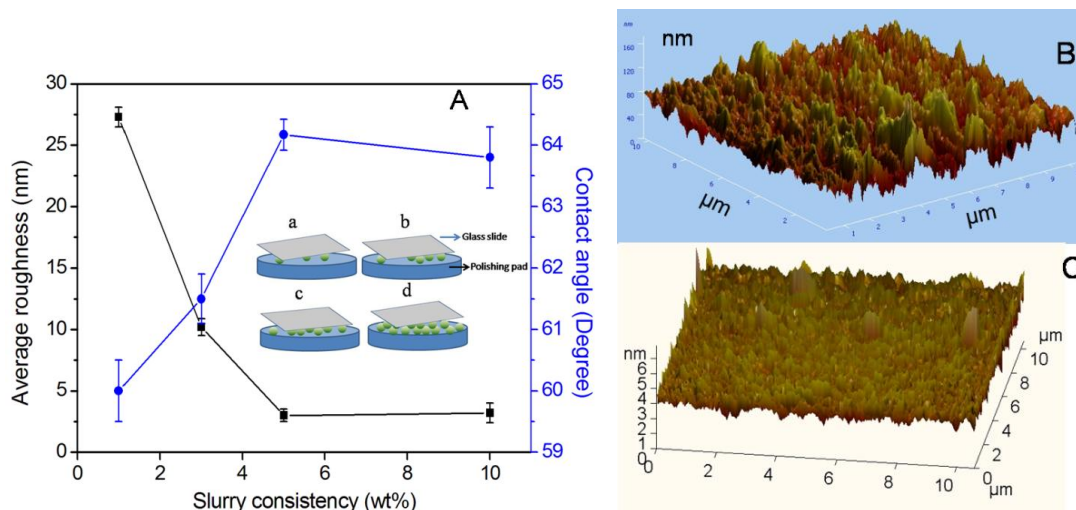


Fig. 2.13 (A) Surface roughness analysis from AFM and water contact angle values of glass polished using 1-10 wt% (a - d in the inset) slurry of HT1. Typical 3D AFM images of glass polished using (B) 1 and (C) 5 wt% slurry.

Further increase in slurry consistency does not show much variation in R_a value as the abrasive particles might have reached a saturation value in between the polishing pad and 1 cm^2 glass substrate as shown in the inset of Fig. 2.13A. This observation was contradictory to that reported by Wang et al., probably because most of the results reported in the literature used concentrated slurries.^[18, 29, 45]

2.4.9 Effect of pH of slurry

The effect of pH of slurry in glass polishing was studied by performing polishing experiments using slurry of HT1 at 4, 6.1 and 10 pH values. The R_a values from AFM analysis versus pH of the slurry is presented in Fig. 2.14A. Detailed study on the electrokinetic properties of polishing slurry and mechanism of glass polishing give new insight into the effect of pH of slurry in glass polishing. The zeta potential versus pH of slurry is shown in Fig. 2.14B. Use of CMC as dispersant in the present study was found

to influence the electrokinetic properties of the ceria slurry as evidenced by zeta potential measurements shown in Fig. 2.14B.

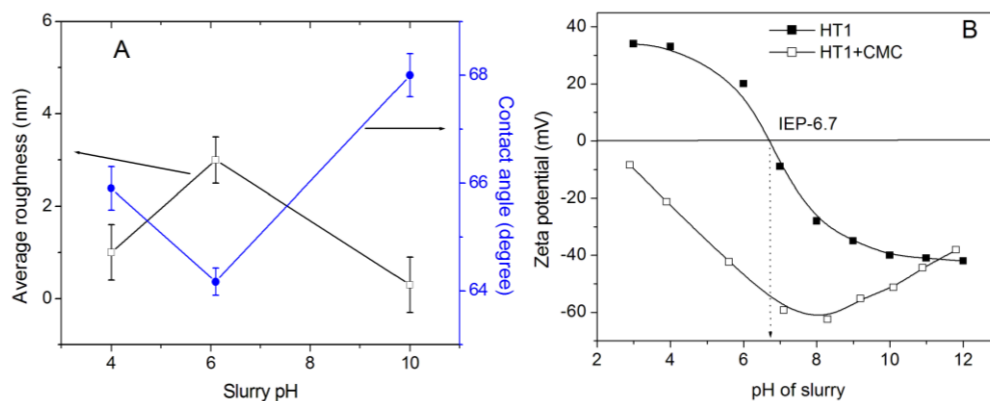


Fig. 2.14 A) The surface roughness analysis and advancing water contact angle of glass polished at pH 4, 6 and 10. B) Zeta potential of ceria slurry as a function of pH without and with CMC.

The Isoelectric point of pure ceria slurry was found to be at pH 6.7 which is in the range reported by others.^[45] CMC is an anionic linear polyelectrolyte and its molecular conformation in aqueous solution strongly depends on the concentration, ionic strength and pH.^[46] On addition of 1.0 wt% CMC, CeO₂ becomes negatively charged in the entire experimental pH range. A similar behavior was observed by Shen et al. in alumina suspensions on addition of a cationic polyelectrolyte polydiallyldimethylammonium chloride (PDADMAC). Rapid adsorption of large number of negatively charged CMC molecules onto the positively charged nanoparticles causes charge neutralization and a relatively strong charge inversion (zeta potential -8.5 mV at a pH of 2.9). At pH values above the pKa of CMC (pH 3.65)^[47] the dissociation of CMC molecules increases and the molecular chains possess partially expanded structure with strong electrostatic repulsion between the neighbouring CMC chains.^[46, 48] Hence at pH values above 4, the

adsorption of CMC molecules on to the NPs increases thereby stabilizing the ceria NPs in the slurry as evidenced by zeta potential in the range of $-(40-60)$ mV.

The *Ra* value of the glass surface was found to be 1, 3 and 0.3 nm after polishing using slurry of pH 4, 6.1 and 10 respectively. The hydrolysis of $-\text{Si-O-Si}-$ links in glass is both hydroxyl and hydronium ion catalysed, which is a major step involved in glass polishing as mentioned earlier.^[49] Hence the slurry pH of 4 and 10 facilitate glass polishing and bolster performance. At pH 10, far away from the IEP of ceria (6.7), CeO_2 abrasive slurry possess superior dispersion stability as evidenced by a zeta potential value of $\sim 50 \pm 5$ mV which enables fine polishing of the glass substrate resulting in an *Ra* value less than 1 nm. Further, the acceleration of chemical etching at pH 10 in alkaline solution improves the surface quality of glass to 3 \AA .^[10] These results demonstrate that the electrostatic repulsion among the particles responsible for superior dispersion is one of essential parameters for polishing slurry.

2.5 Conclusions

Spherical, fine cerium oxide NPs have been synthesized by simple ammonia precipitation method. Anisotropic shapes of CeO_2 crystals such as rods and cubes were synthesized by hydrothermal treatment of the hydrated oxide precipitate. Polishing efficiency on glass substrate was evaluated with ceria abrasives of different morphology which showed strong shape and pH dependency. Surface roughness analysis by AFM reveals that the ceria sample with mixed morphology of rods and cubes could produce a surface finish ~ 0.3 nm in alkaline medium. Thus, in the present study, a precise control over glass polishing was achieved by tailoring the amount of Ce^{3+} in the sample which in turn was realized through control over abrasive morphology using simple synthetic

protocols. Predominance of Ce^{3+} and dipolar (200) surface was found to strongly influence hydrophilicity of the nonabrasive which further influence nanolevel polishing. This work has indicated promising polishing efficiency with nano CeO_2 slurry in achieving nanolevel planarity on glass substrates desirable for the global planarization of complex device topography. Probably there is plenty of scope for further research in this line with the size of CeO_2 crystals, thermal treatment, substrates and chemistry of the carrier solvent to tailor and improve CMP performance and selectivity.

2.6 References

- [1] L. M. Cook, *J. Non-Cryst. Solids* **1990**, *120*, 152.
- [2] N. P. Mellott, S. L. Brantley, J. P. Hamilton, C. G. Pantano, *Surf. Interface Anal.* **2001**, *31*, 362.
- [3] L. Y. Wang, K. L. Zhang, Z. T. Song, S. L. Feng, *Appl. Surf. Sci.* **2007**, *253*, 4951.
- [4] D. Bouzid, N. Belkhie, T. Aliouane, *Iop, Materiaux 2010, Mater. Sci. Eng.* **2012**, *28*.
- [5] T. Yu, Y. Park, M. C. Kang, J. Joo, J. K. Park, H. Y. Won, J. J. Kim, T. Hyeon, *Eur. J. Inorg. Chem.* **2008**, 855.
- [6] J. Y. Kim, S. K. Kim, U. Paik, T. Katoh, J. G. Park, *J. Korean Phys. Soc.* **2002**, *41*, 413.
- [7] D. Cornish, L. Watt, *Br. Sci. Instr. Res. Assoc. Rep.* **1963**, R295
- [8] W. Silvernail and N. Goetzinger, *Glass Ind.* **1971**, *52*, 130.
- [9] Q. Luo, D. R. Campbell, S. V. Babu, *Langmuir* **1996**, *12*, 3563.
- [10] Y. G. Wang, L. C. Zhang, A. Biddut, *Wear* **2011**, *270*, 312.
- [11] P. R. V. Dandu, S. Peddeti, S. V. Babu, *J. Electrochem. Soc.* **2009**, *156*, H936.
- [12] N. B. Kirk, J. V. Wood, *J. Mater. Sci.* **1995**, *30*, 2171.
- [13] T. Suratwala, M. Feit, W. Steele, L. Wong, N. Shen, R. Dylla-Spears, R. Desjardin, D. Mason, P. Geraghty, P. Miller, S. Baxamusa, *J. Am. Ceram. Soc.* **2014**, *97*, 81.
- [14] D. Ng, M. Kulkarni, J. Johnson, A. Zinovev, D. Yang, H. Liang, *Wear* **2007**, *263*, 1477.
- [15] A. Jindal, S. Hegde, S. V. Babu, *J. Electrochem. Soc.* **2003**, *150*, G314.
- [16] L. Holland, *Chapman and Hall, London* **1964**.

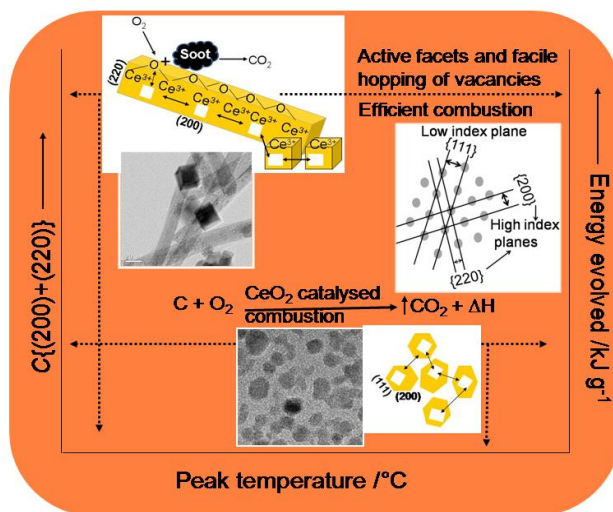
- [17] N. Brown, *Document MISC4476, Lawrence Livermore National Laboratory, Livermore* **1987**, 4.
- [18] C. H. Zhou, L. Shan, J. R. Hight, S. Danyluk, S. H. Ng, A. J. Paszkowski, *Tribol. T.* **2002**, 45, 232.
- [19] R. Jairath, M. Desai, M. Stell, R. Tolles, In *Advanced Metallization for Devices and Circuits - Science, Technology and Manufacturability, Vol. 337* (Eds.: S. P. Murarka, A. Katz, K. N. Tu, K. Maex), **1994**, pp. 121.
- [20] Y. S. Xie, B. Bhushan, *Wear* **1996**, 200, 281.
- [21] M. Biemann, U. Mahajan, R. K. Singh, *Electrochem. Solid St.* **1999**, 2, 401.
- [22] X. D. Zhou, W. Huebner, H. U. Anderson, *Chem. Mater.* **2003**, 15, 378.
- [23] S. Ghosh, D. Divya, K. C. Remani, T. S. Sreeremya, *J. Nanopart. Res.* **2010**, 12, 1905.
- [24] L. V. Zogheib, A. D. Bona, E. T. Kimpara, J. F. McCabe, *Braz. Dent. J.* **2011**, 22, 45.
- [25] F. Zhang, S. P. Yang, H. M. Chen, X. B. Yu, *Ceram. Int.* **2004**, 30, 997.
- [26] H. X. Mai, L. D. Sun, Y. W. Zhang, R. Si, W. Feng, H. P. Zhang, H. C. Liu, C. H. Yan, *J. Phys. Chem. B* **2005**, 109, 24380.
- [27] T. S. Sreeremya, A. Krishnan, S. J. Iyengar, S. Ghosh, *Ceram. Int.* **2012**, 38, 3023.
- [28] P. Dutta, S. Pal, M. S. Seehra, Y. Shi, E. M. Eyring, R. D. Ernst, *Chem. Mater.* **2006**, 18, 5144.
- [29] P. L. Kuo, C. L. Liao, S. K. Ghosh, *Colloid Polym. Sci.* **2001**, 279, 1212.
- [30] G. B. Basim, B. M. Moudgil, *J. Colloid Interface Sci.* **2002**, 256, 137.
- [31] D. Quere, *Physica A* **2002**, 313, 32.
- [32] P. Bharali, P. Saikia, B. M. Reddy, *Catal. Sci. Technol.* **2012**, 2, 931.
- [33] X. Liu, K. Zhou, L. Wang, B. Wang, Y. Li, *J. Am. Ceram. Soc.* **2009**, 131, 3140.

- [34] Y. Lee, G. He, A. J. Akey, R. Si, M. Flytzani-Stephanopoulos, I. P. Herman, *J. Am. Chem. Soc.* **2011**, *133*, 12952.
- [35] A. Krishnan, T. S. Sreeremya, E. Murray, S. Ghosh, , *J. Colloid Interface Sci.* **2013**, *389*, 16.
- [36] Z. Wu, M. Li, J. Howe, H. M. Meyer, S. H. Overbury, *Langmuir* **2010**, *26*, 16595.
- [37] N. Brown, L. Cook, *Paper TuB-A4, Tech. Digest, Topical Meeting on the Science of Polishing, Optical Society of America* **1984**.
- [38] P. R. V. Dandu, S. V. Babu, *Imaging and Applied Optics Technical Digest* **2012**.
- [39] R. Sabia, Stevens, H. J., *The Glass Researcher* **1999**, *9*, 16.
- [40] J. Bentley, S. R. Gilliss, C. B. Carter, J. F. Al-Sharab, F. Cosandey, I. M. Anderson, P. J. Kotula, in *EMAG-NANO 2005: Imaging, Analysis and Fabrication on the Nanoscale, Vol. 26* (Eds.: P. D. Brown, R. Baker, B. Hamilton), **2006**, pp. 69.
- [41] L. Martinez, E. Roman, J. L. de Segovia, S. Poupard, J. Creus, F. Pedraza, *Appl. Surf. Sci.* **2011**, *257*, 6202.
- [42] S. Agarwal, L. Lefferts, B. L. Mojet, D. A. J. M. Ligthart, E. J. M. Hensen, D. R. G. Mitchell, W. J. Erasmus, B. G. Anderson, E. J. Olivier, J. H. Neethling, A. K. Datye, *Chemsuschem* **2013**, *6*, 1898.
- [43] G. B. Harris, *Philos. Mag.* **1952**, *Series 7*, *43*, 113.
- [44] N. S. Ramgir, I. S. Mulla, K. P. Vijayamohanan, *J. Phys. Chem. B* **2005**, *109*, 12297.
- [45] R. Dylla-Spears, L. Wong, P. E. Miller, M. D. Feit, W. Steele, T. Suratwala, *Colloids Surf. A* **2014**, *447*, 32.
- [46] I. Dogsa, M. Tomsic, J. Orehek, E. Benigar, A. Jamnik, D. Stopar, *Carbohydr. Polym.* **2014**, *111*, 492.
- [47] K. W. King, R. M. Smibert, *Appl. Microbial.* **1963**, *11*, 315.
- [48] U. Kastner, H. Hoffmann, R. Donges, J. Hilbig, *Colloids Surf. A* **1997**, *123*, 307.
- [49] C. J. Brinker, *J. Non-Cryst. Solids* **1988**, *100*, 31.

Morphology dependant catalytic activity of cerium oxide nanoparticles in high temperature oxidation

3.1 Abstract

The catalytic performance of a range of nanocrystalline CeO₂ samples synthesised using methods which we demonstrate produce different morphologies is presented in this chapter. It is found that the activity is not correlated with the specific surface area of the powders. The powders were therefore characterized in detail by microscopic (HR-TEM) and crystallographic (XRD) methods which demonstrate that activity is determined by the fraction of the active planes. Different synthetic methods produce CeO₂ nanostructures with preferentially grown active planes which can effectively used as potential catalyst and as oxygen storage material. Crystals with higher {100} facets (a mixed morphology of rods and cubes in the present study) show enhanced catalytic activity. The activity was related to the energetics of the reaction on the exposed crystal facets.



The study provides a step towards quantitative evaluation of the relative contribution from the different facets. This method provides a facile protocol to fabricate CeO₂ nanostructures with preferentially grown active planes, which has great potential in catalytic applications.

3.2 Introduction

Rapid advancements in nanoscience and technology have enabled the fabrication of catalyst particles with tunable shapes in the nanometre scale. Various synthetic strategies have been used to synthesise metal and oxide NPs of desired shapes and even multidimensional structures, and many have the potential to meet the specific requirements for catalysis in terms of activity and selectivity. Heterogeneous catalysis has long been a topic of substantial interest for fundamental studies of chemistry and for practical applications in chemical industries; more than 90% of chemical manufacturing processes use catalysts.^[1] Heterogeneous catalysis is also a major technology for the energy and environmental fields, involving the production of fuels/chemicals and in the clean-up of hazardous or polluting wastes.

Nanoscale cerium oxide crystals with the face-centered cubic fluorite-type $Fm\bar{3}m$ crystal structure^[2-4] have many properties which make them attractive materials for real applications, these include direct electrochemical oxidation of methane in solid oxide fuel cells,^[5, 6] in oxidation catalysis^[7, 8] and as automobile exhaust catalysts.^[9] This interest arises due to the redox activity of the cerium ions,^[10, 11] and because the physical and chemical properties can be tailored through doping or by varying grain size and shape.^[12] Specifically, in catalytic applications of CeO₂, the crystallite size, the number of oxygen vacancies present and the resulting lattice strain are critical to the materials performance.^[13, 14] The interesting chemistry in heterogeneous catalysis using ceria involves reactions taking place at the ceria surface. It has also been reported that despite the low specific surface area, tailored morphologies can perform as smart catalyst in

solid-solid catalysis.^[15] The shape of CeO₂ nanocrystals is correlated with the predominance of particular crystal facets which exhibit different reactivities in various catalytic processes.^[16, 17] For instance, sulphur recovery from SO₂ rich gas can be accomplished on the CeO₂ (111) surface but not on the CeO₂ (110) surface.^[18] Hence methods that give control over crystal shape may provide a means to understand and optimise the catalytic activity.

Anisotropic CeO₂ nanocrystals with rod^[11, 19] and cube^[11] shapes exhibit higher CO conversion at lower temperature^[19] and display higher oxygen storage capacity^[11] than spheroidal particles, due to the presence of a greater proportion of {100} and {110} surfaces. Huang et al. observed strong morphology effects of the CeO₂ support in the preparation, metal–support interaction, and catalytic performance of the Pt/CeO₂ catalysts and correlated with the exposed crystal planes.^[17] Similarly, it was recently reported that for doped-CeO₂ nanocrystals both H₂ selectivity and ethanol-reforming activity decrease in the order rod > tube > cube, as compared to irregular NPs with evenly distributed facets.^[20] This was attributed to the combined effect of high surface area and exposed facets of {100}/{110} planes. On the other hand, Guan et al. reported conflicting observations that spherical particles, with relatively higher surface area, are more active in CO conversion than the rod and prism shaped CeO₂ crystals.^[21] The apparent contradiction in these observations prompted the need for assessment of catalytic activity not only in terms of crystal morphology but in terms of the relative preponderance of the crystal facets.

Among the low index facets of ceria, i.e., {111}, {100} and {110}, the {100} facet is energetically unstable; transforming into {111} on heating above 500°C, and is

catalytically more active than the other two planes.^[22] However, the {110} surface has the lowest vacancy formation energy,^[17, 23-25] an observation which was first predicted by Conesa et al. on the basis of calculation.^[26] The effect of the calcining^[27] and deposition temperature^[28] on preferred orientations of the different crystal facets in CeO₂ has been measured in terms of the changes in the texture coefficient and it was shown that temperature determines the kinetics of growth as manifested in the smoothness of the grains, the crystallinity, the occurrence of preferential growth and the morphology. The texture coefficient of CeO₂ (200) reflection had a maximum of 6.7 at 113 W laser power, at 836 K deposition temperature.^[28] Fino et al. have evaluated catalytic activity of ceria by combustion of carbon soot although there was no detailed morphological or crystallographic assessment of the catalytic surfaces.^[29] The consensus across the published literature is that CeO₂ crystals with a predominance {100}/{110} planes over {111} planes are more catalytically active. Morphology dependent catalytic activity of ceria NPs in soot oxidation was recently reported by Miceli et al. and they observed better activity with star shaped ceria crystals of high SSA.^[15] Achieving tailored morphologies with desired exposed crystal facets and oxygen vacancy in ceria via controlled synthesis process is always desired in catalysis.^[30] However, to the best of our knowledge, there is no study correlating the chemical reactivity with the relative content of active crystal facets in CeO₂ crystals of different shapes.

The present chapter encompasses synthesis of cerium oxide nanocrystals of diverse morphology and its subsequent application as a heterogeneous catalyst in particulate matter (soot) combustion. The nanopowders were characterised by X-ray diffraction (XRD), Fourier transform infrared spectroscopy (FT-IR), thermogravimetry,

X-ray photoelectron spectroscopy (XPS), high-resolution transmission electron microscopy (HR-TEM), and Brunauer-Emmett-Teller (BET) surface area analysis. The abundance of exposed crystallographic planes was evaluated using the texture coefficient^[31] for the three low index planes in CeO₂ nanocrystals by performing Harris analysis^[32] on XRD data, with supporting evidence provided by HR-TEM. The effect of size, shape, and BET surface area of fine CeO₂ nanocrystals on catalytic activity has been investigated by diesel soot combustion and temperature-programmed reduction (TPR) with H₂. Catalytic activity of CeO₂ crystals of different shapes and sizes have been explained in terms of texture coefficient of different crystal planes, this places understanding of the activity on a strong physical basis and identifies design goals for future catalyst development.

3.3 Experimental Section

Materials: The starting chemicals employed in the syntheses were Ce(NO₃)₃·6H₂O (>99.9%, Indian Rare Earths Ltd., India) and the precipitants NaOH (analytical grade, Qualigens Fine Chemicals, India), NH₄OH (25%, analytical grade, Qualigens Fine Chemicals, India). All the chemicals were used as received without further purification. All the chemical syntheses and washings were carried out using double distilled water obtained from a quartz glass distillation unit.

3.3.1 Synthesis

Nanosized cerium oxides were synthesised by ammonia precipitation and precipitation using sodium hydroxide followed by hydrothermal treatment.

Ammonia precipitation: Small spherical crystals of cerium oxide were synthesised by ammonia precipitation using 0.05 M aqueous $\text{Ce}(\text{NO}_3)_3 \cdot 6\text{H}_2\text{O}$ (CN) solutions by salt into precipitant (SIP) technique.^[33] The detailed synthetic procedure is provided in section 2.3.1a.

Synthesis of Cerium oxide Nanorods: Cerium oxide nanorods were prepared hydrothermally from a 0.05 M CN precursor solution. The detailed synthetic procedure is given in section 2.3.1b. The sample will henceforth be called as HT1. A fraction of this sample was subsequently calcined at 400 and 1000°C for 4 h, the calcined samples will be referred to as HT1C4 and HT1C1 respectively.

Cerium oxide Nanocubes: Cerium oxide nanocubes were synthesised using 0.05 M aqueous CN solution by autoclaving the freshly precipitated slurry at 180°C, following a modified method described for synthesising CeO_2 nanorods provided in section 2.3.1.b. This product is denoted as HT2.

3.3.2 Catalytic activity tests

The reactivity of cerium oxide NPs in catalysing combustion of carbon was investigated by controlled combustion of a 40 mg mixture of CeO_2 catalyst, carbon soot (collected by burning diesel) and α -alumina using a simultaneous thermal analyser. The rate of heating used in the ramp was $10^\circ\text{C min}^{-1}$ using standard alpha alumina as reference in the temperature range 50°-800°C. The sample for soot oxidation was prepared by mixing carbon, powdered CeO_2 and alumina powder (average particle size ~450 nm (Condea Chemie, Germany) in the weight ratio 1:9:10 in an agate mortar. It was

mixed and ground well. The inert alumina powder was added to prevent the thermal runaways.

The total energy evolved and the peak temperatures of combustion were calculated for different CeO₂ powders from the thermal analysis profiles using the Pyris software of the TGA equipment.

3.3.3 Oxygen Storage Capacity Measurements

A modified thermogravimetric method was employed to determine the OSC by the oxygen release characteristics of the sample in the temperature region 573–1073 K.^[34] The change in the weight of the sample was monitored by thermogravimetry (TG) under cyclic heat treatments in flowing nitrogen or dry air. A thermogravimetric analyser (Perkin Elmer, STA 6000) is employed for this purpose. The heat cycle consisted of heating the sample to 1073 K, cooling to 423 K, and again heating to 1073 K. All heating and cooling rates are maintained at 5 K.min⁻¹. The weight loss of the sample during the second heating cycle is used to measure the oxygen release properties.

3.3.4 Temperature Programmed Reduction using Hydrogen (H₂-TPR)

Temperature programmed reduction experiments were carried out using a 5% H₂-N₂ mixture (40 mL.min⁻¹ flow rate) at a heating rate of 10°C min⁻¹. 0.1 g of catalyst was used. The catalyst was heated at 120°C for 2 h and cooled to room temperature in flowing (40 mL.min⁻¹) helium prior to the TPR experiment.

3.4 Results and discussion

3.4.1 Primary sample characterisation

The recorded XRD patterns for three selected powder samples, synthesised through different techniques, are presented in Fig. 3.1. The XRD profiles for all the

nanopowders match with the face-centred cubic [space group: $Fm\bar{3}m$ (225)] of crystalline CeO_2 (JCPDS Card No. 34-394) with fluorite-type structure in which each metal cation is surrounded by eight oxygen atoms.^[35] The refinement of the lattice constants revealed small deviation in unit cell parameters (lattice constant $a = 0.541$ - 0.545 nm) in CeO_2 of rod/tube shapes as well as ammonia precipitated crystals, indicative of small structural distortion due to crystal defects.^[20] The XRD patterns also reveal that the as-prepared ammonia precipitated and hydrothermally treated powders are crystalline CeO_2 . There is moderate broadening of the diffraction peaks in AP, which suggests smaller crystals in this sample.

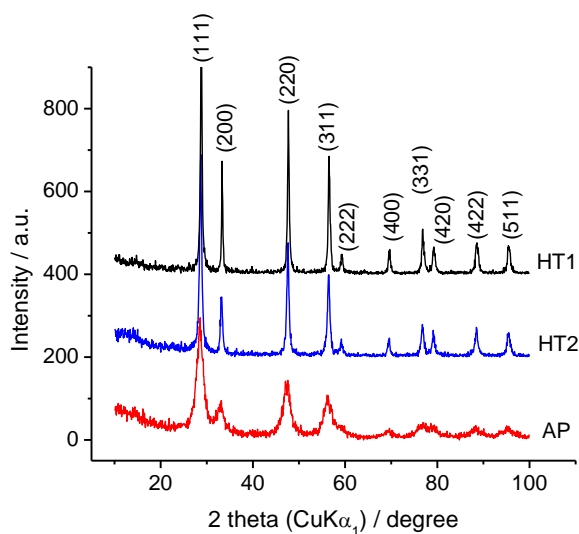


Fig. 3.1 X-ray diffraction patterns of CeO_2 powders AP, HT1 and HT2 synthesised through different routes. The patterns of HT2 and HT1 are scaled to avoid overlapping.

An important factor in developing new nanotechnologies for materials applications is the need to produce nanocomposites. In most preparative schemes good dispersibility, preferably in aqueous suspension is required. For this reason we studied the

colloidal properties of aqueous suspensions of AP and HT1 (as examples of both methods) by photon correlation spectroscopy (PCS) as shown in Fig. 3.2. The average hydrodynamic size, D_{PCS} , for HT1 is 26 nm with a polydispersity index (PDI) of 0.19. For AP, D_{PCS} is 17 nm with a PDI of 0.26. The low PDI values indicate that the suspensions are relatively monodisperse.

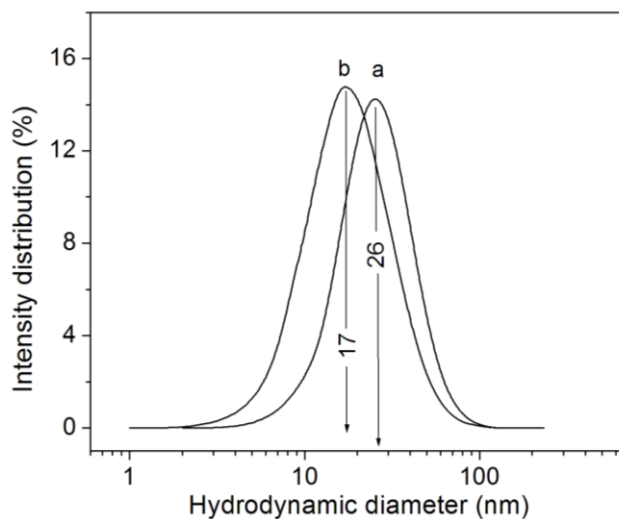


Fig. 3.2 Particle size distribution as measured by PCS for CeO₂ powders (a) HT1 and (b) AP dispersed in water.

At pH ~10, the zeta potential of the suspensions was measured as -30 mV. The suspensions were stable for several days due to electrostatic stabilisation, as one would expect given the strong surface charge.

3.4.2 Detailed X-ray diffraction analysis

The mean crystal diameter and microstrain of the CeO₂ nanocrystals were evaluated by line-profiling of prominent X-ray diffraction peaks. Crystallite size is often determined from XRD profile using the Scherrer equation,^[36, 37] however, this underestimates grain size as it ignores broadening of the diffraction peaks due to

microstrain in the lattice^[13] and so is not appropriate for this study. Following W-H technique the $\beta \cos \theta$ is plotted against $\sin \theta$ for a number of XRD peaks for all the nanocrystalline CeO₂ powders at different 2θ values and are shown in Fig. 3.3. The average crystal size (D_{XRD}) and strain (ϵ) are determined from the intercept and the slope of the linear regression to the data.

The estimated D_{XRD} values are provided in Table 3.1. The strain profile (Fig. 3.3b) shows a non-linear decrease in strain with increase in size. The strain data conform very well to a single power law, even for samples prepared in very different ways. The value for the power, 1.68, is in the range reported by other workers.^[14] The strain values in the range 0.0041-0.0011, obtained for HT1, HT2 and HT1C1 are far smaller than those previously reported for CeO₂ crystals of comparable sizes, which were synthesised by wet chemical methods.^[14, 38]

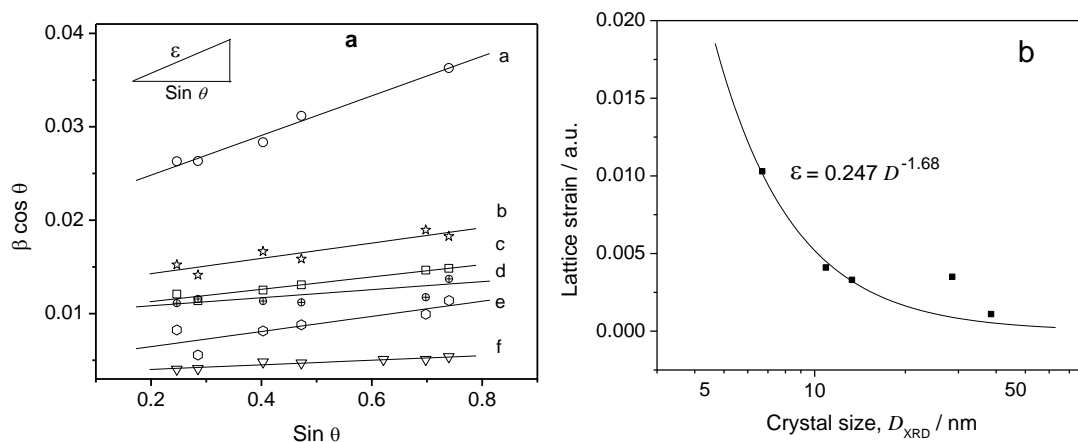


Fig. 3.3 (a) Representative Williamson-Hall plot of $\beta \cos \theta$ versus $\sin \theta$, for the reasonably well-resolved reflections. The solid lines are linear regressions to the data. (b) semilog plot of variation in lattice strain with the size of CeO₂ crystals of different shapes. The solid line is a least square fit of a power law to the data.

Interestingly the lattice strain of 0.0041 in HT1 is further reduced to 0.0011 in HT1C1, on heating at 1000°C. Evidently the extended duration (~24 h) used in the hydrothermal treatment, and subsequent annealings, results in larger crystallites with reduced microstrain.^[39] On the basis of previous experiments these difference might be expected to affect the catalytic activity of the surfaces.^[14]

Texture coefficient by Harris analysis

Harris analysis was also performed on the CeO₂ XRD data.^[32, 40] The preferred orientation of the crystallographic planes was estimated and expressed as the texture coefficient $C(h_i k_i l_i)$, using equation 2.2. A sample with randomly oriented crystallites presents a $C(hkl)$ of 1, while a larger value indicates an abundance of crystallites oriented to that (hkl) plane.^[31]

Table 3.1 Crystal dimensions and texture coefficients of different crystal facets of CeO₂.

Sample	D_{XRD} [nm]	$C[111]$	$C[200]$	$C[220]$	$C[200] +$ $C[220]$
HT1	10.1	0.7972	1.199	1.004	2.203
HT1C4	28.5	0.9401	1.1429	0.9169	2.0598
HT2	13.9	0.9505	1.0721	0.9772	2.0493
AP	6.4	0.9634	1.0638	0.9727	2.0365
CC	13.7	1.0604	0.9526	0.9869	1.9395
HT1C1	39.3	1.1516	0.9802	0.868	1.8482

The texture coefficient data for all the specimens of this study is shown in Fig. 3.4. Preferential orientation of the crystallites along the higher energy planes {100} was

apparent in most cases, but particularly for the hydrothermally synthesised samples. The I_{200}/I_{111} was ~ 2 times higher than that of bulk ceria in HT1 (Fig. 3.1).

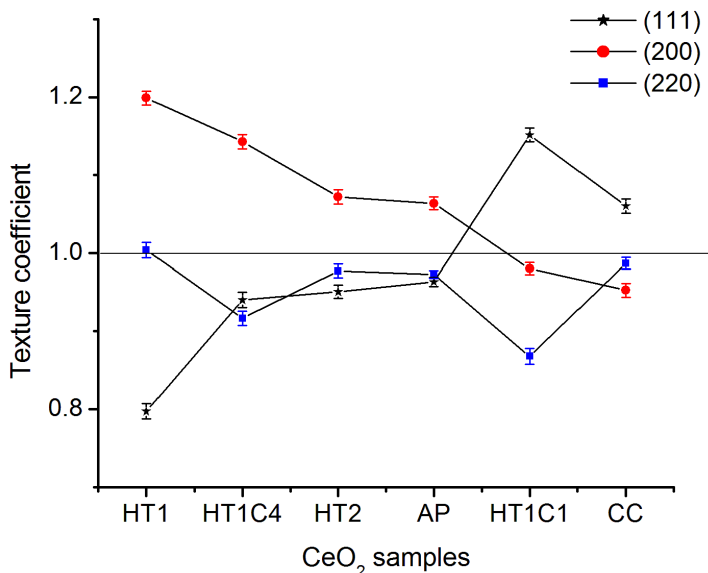


Fig. 3.4 The texture coefficient of CeO₂ nanocrystals of different shapes calculated from their powder X-ray diffraction patterns (reference JCPDS 34-394). The error bars represent the standard deviation estimated on the basis of the three independent measurements.

However, annealing the sample HT1 at 400 and 1000°C (HT1C4 and HT1C1), has resulted in preferential growth of CeO₂ crystals in stable, low energy {111} facets.

3.4.3 Electron microscopy

Detailed morphological and structural analyses of the samples was undertaken using bright field high-resolution TEM, typical results are shown in Fig. 3.5 and 3.6. The ammonia precipitated CeO₂ NPs in AP are found to be almost spherical. The mean particle size (D_{TEM}) in AP is 5.3 nm with standard deviation, $\sigma = 0.99$ nm ($D_{\text{XRD}} = 5.2$ nm) as shown in Fig. 3.5a.

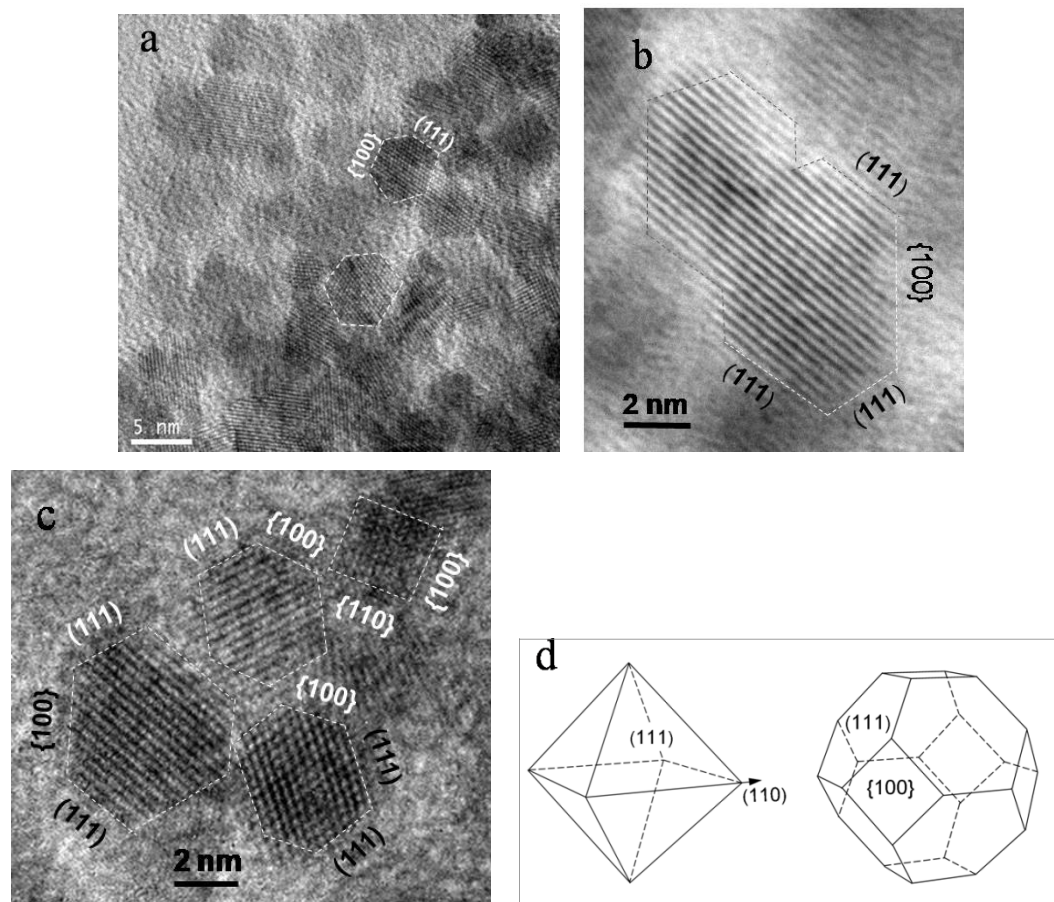
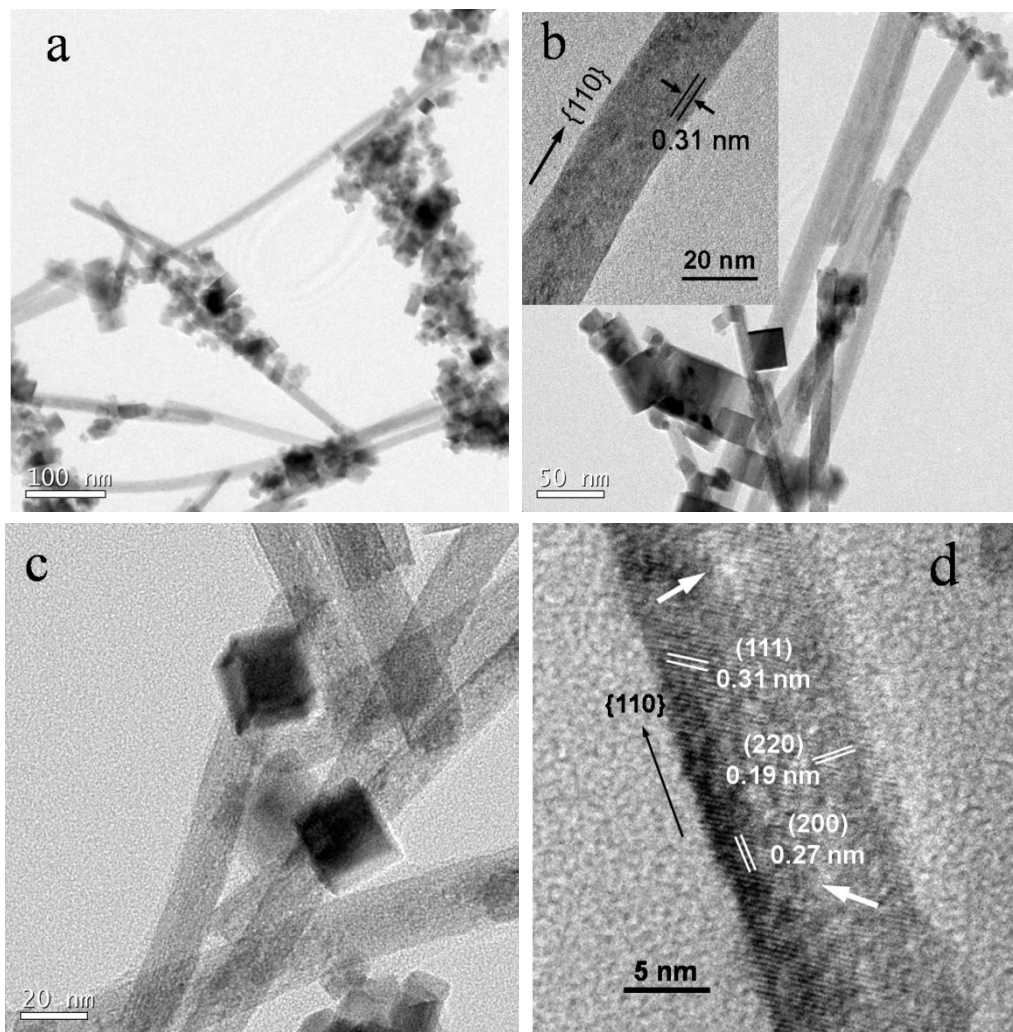


Fig. 3.5 Bright field TEM images of ammonia precipitated CeO₂ particles (a) AP and (b) Typical high-resolution TEM images of CeO₂ NPs displaying a coherent interface in AP, (c) the {100} and {111} facets of cubic CeO₂ (AP), and (d) schematic model showing the formation of a truncated octahedron from an octahedron.

Lattice fringes attributed to (111), (200), and (220) crystal planes with corresponding interplanar spacings of 0.31, 0.27, and 0.19 nm, respectively, which are characteristic of fcc CeO₂ were identified in HR-TEM images of spheroidal crystals in AP (Fig. 3.5a). A careful examination reveals that the particles are dominated by {111} and {200} fringes along the [110] observation establishing that the shape of the ceria nanocrystals is the truncated octahedron (polyhedra) enclosed by eight {111} and six {200} planes (Fig. 3.3d), as already reported.^[41] Crystal planes of similar type tend to

align with each other to minimise the interface strain,^[42] forming a coherent interface (Fig. 3.5b). High-resolution TEM micrographs of CeO₂ samples synthesised hydrothermally are shown in Fig. 3.6.



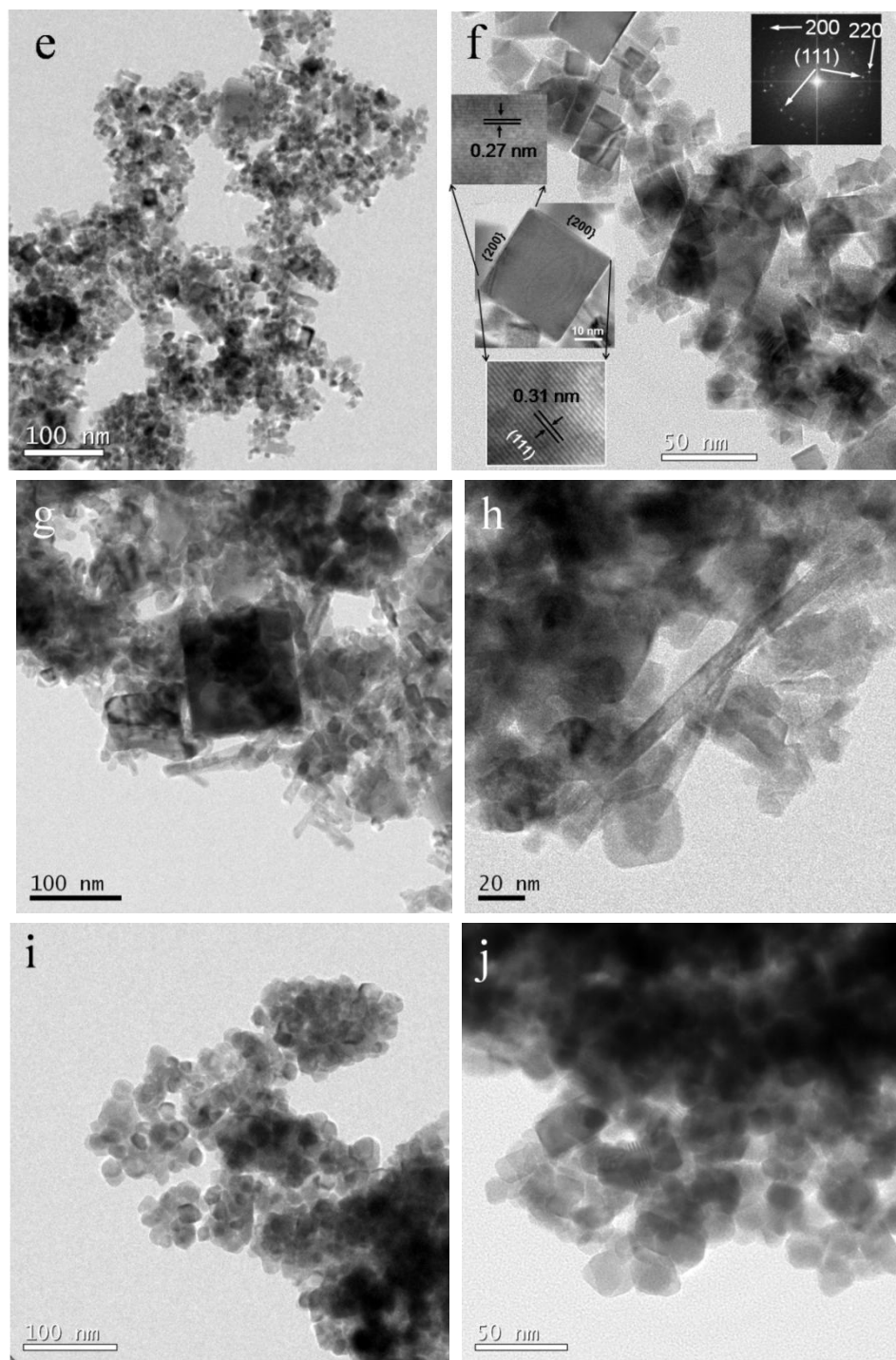


Fig. 3.6 TEM image of hydrothermally synthesised CeO_2 crystals. (a, b, c) HT1 containing nanorods and cubes autoclaved at 120°C . (d) HR-TEM image of a nanorod in HT1. (e, f) HR-TEM image of nanocubes in HT2 autoclaved at 180°C , nanocubes showing (111) and {100} lattice planes are shown in the inset. FFT analysis is also shown as the inset to (f). (g, h) HT1C1 (i, j) commercial ceria.

Mild hydrothermal treatment at 120°C with a high base concentration (8 M) produced predominantly nanorods (HT1) from anisotropic growth of unstable $\text{Ce}(\text{OH})_3$ nuclei, governed by dissolution recrystallisation mechanism. When the autoclave temperature was increased to 180°C (HT2) nanocubes were formed. The average sizes from TEM (D_{TEM}) for HT2 is 13.5 ± 2.5 nm. The TEM analysis of sample HT1 demonstrates that it consists of a mixture of cubic and rod-shaped crystals of CeO_2 . Detailed analysis of multiple images of HT1 (e.g. Fig. 3.6a) reveals that it contains ~31.5% (number) nanorods with an average length of ~355 nm and diameter ~22 nm, that is, an aspect ratio of ~16. This equates to an average (equivalent sphere) diameter of ~60 nm. The remaining 68.5% are nanocubes with an average edge length of ~18.4 nm. By volume (or mass) the sample is approximately 91% rods and 9% cubes. The square faces of the CeO_2 nanocubes are enclosed by {100} planes. Strong presence of {111} facets is evidenced by FFT analysis, see the inset to Fig. 3.6f. The (111) crystal facets pass diagonally across the surface of the cubes (insets of Fig. 3.6f). 1D growth is seen in the HR-TEM images of nanorods in {110} direction with {111} as well as {100} exposed surfaces. Fast Fourier transform (FFT) analysis of Fig. 3.6d confirm the presence of {111} and {110} facets only. By contrast, Yang et al. reported the growth along the [211] direction.^[43] Point defects due to missing atoms or local deformation due to the twist of parallel planes are observed on the nanorod surfaces in some instances, these are marked by arrowheads in Fig. 3.6d. We expect that such defects boost up the catalytic performance as more surface reconstruction may have occurred in these nanorod surfaces.

3.4.4. XPS and Raman spectral analysis

Due to the lower energy requirement for the interconversion between the two oxidation states (1.72 eV), the Ce^{3+} state exists to some extent, along with the Ce^{4+} in CeO_2 .^[44] For the detailed study of $[\text{Ce}^{3+}]$ /oxygen vacancies in the system, the XPS and Raman spectra of selected samples were analysed. Fig. 3.7 shows the XPS survey and Ce 3d spectra of HT1, HT2, AP.

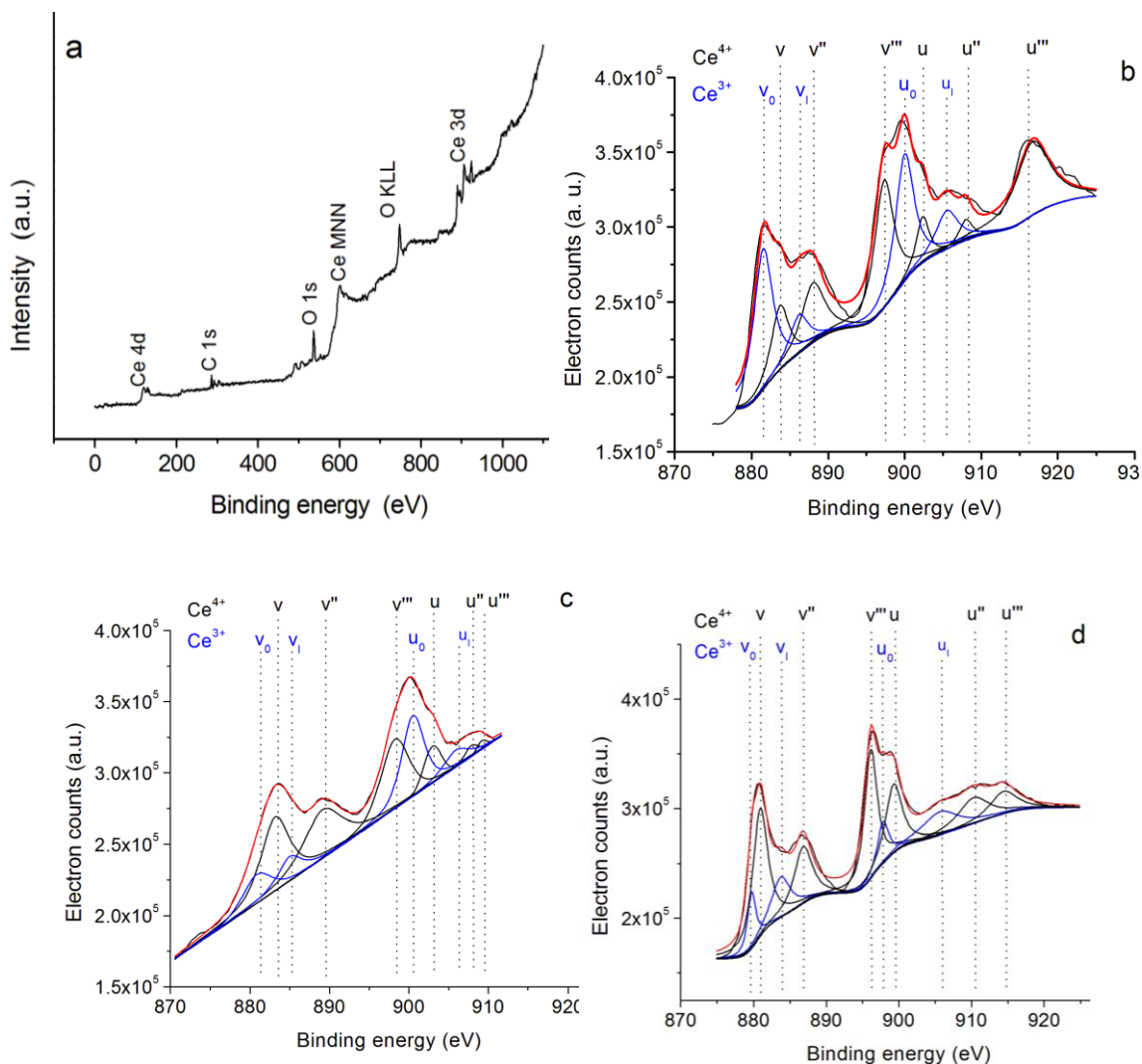


Fig. 3.7 XPS patterns: a) wide spectrum of HT1 and deconvoluted Ce 3d spectra of b) HT1, c) HT2, and d) AP.

The XPS wide spectrum shows the peaks attributed to the core levels of Ce 4d, Ce 3d, O 1s, and C 1s where the Ce 3d electron core level is characterised by 3d_{5/2} and 3d_{3/2} series peaks.^[45] In the Ce 3d spectrum, v_o, v₁, u_o, and u₁ peaks are attributed to Ce³⁺; while v, v'', v''', u, u'' and u''' are the characteristic peaks of Ce⁴⁺ ions. The concentrations of Ce³⁺ in all the samples were estimated using the integrated area of each peak in the spectrum and is given in Table 3.2. The Ce³⁺ content is evaluated as 44.3, 35.5 and 26.2% in HT1, HT2 and AP respectively (Table 3.2).

Table 3.2 Ce³⁺ content from the integrated peak area analyses of XPS spectrum (binding energy states for Ce³⁺ are indicated by subscripted ‘u’ and ‘v’).

Area	v _o	v	v ₁	v''	v'''	u _o	u	u ₁	u''	u'''	Ce ³⁺ (%)
HT1	414551.6	171243.5	113523.2	213745.2	376724.5	359494.0	90732.91	131589.7	41154.68	387503.4	44.3
HT2	108324.1	303712.8	87602.8	264997.3	248741.3	244545.7	72051.84	62091.56	15767.84	15767.84	35.5
AP	106075.9	431106.100	170481.50	227699.7	363766.9	103940.2	253428.3	181971.5	173765.3	133598.8	26.2

The Ce 3d spectrum of commercial ceria was not resolvable as it contains dopant cations as impurity (Fig. 2.9D). The Ce³⁺ concentration in HT1 (rod-cube) is almost twice the same contained in AP (spheres) and is slightly higher than that reported for 2 nm CeO₂ nanodots in our earlier work^[45] substantiating the size and shape dependence of Ce³⁺ content. It is well-known that the presence of Ce³⁺ in the fluorite lattice, generates oxygen vacancies to maintain charge balance.^[34, 46] The presence of surface oxygen vacancies in the materials was monitored by UV-Raman spectroscopy (Fig. 3.8) which shows the presence of peaks at 460 (peak γ), 560 (α) and 600 cm⁻¹ (β) respectively. A small peak characteristic of O₂ ^{δ -} (0 < δ < 1) species was observed at ~1340 cm⁻¹ in all the samples.

The main peak at ca. 460 cm^{-1} is due to the F_{2g} mode vibration of cubic fluorite structure in CeO_2 .^[47] The phonon modes at 560 and 600 cm^{-1} are characteristic of oxygen vacancies in ceria system.^[34, 45, 47]

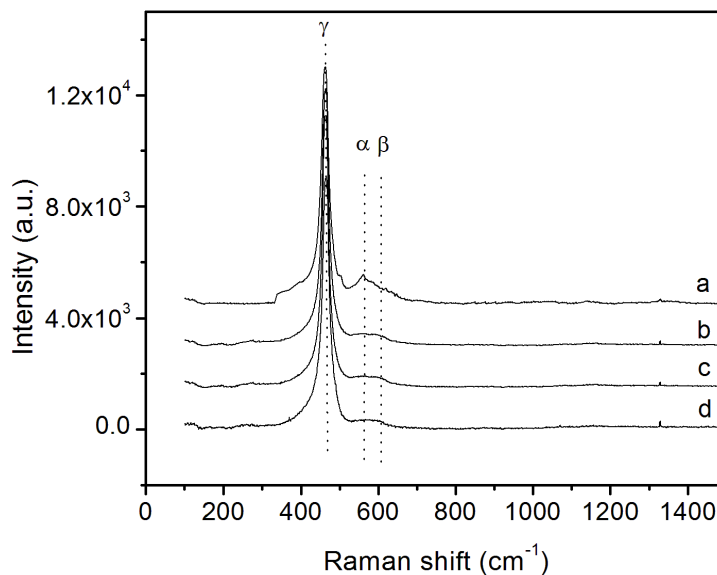


Fig. 3.8 Raman spectra of HT1 (a), HT2 (b), AP (c) and CC (d) at 633 nm excitation taken at room temperature.

Following the observation made by Wu et al.,^[48] the relative density of defect sites ($\sim 560\text{ cm}^{-1}$) in nanoparticulate CeO_2 varies as HT1 (rod-cube) $>$ HT2 (nanocubes) \geq AP (nanospheres). CeO_2 possess a high oxygen storage capacity (OSC) because of the rapid formation and elimination of oxygen vacancy defects in it. The higher Ce^{3+} concentration ensuing in defects and exposure of more reactive $\{100\}$ surfaces, followed by $\{110\}$ surfaces, can facilitate the formation of oxygen vacancies in them,^[11] and introduce enhanced oxygen storage capacity in the material as shown in Table 3.3.

Table 3.3 Oxygen storage capacity from TGA and $[\text{Ce}^{3+}]$ from deconvoluted Ce 3d XPS spectra.

Sample	Wt loss (%)	Oxygen vacancy content (δ)	Total OSC ($\mu\text{mol O g}^{-1}$)	Ce^{3+} (%)
HT1	1.346	0.431	420.6	44.3
HT2	0.76	0.243	280.9	35.4
AP	0.8988	0.287	237.5	26.2
CC	0.3147	0.1	98.3	Nd ^{c)}

^{c)} Not determined. $[\text{Ce}^{3+}]$ could not be calculated as the Ce 3d spectrum of commercial ceria is not well resolved (see Fig. 2.9D).

The OSC as determined by thermogravimetry^[34] (shown in Table 3.3) follow an order HT1 > HT2 > AP > CC. The highest value obtained was 420.6 $\mu\text{moles O}_2 \text{g}^{-1}$ for HT1 (Rod-Cube), which possess paramount concentration of Ce^{3+} (44.3%), and reactive polar {100} surface. Mai et al. reported an OSC value of 554 and 353 $\mu\text{moles O}_2 \text{g}^{-1}$ for pure ceria nanorods and nanocubes respectively.^[11]

3.4.5 Overview of physical properties

Selected data from the range of characterization techniques are presented in Table 3.4. It is clear that both the D_{XRD} and D_{BET} values (which are statistical averages of the entire sample) are in excellent numerical agreement with D_{TEM} (which is evaluated from a limited number of micrographs) for samples AP, and HT2. This validates our choice of the W-H procedure for measuring D_{XRD} and strengthens the validity of the strain values obtained. It also confirms that particles in samples AP, and HT2 are single crystals, as is suggested by the observation of sharp parallel crystal facets in the HR-TEM micrographs. It is generally found that the macroscopic surface area of the samples shows the expected

correlation with NP size, the hydrothermally synthesised samples having specific surface areas almost an order of magnitude lower than those produced by co-precipitation. For sample HT1, widely differing average size and crystal diameter ($D_{\text{TEM}} \sim 60$ nm and $D_{\text{XRD}} = 10.1$ nm) are observed as this sample is composed of a mixture of nanocubes and nanorods. It is very interesting that, despite this difference, the dependence of crystal strain on D_{XRD} for this sample (Fig. 3.3b) perfectly matches the behaviour of the single-crystalline powders.

Table 3.4 Primary physical characterisation of the CeO₂ nanocrystal samples.

Sample name ^{a)}	Morphology	D_{XRD} (nm)	D_{TEM} (nm)	D_{BET} (nm)	SSA (m ² .g ⁻¹)	Lattice parameter (nm)
AP	Spheres	6.4	6	5.8	143	0.544
HT1	Cubes and rods	10.1	60 ^{b)}	12.5	66	0.542
HT2	Cubes	13.9	13.5	19.7	42	0.542
HT1C4	Large cubes and rods	28.5	nd	36.9	22.4	0.541
CC	Spheres and cubes	13.7	20	165	5	0.543
HT1C1	Large cubes and rods	39.3	-	Nd ^{c)}	<1	0.541

^{a)} AP-Ammonia precipitated spherical ceria NPs, HT1 and HT2 are hydrothermally synthesized ceria at 120 and 180°C, CC is commercial ceria. HT1C4 and HT1C1 are HT1 calcined at 400 and 1000°C.

^{b)} Equivalent sphere diameter (see text)

^{c)} The BET equivalent size could not be measured for this sample, given the low SSA.

The hydrodynamic diameter, D_{PCS} , for AP was 17 nm (PDI 0.26), indicating the presence of small clusters of crystals.^[49] However, in the case of HT1, D_{PCS} was only 26

nm (PDI 0.19). This demonstrates that the larger nanorods are not dispersible and the suspension produced from HT1 is composed of dispersed nanocubes, of edge length, from TEM, ~18.4 nm. Given that the D_{PCS} value is the average based on the light scattering intensity, which is proportional to the sixth power of particle size. At the detection angle used in this study, 90° , the experiment is particularly sensitive to the presence of any aggregates. Hence for this suspension the number of clusters of nanocubes, if any, must be very small. This approach based on preferential precipitation is currently under investigation in our laboratory with a view to isolate the isotropic and anisotropic fractions as pure materials.

So in summary, co-precipitation produces samples composed of single spherical crystals of CeO_2 , of size < 7 nm, with a slight preponderance of high energy $\{100\}$ facets. The hydrothermal approach produces materials composed of nanocubes or mixtures of rods and cubes. The crystals in the hydrothermally produced samples have a greater preponderance of high energy $\{100\}$ facets than in the powders prepared by co-precipitation. Thermal treatment of the samples produced by the hydrothermal approach results in a significant increase in crystal size and these are now dominated by less active $\{111\}$ facets.

3.4.6 Catalytic activity evaluation

3.4.6.1 Diesel soot oxidation

The catalytic activity of the CeO_2 powders was evaluated by measuring the peak combustion temperature (T_p) and the total heat evolved (ΔH) during the CeO_2 catalysed combustion of carbonaceous materials (diesel soot). The ΔH values are calculated from the area of peak in DTA using the Pyris software. The carbonaceous soot was

characterised by TGA which revealed a total combustibles content of 92.50 wt% and the presence of 6.75 wt% moisture. Hence remaining 0.75% is neither volatile nor combustible.

TGA profiles of soot with and without various nanocatalysts and variation of energy evolved and peak temperature estimated from DTA profiles against $[C(200)+ C(220)]$ are given in Fig. 3.9 which shows that catalytic activity in terms of the total heat evolved from the soot combustion varies from a minimum of 4 kJ.g^{-1} , for HT1C1, to a maximum of 13.0 kJ.g^{-1} , for HT1.

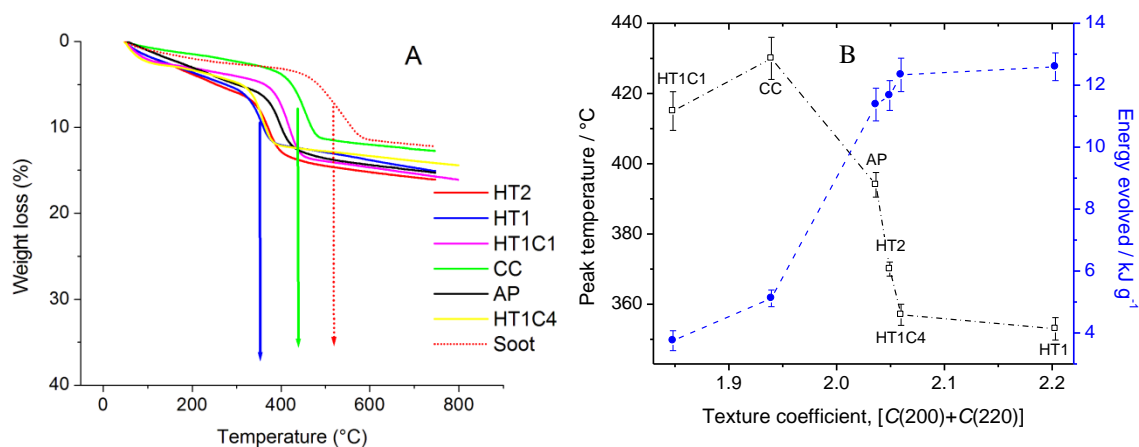


Fig. 3.9 A) TGA profiles of soot with and without various nanocatalysts. B) Variation of (a) energy evolved and (b) peak temperature against $[C(200)+ C(220)]$ which shows the catalytic activity of ceria nanoparticles.

These values are in the expected range; 15 kJ.g^{-1} has been reported for coal.^[29] The same samples define the range of peak combustion temperatures (T_P) in this study, which were generally inversely correlated with the total heat evolved; the extreme values were 430 and 353°C for CC and HT1, respectively. The T_P value for uncatalysed soot oxidation was 518°C and hence HT1 could reduce the soot oxidation temperature by $\sim 165^\circ\text{C}$.

We noted above (Fig. 3.4.) that the texture coefficients vary from sample to sample. We now note (Table 3.1) that the sum of texture coefficients for the facets (200) and (220) [$C(200) + C(220)$] increases in the order $HT1 > HT1C4 > HT2 > AP > HT1C1 > CC$, which are considered to be more active, is a minimum (1.85) in HT1C1 and maximum (2.20) in HT1. The soot combustion temperature of various nanocatalysts decreases in the order $CC > HT1C1 > AP > HT2 > HT1C4 > HT1$. It should be noted that the catalytic activity measurements were performed in triplicate and for each sample at least two independent preparations were completed. The error bars represent the standard deviation estimated on the basis of the three measurements. The measurements show significant variation in activity from sample to sample that is not correlated with the specific surface area of the powders (Table 3.4). The SSA of the highly active HT1 was in the range reported by other authors.^[11, 24, 46] It is also interesting to note that the reduction in T_p (~32%) was better than that reported by Fino et al. (30%) for self assembled ceria stars with a high SSA of $105 \text{ m}^2 \cdot \text{g}^{-1}$.^[15] Despite the very low SSA ($< 1 \text{ m}^2 \cdot \text{g}^{-1}$), HT1C1 shows ~20% reduction in T_p . We can conclude that, under the conditions of the study, activity was not limited by the available surface but by the energetics of the reaction on the exposed crystal facets in all cases.

Considering the energy evolved during soot oxidation, we find that except for CC, the trend in ΔH is not associated with formation method, surface area, or crystal size, but once again with the sum of the texture coefficients of the active planes $C(200)$ and $C(220)$. We tentatively attribute the deviation of T_p in CC to factors related to the presence of dopant metal ions. This reaffirms that the exposed $\{100\}$ and $\{110\}$ facets exhibit greater catalytic activity as compared to $\{111\}$ facets.^[20] As expected the peak

combustion temperature, T_p , is found to broadly follow the opposite trend; more efficient catalysis is associated with a higher energy generation at lower temperature. Comparing the hydrothermal to the co-precipitation approaches; we find that in general for the HT series greater $C(200)$ values and lower $C(220)$ are observed. However, the trend in activity is only apparent when the sum of the texture coefficients is examined. So once again, the soot combustion study reaffirms our findings from the OSC measurements. This suggests that the activity is shared across these crystal facets irrespective of the method of synthesis, crystal size or morphology. On calcining HT1 at 1000°C to produce HT1C1, we observe only a trivial reduction in catalytic activity due to crystal growth ($D_{\text{XRD}} \sim 39$ nm) preferentially in the least active (111) plane, as indicated by a decrease in $C(200)$ and an increase in $C(111)$. It is interesting and assuring to note that HT1 retained its morphology (see Fig. 3.6g) and catalytic activity in soot oxidation even after calcination at 400°C (HT1C4) and the one heat treated at 1000°C (HT1C1, ageing period 4 h) was far better than commercial ceria powder as evidenced by the soot combustion temperature of 357 and 415°C in these samples respectively with respect to the same at 430°C with CC.

Sample HT1 is unusual in that it contains a mixture of nanorods and nanocubes, the latter comprising ~9% of the sample by mass. The fraction of the total surface area corresponding to the cubes is therefore <1% and they are predominantly bound with {100} facets. The sample activity therefore arises almost exclusively due to the nanorods and the ΔH value for HT1 follows the trend of the other samples. The T_p value for HT1 is, however, lower than for the other samples. This suggests different reaction kinetics for the exposed {100} and {110} facets that dominate the surfaces of the rods, which are far

more extended in this case. The nanorods with more exposed {100} crystallographic facets are expected to have more of oxygen terminated facets. Oxygen terminated facets would theoretically require less amount of activation energy to donate oxygen as compared to cerium terminated facets. Once again there is no strict correlation between the specific surface area and the peak temperature indicating that the energetic on the surface are the defining influence in the combustion behaviour.

Mechanism of soot oxidation/Catalytic pathway for soot oxidation

A catalytic pathway (Fig. 3.10) similar to the one reported by Li et al. for CO oxidation is proposed for soot oxidation on the defective ceria NRs. This pathway involves alternative reduction and oxidation of the ceria surface with formation of oxygen vacancies and their successive replenishment by gas-phase oxygen.^[46]

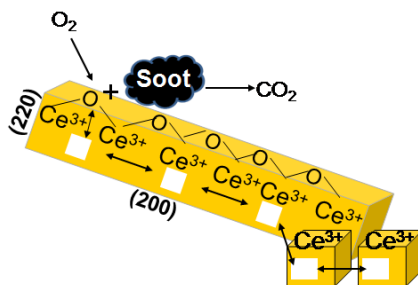


Fig. 3.10 Catalytic pathway for soot oxidation over HT1 with mixed morphology of rods and cubes enriched with linear oxygen vacancy clusters which offers a facile hopping pathway for vacancies.

Balducci et al. have shown in a computer simulation study that migration of oxygen takes place via a vacancy hopping mechanism and it is assumed that an oxide ion migrates to a nearest-neighbour vacant site along a linear path.^[50] Hence in the case of HT1 catalyst with 44.3% Ce^{3+} , the presence of oxygen vacancy clusters facilitates the activation and

transportation of active oxygen species via a vacancy hopping mechanism as shown in Fig. 3.10.

3.4.6.2 From H_2 -TPR profiles of ceria nanocatalysts

H_2 -TPR profiles of selected catalysts compiled in Fig. 3.11 provide further information on enhanced catalytic activity of our samples compared to that of commercial ceria.

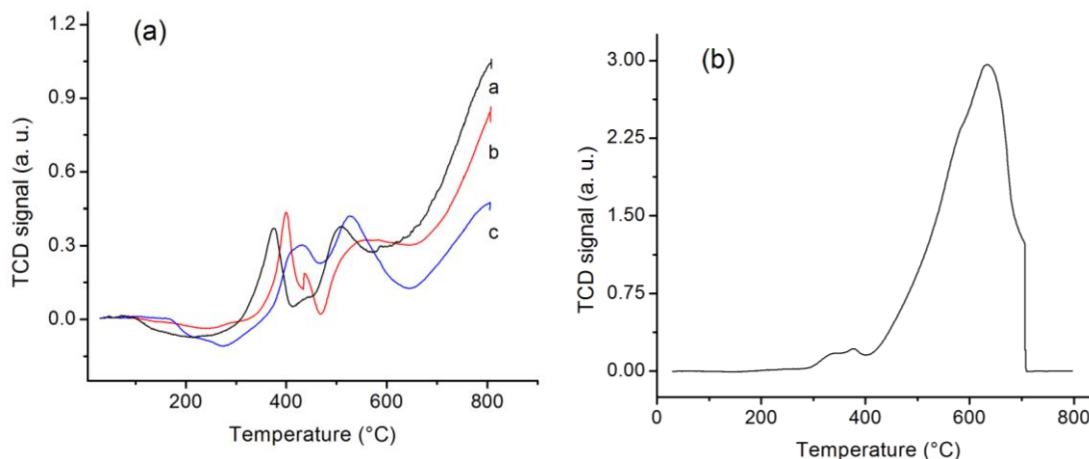


Fig. 3.11 H_2 -TPR profile of a) HT1 b), HT2 and c) AP in (a) and (b) commercial CeO_2 .

The reduction profiles show two broad maxima and a further reduction maximum near or above $700^\circ C$ (the maximum operating temperature possible was $800^\circ C$ in the TPR instrument); the former features below $650^\circ C$ are attributed to a global process corresponding to the consumption of surface oxygen species, whereas the maximum at about $800^\circ C$ reflects the bulk reduction. However, in the commercial CeO_2 profile in Fig. 3.12b only the bulk peak was predominantly observed, which is reasonable taking into account that the BET surface area of this sample is very low ($5\text{ m}^2\cdot\text{g}^{-1}$). However, bulk oxygen requires to be transported to the surface before their reduction and consequently, the bulk reduction takes place at higher temperature compared to the surface reduction.^[51]

In HT1, HT2 and AP the reduction peaks located between 280–500°C are substantially higher than that in the case of commercial ceria powders, which means that all the ceria nanocatalysts possess stronger surface activity than that of the commercial ceria particles. In view of the normal diesel exhaust temperature in the range of 200–400°C, the oxygen release capacity of each catalyst in this temperature range is an important factor affecting soot combustion performance.^[29, 52] During the soot oxidation with O₂, the function of the catalyst is to increase the ‘active oxygen’ transfer to the soot surface.^[53] Clusters of more than two vacancies, such as linear surface oxygen vacancies as present in the mixed morphology catalyst, proved to be favourable for migration of oxygen.^[46] An increase in surface oxygen vacancy (as evidenced by XPS and Raman) will in turn increase surface oxygen mobility. It is interesting to note that in the TPR profile of our nanocatalysts, the peak characteristic of surface oxygen species appeared at 373, 399.8, 430.9°C in HT1, HT2 and AP respectively.

In particular, the first sharp reduction peak shows a high migration rate of surface oxygen due to facile hopping of vacancies in a linear way, which leads to a much lower soot combustion temperature (T_P) of 353°C in HT1. The T_P value increases to 430°C in the case of commercial ceria because of the large amount of lattice oxygen released at high temperature by this catalyst. Though the nature of the reductants in the H₂-TPR and the soot oxidation (carbon) is different, the trends in the catalyst surface reduction temperature in the H₂-TPR and the peak temperature, T_P from thermogravimetric profiles in soot oxidation are very well coincided, which suggests the involvement of the active crystal facets in catalysis/chemical reactions.

3.5 Conclusions

Nanocrystalline samples of CeO₂ have been synthesised using a simple one step, surfactant free, precipitation technique and by hydrothermal methods. Despite the differences in crystal shape and size that result, the lattice strain is found to follow a single scaling law with strain decreasing nonlinearly with increase in average crystal size. It was also found that the adoption of crystals with higher {100} facets show enhanced catalytic activity. Besides, the Ce³⁺ concentration varying with the shape of the catalysts to a maximum of ~44% in mixed morphology catalyst, it confers high OSC which also contributed to the enhanced catalytic activity. A remarkable feature which makes the mixed morphology catalyst promising candidate in soot oxidation is that they offer better catalytic activity even after thermal ageing at a temperature as high as 1000°C. The study demonstrates that engineered exposed crystal facets with low strain have high activity and for the first time suggests synthetic and processing methods that may provide materials with enhanced properties.

3.6 References

- [1] J. N. Armor, *Catal. Today* **2011**, *163*, 3.
- [2] R. Si, Y. W. Zhang, L. P. You, C. H. Yan, *Angew. Chem. Int. Ed.* **2005**, *44*, 3256.
- [3] R. Si, Y. W. Zhang, L. P. You, C. H. Yan, *J. Phys. Chem. B* **2006**, *110*, 5994.
- [4] F. Bondioli, A. B. Corradi, C. Leonelli, T. Manfredini, *Mater. Res. Bull.* **1999**, *34*, 2159.
- [5] T. S. Sreeremya, A. Krishnan, S. J. Iyengar, S. Ghosh, *Ceram. Int.* **2012**, *38*, 3023.
- [6] T. S. Sreeremya, A. Krishnan, A. P. Mohamed, U. S. Hareesh, S. Ghosh, *Chem. Eng. J.* **2014**, *255*, 282.
- [7] A. Atkinson, S. Barnett, R. J. Gorte, J. T. S. Irvine, A. J. McEvoy, M. Mogensen, S. C. Singhal, J. Vohs, *Nat. Mater.* **2004**, *3*, 17.
- [8] B. Murugan, A. V. Ramaswamy, *J. Am. Chem. Soc.* **2007**, *129*, 3062.
- [9] T. S. Sreeremya, K. M. Thulasi, A. Krishnan, S. Ghosh, *Ind. Eng. Chem. Res.* **2012**, *51*, 318.
- [10] H. Schulz, W. J. Stark, M. Maciejewski, S. E. Pratsinis, A. Baiker, *J. Mater. Chem.* **2003**, *13*, 2979.
- [11] H. X. Mai, L. D. Sun, Y. W. Zhang, R. Si, W. Feng, H. P. Zhang, H. C. Liu, C. H. Yan, *J. Phys. Chem. B* **2005**, *109*, 24380.
- [12] Y. W. Jun, J. S. Choi, J. Cheon, *Angew. Chem. Int. Ed.* **2006**, *45*, 3414.
- [13] S. C. Tjong, H. Chen, *Mat. Sci. Eng. R.* **2004**, *45*, 1.
- [14] S. Deshpande, S. Patil, S. Kuchibhatla, S. Seal, *Appl. Phys. Lett.* **2005**, *87*.
- [15] P. Miceli, S. Bensaid, N. Russo, D. Fino, *Nanoscale Res. Lett.* **2014**, *9*.
- [16] W. I. Hsiao, Y. S. Lin, Y. C. Chen, C. S. Lee, *Chem. Phys. Lett.* **2007**, *441*, 294.
- [17] W. Huang, *Top. Catal.* **2013**, *56*, 1363.

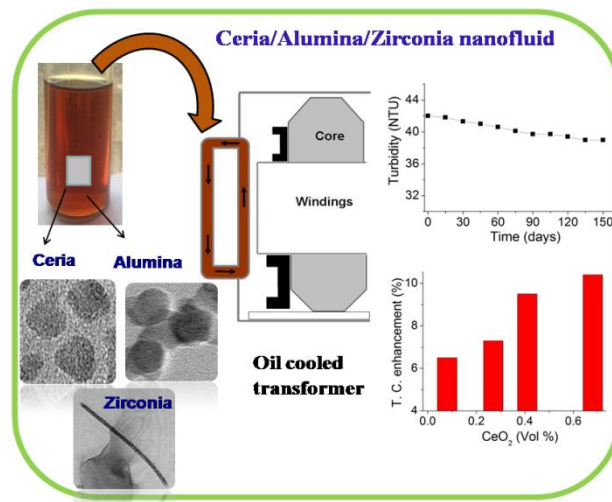
- [18] G. R. Rao, *Bull. Mater. Sci.* **1999**, 22, 89.
- [19] K. B. Zhou, X. Wang, X. M. Sun, Q. Peng, Y. D. Li, *J. Catal.* **2005**, 229, 206.
- [20] W. T. Chen, K. B. Chen, M. F. Wang, S. F. Weng, C. S. Lee, M. C. Lin, *Chem. Commun.* **2010**, 46, 3286.
- [21] Y. J. Guan, E. J. M. Hensen, Y. Liu, H. D. Zhang, Z. C. Feng, C. Li, *Catal. Lett.* **2010**, 137, 28.
- [22] S. W. Yang, L. Gao, *J. Am. Chem. Soc.* **2006**, 128, 9330.
- [23] M. Nolan, S. C. Parker, G. W. Watson, *Surf. Sci.* **2005**, 595, 223.
- [24] Y. Gao, W. Wang, S. Chang, W. Huang, *Chemcatchem* **2013**, 5, 3610.
- [25] Z.-A. Qiao, Z. Wu, S. Dai, *Chemsuschem* **2013**, 6, 1821.
- [26] J. C. Conesa, *Catal. Today* **2009**, 143, 315.
- [27] H. H. Huang, H. P. Chang, Y. T. Chien, M. C. Huang, J. S. Wang, *J. Cryst. Growth* **2006**, 287, 458.
- [28] P. Zhao, A. Ito, R. Tu, T. Goto, *Surf. Coat. Tech.* **2010**, 204, 3619.
- [29] P. Palmisano, N. Russo, P. Fino, D. Fino, C. Badini, *Appl. Catal. B* **2006**, 69, 85.
- [30] C. Sun, H. Li, L. Chen, *Energy Environ. Sci.* **2005**, 5, 8475.
- [31] S. Navaladian, B. Viswanathan, T. K. Varadarajan, R. P. Viswanath, *Nanoscale Res. Lett.* **2009**, 4, 181.
- [32] G. B. Harris, *Philos. Mag.* **1952**, Series 7, 43, 113.
- [33] X. D. Zhou, W. Huebner, H. U. Anderson, *Chem. Mater.* **2003**, 15, 378.
- [34] P. Bharali, P. Saikia, B. M. Reddy, *Catal. Sci. Technol.* **2012**, 2, 931.
- [35] T. Taniguchi, T. Watanabe, N. Sakamoto, N. Matsushita, M. Yoshimura, *Cryst. Growth Des.* **2008**, 8, 3725.
- [36] C. G. Hu, Z. W. Zhang, H. Liu, P. X. Gao, Z. L. Wang, *Nanotechnology* **2006**, 17, 5983.

- [37] M. Leoni, P. Scardi, *J. Appl. Crystallogr.* **2004**, *37*, 629.
- [38] P. Dutta, S. Pal, M. S. Seehra, Y. Shi, E. M. Eyring, R. D. Ernst, *Chem. Mater.* **2006**, *18*, 5144.
- [39] J. L. M. Rupp, A. Infortuna, L. J. Gauckler, *Acta Mater.* **2006**, *54*, 1721.
- [40] N. S. Ramgir, I. S. Mulla, K. P. Vijayamohanan, *J. Phys. Chem. B* **2005**, *109*, 12297.
- [41] J. Zhang, S. Ohara, M. Umetsu, T. Naka, Y. Hatakeyama, T. Adschiri, *Adv. Mater.* **2007**, *19*, 203.
- [42] Z. L. Wang, X. D. Feng, *J. Phys. Chem. B* **2003**, *107*, 13563.
- [43] N. Du, H. Zhang, B. G. Chen, X. Y. Ma, D. R. Yang, *J. Phys. Chem. C* **2007**, *111*, 12677.
- [44] K. B. Jaimy, V. P. Safeena, S. Ghosh, N. Y. Hebalkar, K. G. K. Warriar, *Dalton Trans.* **2012**, *41*, 4824.
- [45] A. Krishnan, T. S. Sreeremya, E. Murray, S. Ghosh, *J. Colloid Interface Sci.* **2013**, *389*, 16.
- [46] X. Liu, K. Zhou, L. Wang, B. Wang, Y. Li, *J. Am. Chem. Soc.* **2009**, *131*, 3140.
- [47] Y. Lee, G. He, A. J. Akey, R. Si, M. Flytzani-Stephanopoulos, I. P. Herman, *J. Am. Chem. Soc.* **2011**, *133*, 12952.
- [48] Z. Wu, M. Li, J. Howe, H. M. Meyer, III, S. H. Overbury, *Langmuir* **2010**, *26*, 16595.
- [49] S. Ghosh, D. Divya, K. C. Remani, T. S. Sreeremya, *J. Nanopart. Res.* **2010**, *12*, 1905.
- [50] G. Balducci, J. Kaspar, P. Fornasiero, M. Graziani, M. S. Islam, J. D. Gale, *J. Phys. Chem. B* **1997**, *101*, 1750.
- [51] G. R. Rao, B. G. Mishra, *Bull. Catal. Soc. India* **2003**, *2*, 122.
- [52] Y. Sheng, Y. Zhou, H. Lu, Z. Zhang, Y. Chen, *Chinese J. Catal.* **2013**, *34*, 567.
- [53] S. K. Meher, G. R. Rao, *J. Chem. Sci.* **2014**, *126*, 361.

Cerium oxide based Nanofluid as Efficient Coolant in Transformers - A Comparative Study with Alumina and Zirconia

4.1 Abstract

Low thermal conductivity is a primary limitation in the development of energy-efficient heat transfer fluids that are required in numerous industrial sectors. Recently submicron and high aspect ratio particles (NPs and nanotubes) were introduced into the heat transfer fluids to enhance the thermal conductivity (TC) of the resulting nanofluids. The aim of this chapter was to investigate the physico-chemical properties of nanofluids synthesized using inorganic oxide nanoparticles suspended in heat transfer fluids.



Transformer oil (TO) based nanofluids containing either ceria nanocubes (0.08–0.7 vol%), zirconia nanorods (0.03–1.7 vol%), and alumina nanospheres (0.02–0.2 vol%), were prepared via a two-step method. The thermal decomposition of their respective oleate precursor in a high boiling solvent was used for the fabrication of oil dispersible

surface modified NPs. Systematic monitoring of synthesis parameters such as reaction temperature and time (refluxing conditions) was carried out. The products were characterized by XRD, IR, PCS and TEM. The excellent solubility and stability of surfactant capped NPs in conventional organic solvents make them suitable for the preparation of oil-based nanofluids. The suitability of the nanofluids as heat transfer fluid was thoroughly investigated by measuring thermal conductivity, viscosity and particle size. Stability of the nanofluid was ensured by performing ageing studies. Effects of particle volume fraction and temperature on the thermal conductivity of oil based nanofluids were studied. Ceria/alumina/zirconia nanofluids showed almost identical flow behaviour in which a Newtonian flow at lower concentrations and shear thinning behaviour at higher concentrations was observed. The maximum thermal conductivity enhancement observed with ceria, alumina and zirconia nanofluids was 14.6, 10.3 and 12.4% respectively. All the prepared nanofluids exhibited long term stability (over five months), reasonable enhancement in thermal conductivity and good flow properties which make them adaptable in industrial heat transport applications.

4.2 Introduction

More recently, surface-modified rare-earth oxide nanocrystals have drawn more attention due to their unique properties and promising applications in, for example, UV shielding, luminescent displays, optical communication, biochemical probes, **nanofluids** and medical diagnostics.^[1] Nanofluids are dispersions of nanoparticles (NPs) in a basefluid like water, oil, ethylene glycol etc. and is mostly used in heat transport /cooling applications. Cooling is one of the most important challenges in devices in numerous industrial sectors. Despite the considerable amount of research and development focusing on industrial heat transfer requirements, major improvements in cooling capabilities have been lacking because conventional heat transfer fluids have poor heat transfer properties.^[2] One of the usual methods used to overcome this problem is to increase the surface area available for heat exchange, which usually leads to impractical or unacceptable increases in the size of the heat management system. Present quantum growth in the IT, innovative engineering, health care and electronic consumer goods sector has posed a challenge to improve the heat transfer capabilities of conventional heat transfer fluids.

An innovative idea of dispersing high thermally conductive solid NPs in the basefluid for improving the thermal conductivity of the fluid was developed by Dr. Choi of Argonne National Laboratory, US in 1995.^[3] Materials used for NPs include chemically stable metals (e.g., gold, silver, copper), metal oxides (e.g., alumina, zirconia, silica, titania) and carbon in various forms (e.g., diamond, graphite, carbon nanotubes, fullerene etc.). One of the major issues in synthesising stable nanoparticle suspensions is

to prevent agglomeration during synthesis and the surface coating process.^[4] Due to their high specific surface areas, and large surface-area to volume ratio, NPs exhibit a high reactivity and strong tendency towards agglomeration in suspension.^[5]

Heat transport driven failures are quite often in high voltage power transformers. Dielectric oils in high voltage transformers provide efficient cooling which can extend the life of transformers.^[6] These transformer oils require excellent nanoparticle (NP) dispersion, high heat conduction, as well as electrical insulation at the same time. Nanofluids with suspension stability for over months are not yet been reported. Motivated by their high inherent TC, metallic NPs such as Cu and Ag were also tested as coolants.^[7-9] Xuan et al. observed a 6% enhancement with 100 nm sized Cu NPs in TO and Kole et al. reported ~24% increase in thermal conductivity with 2 vol% Cu NPs dispersed in gear oil.^[7, 8] However, such nanofluids may cause arcing in high voltage transformer applications.

Unlike metallic counterparts, ceramic (metal oxide) NPs have significantly higher chemical stability over longer periods and are not susceptible to surface oxidation. These promising features together with low electrical conductivity make alumina, ceria, silica etc. suitable candidates in high voltage transformer applications.^[5] Philip et al. investigated the temperature dependence of thermal conductivity in non aqueous magnetic nanofluids.^[10] Alumina being a highly thermal conductive ($33 \text{ W.m}^{-1}.\text{k}^{-1}$) oxide has been tested as a candidate in heat transport application by several researchers.^[6, 11, 12] Choi et al. prepared TO based nanofluids of Al_2O_3 and AlN by a simple ball milling process.^[6] A TC enhancement of 40% in pump oil was reported by Xie et al. with

dispersion of 60 nm alumina NPs (5 vol%) where as 1 vol% of 20 nm alumina NPs enhanced the TC of TO by 14%.^[12] Stearic acid modified spherical MoS₂ NPs in the size range of 50–100 nm were utilised by Li et al. for preparing oil based nanofluids and reported a TC enhancement of ~18% with 1 wt% NP loading at 40°C.^[13] These discoveries clearly indicate that nanofluid technology can provide exciting new opportunities to develop nanotechnology-based coolants for a variety of innovative engineering and medical applications. Hence, the subject of nanofluids is of great interest worldwide for basic and applied research.

In spite of the fact that cerium oxide NPs have been well studied in areas such as catalysis,^[14] chemical-mechanical polishing,^[15] in SOFC's^[16, 17] etc., limited attempts have been made in fabricating ceria nanofluids.^[18, 19] In order to make cerium oxide NPs dispersible in hydrophobic/oleophilic solvents, a proper surface modifier and a facile synthetic strategy has to be identified. Surface modification of rare earths has long been a topic of research. Recent reports suggest that synthesis via an organic route may be preferable to aqueous methods for the preparation of stable nanofluids in apolar solvents, due to the greater control of particle size and polydispersity.^[20] Numerous methods such as hydrothermal,^[21] alcohothermal,^[22, 23] thermal decomposition,^[24] and aqueous precipitation^[14, 15] have previously been reported for the synthesis of organophilic CeO₂ NPs with good control of size. Among these, hydrothermal and alcohothermal methods require high pressure and/or temperature equipment which involves additional costs, safety measures and processing time. Although aqueous precipitation methods are simple, greener and inexpensive, they require multiple processing steps. Solvothermal decomposition of an organic precursor on the other hand is a facile, one step method to

synthesise monodispersed NPs with narrow size distribution.^[20] A versatile method was developed by Kim et al. for continuous synthesis of surface modified cerium oxide NPs.^[18] Hyeon and co-workers identified a novel method for preparing surface modified, monodisperse NPs employing a metal oleate complex as the precursor.

In the present thesis, a metal-oleate complex is prepared by reacting inexpensive and environment friendly compounds, namely, metal salts (chlorides/nitrates) and sodium oleate. Further, a facile reflux technique employing a metal oleate precursor in diphenyl ether in the presence of oleic acid as the capping agent has been attempted for preparing oleophilic NPs of ceria, alumina and zirconia. Stable oil-based nanofluids with varying solid content were prepared by dispersing these capped NP's in transformer oil. The corresponding thermal conductivity and rheological tests were performed and the dependence of TC on the concentration and temperature has been evaluated. The nanofluids demonstrated higher thermal conductivity than the basefluid (oil). An attempt is also made to propose the mechanism of thermal conductivity enhancements in the prepared nanofluids. So, this chapter will mainly focus on the surface modification of the NPs by selecting suitable surfactants based on the carrier fluid, to prepare stable, low viscous nanofluids with improved thermal conductivity.

4.3 Experimental

Cerium nitrate hexahydrate ($\text{Ce}(\text{NO}_3)_3 \cdot 6\text{H}_2\text{O}$, 99.99%, Indian Rare Earth Ltd., India), Zirconium oxychloride ($\text{ZrOCl}_2 \cdot 8\text{H}_2\text{O}$, 99.99%, Indian Rare Earth Ltd., India), Aluminium nitrate nonahydrate ($\text{Al}(\text{NO}_3)_3 \cdot 9\text{H}_2\text{O}$, Merck, India) and were used as the precursor metal salts for ceria, zirconia and alumina. The sodium hydroxide (Merck,

India), oleic acid (Alfa Aesaer, India), ethanol (Merck, India) and cyclohexane (Merck, India) used were of analytical reagent grade. Diphenyl ether (DPE, 99%) and oleyl amine (70%) were procured from Sigma Aldrich. Double distilled water was used for preparation of solutions.

4.3.1 Preparation of metal-oleates (*M-oleates*, *M=Ce, Al and Zr*)

In a typical preparation, weighed amounts of metal precursors and Na-oleate were dissolved in a solution consisting of 85 ml EtOH, 40 ml H₂O and 100 ml cyclohexane. The mixture was reacted at 80°C for 4 h and the organic phase was collected and washed three times with 30 ml water. The remaining cyclohexane was evaporated slowly at 80°C leaving a solid residue.

4.3.2 Reflux synthesis of surface modified nanocrystals

In a typical synthesis, weighed amount of the freshly synthesized metal oleate was dissolved in 40 ml diphenyl ether in a round bottom flask. To this, oleic acid (OA) and oleylamine were added and the reaction mixture was refluxed at its natural boiling point (~265°C) for different time intervals. The molar ratio of metal oleate:oleic acid:oleylamine was 1:3:3. As the reaction proceeded, the solution became slightly cloudy and brown, which demonstrated the formation of nanocrystals. After cooling, acetone was added to precipitate the OA coated NPs. The precipitate was washed thoroughly with acetone and dried. The resulting precipitate was easily dispersible in many nonpolar solvents including hexane and toluene. The capped NPs were dispersed in transformer oil (TO) by sonicating for about 10 min. To understand the reaction

mechanism, the refluxing conditions were slightly varied, for instance, the time of reaction was varied.

4.4 Results and discussion

4.4.1 Characterisation of precursor oleates

The precursor oleates of ceria and zirconia appeared to possess a gel type nature (Fig. 4.1A and C) whereas aluminium oleate (Fig.4.1B) had a waxy nature.

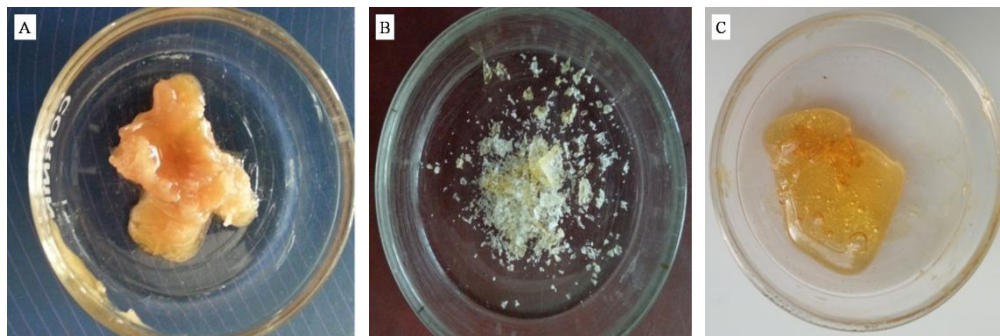


Fig. 4.1 Optical photographs of A) cerium oleate, B) aluminium oleate and C) zirconium oleate.

4.4.1.1 IR spectral investigation of precursor oleates

The respective oleate precursors of ceria, alumina and zirconia were characterized using FT-IR spectra and presented in Fig. 4.2. The characteristic IR bands for metal carboxylates are in the range of $1650\text{-}1510\text{ cm}^{-1}$ for the asymmetrical vibrations and $1400\text{-}1280\text{ cm}^{-1}$ for the symmetrical vibrations.^[25] FTIR spectra of all the oleates contain several strong bands in the $\nu(\text{COO}^-)$ region: 1725 , 1601 , 1510 , and 1430 cm^{-1} . The band at 1725 cm^{-1} can be assigned either to the carbonyl group of oleic acid or to asymmetric vibrations of unidentate carboxylate group.^[25] The bands in the range $2800\text{-}3000\text{ cm}^{-1}$ are

the CH₂ and CH₃ symmetric and asymmetric stretching vibrations.^[4] The rocking vibration at 715 cm⁻¹ is also typical of (CH₂)_n chains with n > 3.^[5] The peak characteristic of M-O-C groups were indicated with arrow heads in **Fig. 4.2** in cerium oleate (675 cm⁻¹),^[26] aluminium oleate (1060, 780 cm⁻¹)^[27] and zirconium oleate (1450, 1560 cm⁻¹).^[28]

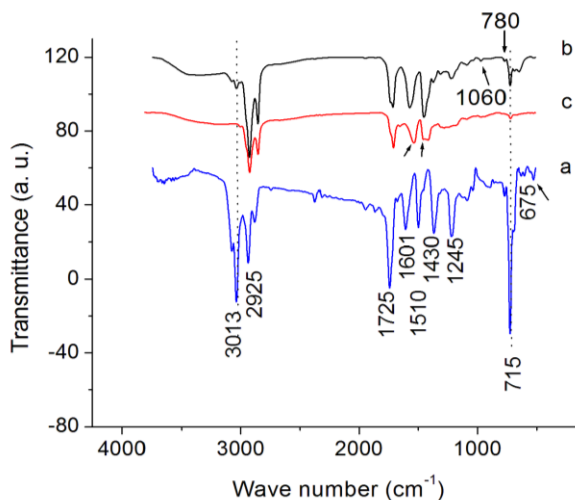


Fig. 4.2 FT-IR spectra of oleate precursors of (a) ceria (b) alumina and (c) zirconia.

Oleic acid coated NPs of ceria, alumina and zirconia have been fabricated by refluxing respective oleate precursors in diphenyl ether solvent for different time intervals. More details on each system are discussed in section 4.4.1.

4.4.2 Thermogravimetric analysis of surface modified NPs

Fig. 4.3 shows the thermogravimetric profiles of surface modified/oleic acid coated NPS of ceria, alumina and zirconia. A two step weight loss was observed in the temperature range of 200-500°C in the case of both ceria and zirconia whereas alumina NPs exhibited a three step weight loss with the total weight loss in the range 39-63%. The major weight loss in the temperature range of 200-500°C, was due to the oleic acid

decomposition.^[29] The weight loss observed in each system are tabulated below for comparison.

Table 4.1 Weight loss observed in the TGA patterns of surface modified nanoparticles

System	Weight loss (%)		
	Total (200-480°C)	200-430°C	430-480°C
Ceria	42.5	35	7.5

System	Weight loss (%)			
	Total (200-530°C)	(200-350°C)	(350-480°C)	(480-530°C)
Alumina	63.4	16.5	32.5	14.4

System	Weight loss (%)		
	Total (200-520°C)	(200-426°C)	(426-480°C)
Zirconia	39.4	24.1	15.3

It is clear from the data that decomposition process of the oleic acid occurring in each nanosystem is different. This may be due to the fact that as prepared NPs are terminated with different crystal facets with different adsorption activity.^[30, 31] In the case of boehmite alumina NPs, a further weight loss of 14.4% was observed after 480°C which extends upto 530°C, may be due to the transformation of boehmite alumina to gamma alumina.^[32] The amount of surfactant coated on to the surface is in the range 30-49% by weight of the NPs. The amount of surfactant in lipophilic ceria reported by Ghosh et al.

was <30% and was dispersible in less viscous non polar solvents such as hexane, toluene etc.^[15]

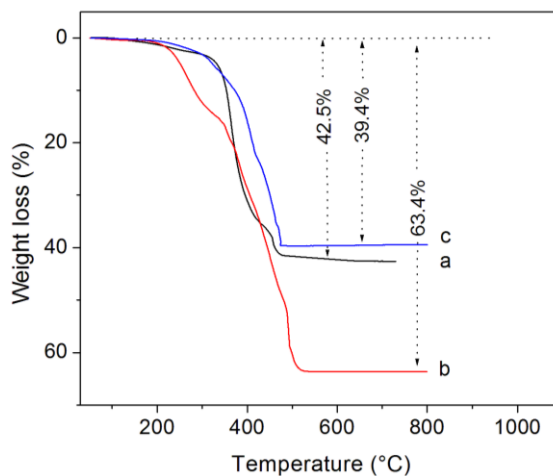


Fig. 4.3 TGA patterns of surface modified NPs of (a) ceria, (b) alumina and (c) zirconia.

Actually, the high percentage of the organic part contributes to the high solubility of the nanoparticles in common organic solvents and especially in high viscous transformer oil and in turn adds to the colloidal stability of the dispersions.

4.4.3 Ceria fluid

4.4.3.1 Powder characterisation

The phase composition of the solid products obtained by thermal decomposition of cerium oleate in DPE for different time intervals (1, 2 and 4h respectively in CeDPE1, CeDPE2 and CeDPE4) was determined by X-ray diffraction. The XRD patterns of CeDPE and FT-IR spectra for CeDPE4 and OA are presented in Fig. 4.4. The XRD patterns of capped ceria nanoparticles show finger-print reflections of typical fcc cubic CeO_2 of $Fm\bar{3}m$ space group.^[14, 16] Fig. 4.4 shows the crystallization and growth of CeO_2 crystals by thermal decomposition of Ce-oleate by extending the reflux time. One hour

reflux treatment on Ce-oleate initiated the formation process of cubic ceria crystals (CeDPE1) as indicated by the appearance of small humps corresponding to (111), (220) and (311) crystal facets which grew sharper on further extending the reflux time to 4 h in CeDPE4. The average CeO₂ crystal size estimated from the line broadening of the (111) X-ray reflection using Scherrer's formula for CeDPE4 is ~ 4.1 nm.^[33, 34]

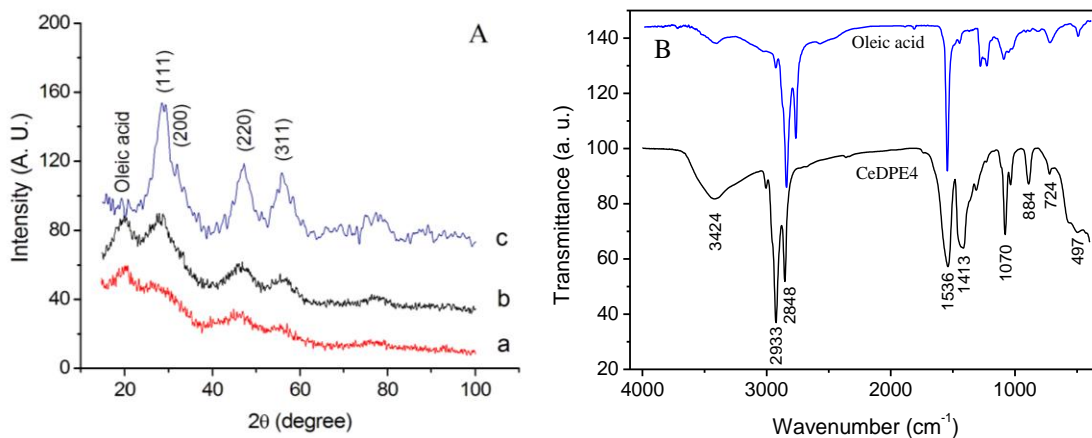


Fig. 4.4 (A) XRD patterns of a) CeDPE1, b) CeDPE2, c) CeDPE4, and (B) FT-IR spectra of CeDPE4 and oleic acid.

A peak at $\sim 20^\circ$ 2θ was observed in all the DPE refluxed samples and was attributed to the presence of OA surfactant^[35] and the relative intensity of this peak with respect to that of cubic ceria became less prominent with increasing refluxing time. The broadened peaks are due to the nanocrystalline nature of the ceria product. The FT-IR measurements of CeDPE4 also provided supporting evidence for the formation of capped ceria nanocrystals (Fig. 4.4B). The characteristic bands of the oleyl group are present in both the spectra. The CeO₂ crystals with chemisorbed OA showed two strong vibrational bands at 2845 and 2927 cm⁻¹ due to the methyl $\nu_s(-CH_3)$ and the $\nu_{as}(CH)$ groups. These peaks are known to be the characteristic modes of the methylene ($-HCH-$) chains that are present in OA. The rocking vibration at 715 cm⁻¹ is also typical of $(CH_2)_n$ chains with n

>3 [17].^[15] The free carbonyl stretching mode of the acid is visible at 1711 cm^{-1} . In comparison, the intensity of this band is reduced in the capped sample, and strong absorption bands corresponding to the asymmetric and symmetric stretching bands of the RCOO^- group appeared at 1536 and 1413 cm^{-1} respectively. Furthermore, the difference of 123 cm^{-1} between both stretching modes is characteristic of a bidentate coordination of the carboxylate to a metal atom. The broad peak at $\sim 3400\text{ cm}^{-1}$ is assigned to absorbed H_2O or OH groups. The multiple peaks in the range $1000\text{--}1700\text{ cm}^{-1}$ can be assigned to the CH, COO and H_2O modes or their mixtures. The peak corresponding to the Ce–O stretch is observed at 497 cm^{-1} and the bands at 1070 and 1350 cm^{-1} are due to $\nu(\text{Ce–O–Ce})$ vibration [17].^[15]

The size and morphology of the ceria particles were examined by transmission electron microscopy (Fig.4.5). TEM images of CeDPE4 showed well separated, monodisperse, nanocrystals of CeO_2 in the size range $3\text{--}7\text{ nm}$ with an average of $5.8\pm 1\text{ nm}$ which is some what larger than the same calculated from X-ray peak broadening (4.1 nm). Crystal size determined from XRD profile using the Scherrer equation^[33, 34] underestimates the grain size as it ignores broadening of the diffraction peaks due to the microstrain in the OA coated crystals.^[15] There were no evidence of agglomeration and the surfactant capped nanocrystals are mostly cubic in shape with the exception of few irregular shaped particles. The high intensity (111) lattice fringes characteristic of cubic ceria was observed in the HR-TEM image as shown in the inset of Fig. 4.5B. The XRD patterns together with TEM analysis clearly indicates that 4 h refluxing at 265°C in DPE is essential for the formation of well crystallized ceria NPs. The particle size

(hydrodynamic diameter) of CeO₂ NCs (CeDPE4) in toluene suspension, measured by photon correlation spectroscopy (PCS) is shown in Fig. 4.6.

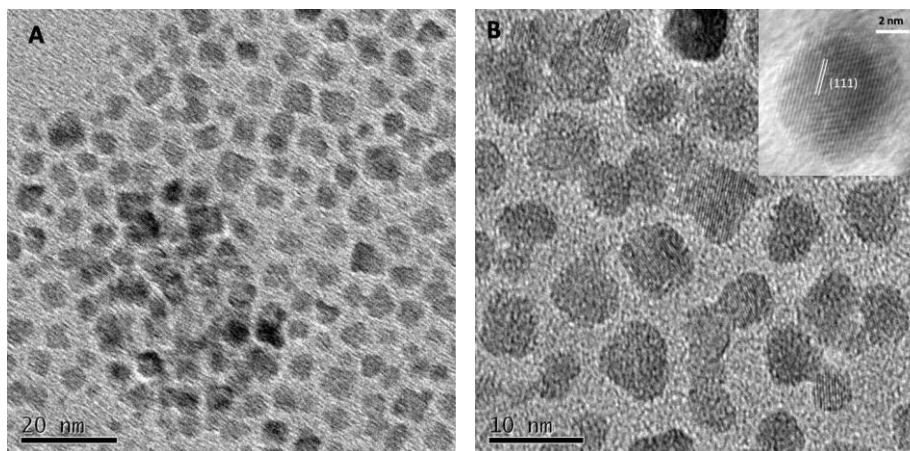


Fig. 4.5 (A) Bright-field TEM, and (B) high-resolution TEM images of CeO₂ nanoparticles in CeDPE4. Prominent (111) lattice fringes characteristic of cubic ceria is marked in HR-TEM image shown in the inset of (B).

The hydrodynamic diameters of these materials are in good agreement with the same from TEM and XRD measurements. The reproducibility of the synthetic procedure in terms of size of the crystalline product was within acceptable limits (~3%). TEM provides the core diameter of cerium oxide particles and DLS data reports the hydrodynamic diameter of the nanocrystal–OA core-shell spherical structures.^[36] The z-average (D_{PCS}) of 7.4 nm have shown a difference of 1.6 nm from D_{TEM} mainly due to the surfactant coating, a value of ~0.8 nm is very close to 0.9 nm for the length of OA chain.^[15]

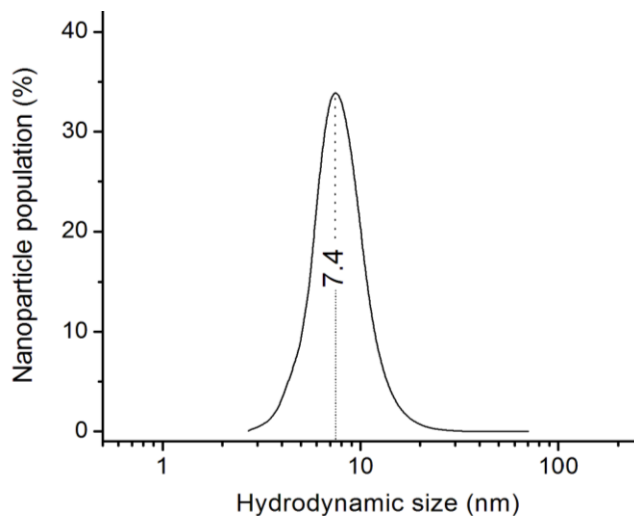


Fig. 4.6 Particle size distribution as measured by photon scattering (number distribution) of suspensions of surface modified ceria (CeDPE4) in toluene.

The PDI value of 0.33 and un-clustered, isolated particles in TEM images confirm the monodispersed nature of CeO_2 nanoparticles.

4.4.3.2 Mechanism of thermolysis

Metal oxide NPs were prepared by decomposing metal-oleate complex in a high boiling solvent. To understand the formation procedure of the NPs, the reaction was studied by varying reaction temperature and reaction time. It was found that below the refluxing point of the solution (265°C , bp of diphenyl ether) there was no nanocrystal produced. The formation of NCs takes place only above 265°C . At temperatures above 265°C the precursors decompose and yield nuclei for metal oxide crystallites. These crystallites rapidly grow over several hours and consume the available soluble metal. In general, the mechanism can be summarised as follows: metal carboxylates decompose on heating near or above 300°C to form metal oxide nanocrystals alongwith some

byproducts.^[37] It is thought that the decomposition reaction proceeds via the formation of free radicals from metal oleates as shown in eqn 4.1 and 4.2.



From the reaction between the simultaneously formed $\text{M-O}\cdot$ and $\text{M}\cdot$ species, M-O-M links arise. This should result in the formation of “ MO_2 ”, as a final solid product.^[38] Subsequently, the oleate molecules generated by oleylamine assisted ionisation of oleic acid leads to the formation of MO_2 NPs (NPs) with negatively charged oleate ions adsorbed on the surface and the core of the metal oxide remaining positively charged.^[20]^{39]} However, a detailed and stoichiometric description of this process has not yet been established. Crystallite growth appears consistent with “Ostwald ripening,” where the higher surface free energy of small crystallites makes them less stable than larger crystallites with respect to dissolution in the solvent. The net result of this ability gradient in dispersion is a slow diffusion of material from the surfaces of small particles to the surfaces of larger particles. Crystal growth by this kind of mass transport can result in the production of colloidal dispersions from systems that may initially be polydispersed.^[40] Capping groups can slow down the growth kinetics by presenting a significant steric barrier to the addition of material to the surface of a growing crystallite. The oleate molecule coordinates the surface of ceria nanocrystallites and permits slow steady growth at temperatures above 265°C . Steady controlled growth results in NPs of a consistent crystal structure.^[41]

4.4.3.3 Rheological properties of nanofluids

The surface modified NPs were dispersed in TO to prepare the nanofluids. The flow behaviour of ceria based nanofluids as measured by viscosity is shown in Fig. 4.7. Ceria nanofluids upto 0.4 vol% solid loading showed Newtonian behaviour with negligible effect on the viscosity against shear rate as there were no significant interactions among the particles. This may be due to the lower concentration of CeO_2 , resulting in relatively large separation among the particles.

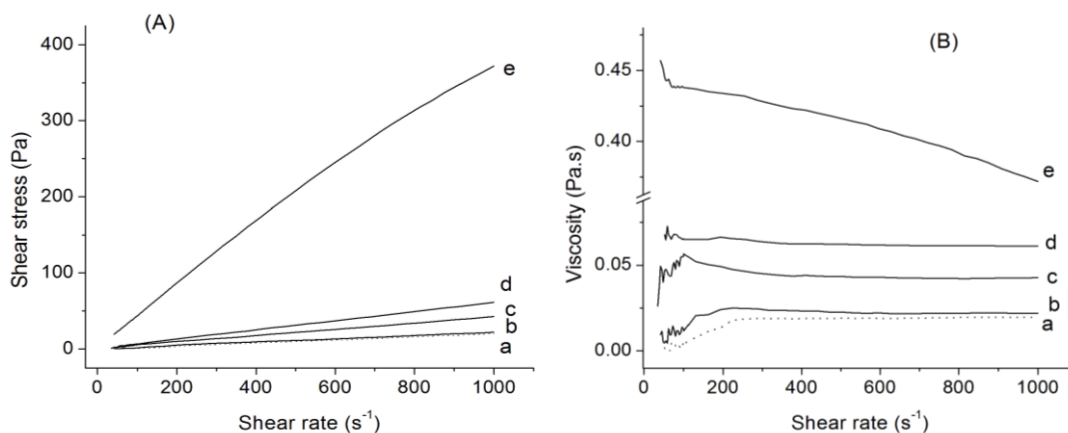


Fig. 4.7 Flow curves [(A) shear stress and (B) viscosity against shear rates] for a) base TO, b) 0.08 vol%, c) 0.27 vol%, d) 0.41 vol%, and e) 0.7 vol% CeDPE4 dispersed nanofluids in TO.

Nanofluid with 0.7 vol% CeO_2 showed shear-thinning behaviour at low shear rates, after which ideal viscous behaviour was observed (Fig. 4.7). Higher loading of ceria NPs in TO produced gel-like suspensions. Shearing causes the three-dimensional network of the gel disintegrate, resulting in a decrease in the interaction among the particles and hence a resultant lowering in the viscosity.^[42] The effect of temperature on viscosity of nanofluids is presented in Fig. 4.8. The viscosity data had a standard deviation within $\pm 2\%$ for all the

CeO₂ fluids. Both the nanofluids and the base TO showed a decrease in viscosity with increase in fluid temperature, the difference being the rate of change.

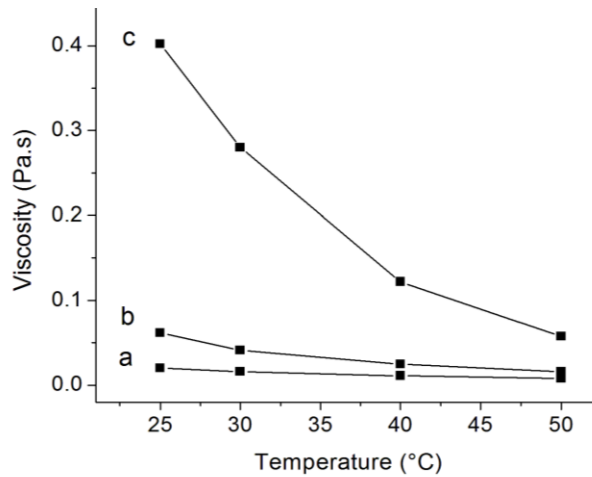


Fig. 4.8 The variation of viscosity with temperature for a) base oil, b) CeDPE4 fluid in TO with solid loading of 0.41%, and c) the same with 0.7 vol% CeDPE4 loading.

This is because, as the temperature increases, the average kinetic energy of the molecules in a liquid increases.^[43] The greater average kinetic energy of the molecules more easily overcomes the attractive forces that tend to hold the molecules together. This could possibly imply that the nanofluids are indeed true colloidal solutions. The viscosity of the 0.7 vol% fluid decreased significantly from initial 0.402 Pa.s at 25°C to 0.058 Pa.s at 50°C. The CeO₂ fluids show a nonlinear decrease in viscosity with temperature with the rate being faster in the lower temperatures (Fig. 4.8). A similar behaviour was reported by Jamshidi et al.^[44] The effect is more pronounced in fluids with higher loading as the surface modified CeDPE4 might form net-work structure among themselves.^[5] The reduction in viscosity was about 59, 74 and 86% for TO, 0.41 and 0.7 vol% nanofluids respectively when temperature was increased from initial 25 to 50°C. The reduction in viscosity of 0.7 vol% fluid at 50°C (86%) is comparable to that reported by Kole et al.

(90%) for 1 vol% Cu based nanofluid.^[7] The change in viscosity with temperature above 40°C is not significant. Accordingly, transformer oil based nanofluids with higher NP loading may find suitable for use as transformer oil at normal temperature of transformer operations (~80°C).^[5]

4.4.3.4 Thermal Conductivity of Nanofluids

The thermal conductivity enhancement of ceria nanofluids (k_{eff}) is calculated using equation 4.4.^[4, 5]

$$k_{eff} = \frac{(k_{nf} - k_{bf})}{k_{bf}} \times 100 \quad (4.4)$$

where k_{nf} and k_{bf} are the thermal conductivity of nanofluid and basefluid respectively. Fig. 4.9 shows the TC enhancements in ceria fluid against its loading at 25°C as well as measurement temperature (30-50°C). The thermal conductivity measurements were carried out at least three times on each fluid. The standard error in the TC measurements was within $\pm 3\%$. It is apparent that the TC of each nanofluid was higher than that of its base fluid and increased almost linearly with increased loading of the nanoparticles. TC enhancements of 6.5 and 9.5% were observed with 0.08 and 0.4 vol% ceria loaded TO based nanofluids respectively. The suspensions turned slowly into syrupy liquid on further increasing ceria loading. The highest concentration of ceria used in this study is 0.7 vol% and that resulted in a 10.3% increase in TC (Fig. 4.9) when compared with the TC of base TO. The maximum enhancement observed with ceria fluids which are viscous gel-like suspensions with higher loading of CeO₂ NPs. Fluids with lower extent of loading show small increases in TC. A similar behaviour was observed in silica system

by Burgi et al. and Botha et al. in which they reported maximum TC enhancements with gel type fluids.^[42, 45] Many authors pinpointed nanoconvection due to Brownian motion as the main mechanism of heat transfer in nanofluids.^[9, 46]

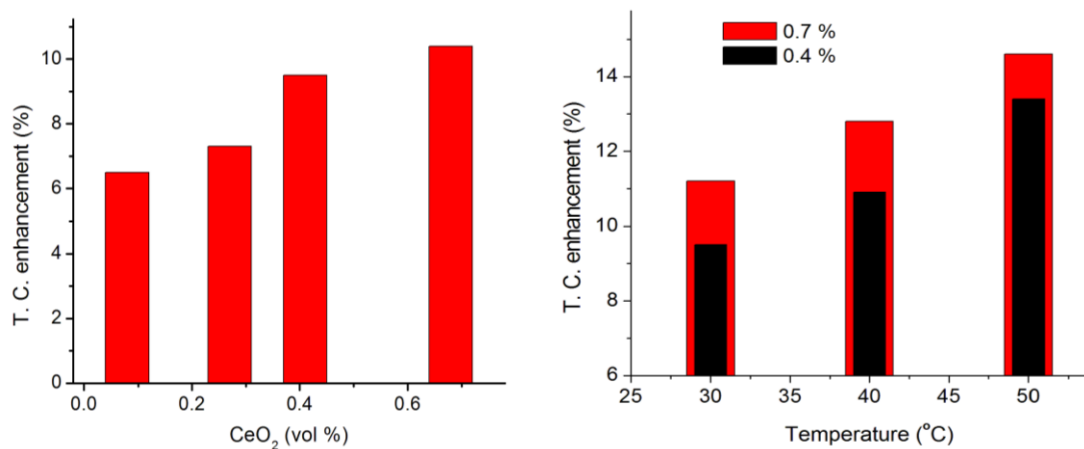
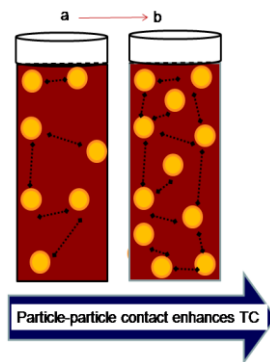


Fig. 4.9 (A) Thermal conductivity of ceria fluids with 0.08-0.7 vol% CeDPE4 loading at 25°C and (B) the variation in thermal conductivity of 0.41 and 0.7% ceria fluids at 30, 40, and 50°C.

In this study, the heat transfer may possibly be through particle-particle contact also in addition to Brownian motion which becomes less prominent in viscous gel-like suspensions as described in Scheme 4.1.

Despite ceria being a poor heat conductor, observed increase in thermal conductivity may be due to i) small particle size and, ii) compatibility of capped particles with TO. The viscosity of nanoparticle-in-oil suspensions increased with increase in particle concentration in the nanofluid (Fig. 4.7).



Scheme 4.1. Enhanced particle-particle contact on moving from low concentration to high concentration (a to b) of NP's which adds to TC.

However, the particle loading cannot be increased indefinitely as the nanofluid forms a gel beyond certain critical concentration. A maximum of 14.6% TC enhancement was observed with 0.7 vol% nanofluid at 50°C. The increase in TC with temperature is consistent with the previously reported results which were all carried at temperatures below 80°C.^[13, 47] An increase in temperature leads to enhanced Brownian motion of the particles, which improves the rate of heat transfer. The Brownian motion of the particles has not contributed directly to the mass transport enhancement, but it enhanced the convection currents because of an increase in the nanoscale stirring of the liquid.^[10]

4.4.4 Alumina nanofluid

Barron and coworkers reported the synthesis of organophilic boehmite alumina by modification with p-hydroxybenzoic acid to produce boehmite alumina supported catalysts useful in olefin polymerisation.^[48] Boehmite alumina is composed of Al-O double layers which are interconnected by hydrogen bonds between the hydroxyl groups as shown in Fig. 4.10A.



It has been shown that carboxylic acids ($-\text{CO}_2\text{H}$) react with boehmite, $[\text{Al}(\text{O})(\text{OH})]_n$, to afford the appropriate carboxy-alumoxane.

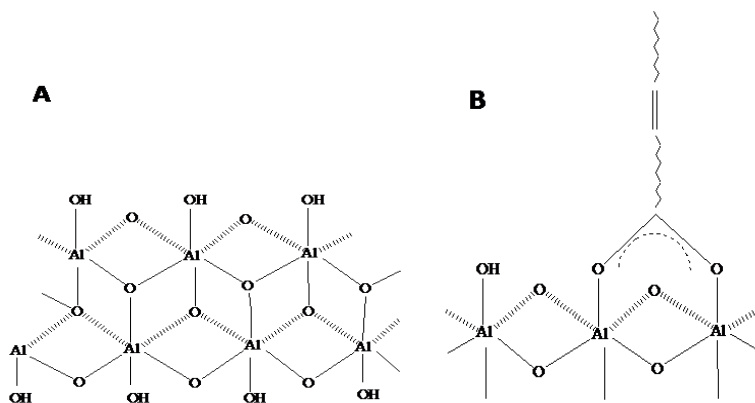


Fig. 4.10 A) Structure of pure boehmite alumina and B) oleate modified organophilic boehmite alumina.

The chemical modification of the generated boehmite during non-aqueous reflux synthesis in presence of oleic acid thus generates organophilic boehmite which can be schematically shown in Fig. 4.10B. As a consequence of the modification, these boehmite particles are highly dispersible in organic media.

4.4.4.1 Powder characterisation

The XRD patterns of samples obtained by refluxing aluminium oleate in DPE for different time intervals are shown in Fig. 4.11. Ageing was performed for 10, 15, 24 and 48 h (AIDPE10, AIDPE15, AIDPE24 and AIDPE48 respectively). The precursor complex of aluminium oleate thermally decomposed to boehmite alumina NCs, a precursor of alumina by ageing for a period of 24 h at the refluxing temperature. Thermal decomposition of aluminium oleate generates nuclei of amorphous alumina hydrate gels. Boehmite alumina/ γ -alumina nanocrystallites are formed at the expense of amorphous

alumina hydrate gels when aluminium oleate suspension is heated which subsequently form HO–Al–O network. The mechanism is shown schematically in Fig. 4.13.

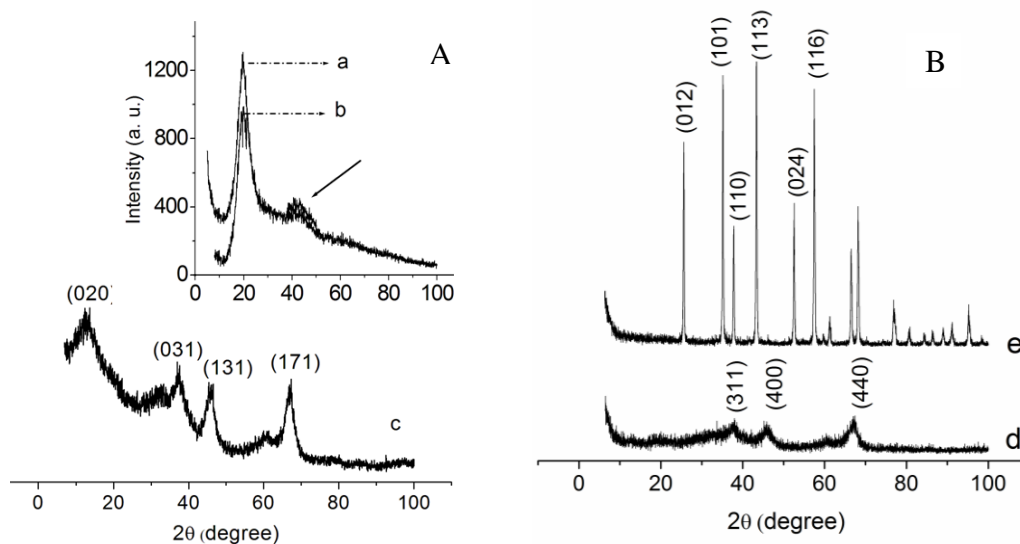


Fig. 4.11 (A) XRD pattern of (a) AIDPE10, (b) AIDPE15 and (c) AIDPE24, (B) AIDPE24-900 and AIDPE24-1000 (d and e respectively).

Two reflections centred at around 20 and 45° 2θ appeared in the XRD pattern of AIDPE10 and AIDPE15 sample (shown as inset of Fig. 4.11). The first high intense peak can be ascribed to the surfactant^[35, 49] and the relatively less intense peak at 45° 2θ can be assigned to boehmite alumina or γ -alumina. The XRD patterns together with TEM analysis clearly indicate the formation of relatively amorphous boehmite NPs by 24 h refluxing at 265°C in DPE. On increasing the refluxing time to 24 h, four distinct reflections at 2θ values 13.9, 38.1, 45.8 and 67.1° appeared in the XRD pattern as shown in Fig. 4.11c, which is in agreement with the standard for boehmite alumina (JCPDS No. 832384) NPs. The (020) reflection is slightly shifted towards smaller scattering angles, which is due to a particle size effect, as observed previously.^[50, 51] The broadened peaks

are due to the nanocrystalline nature of boehmite alumina. Interestingly, it was observed that further refluxing (upto 48 h in the present study) doesn't have much effect on crystallinity/phase transformation. This may be due to the low temperature and normal pH maintained during synthesis as the formation of α -alumina is normally reported to occur near or above 1000°C (XRD not presented here).^[52, 53] The XRD patterns in Fig. 4.11B indicate that on calcination at 900 and 1000°C boehmite alumina is first transformed to its dehydrated counterpart i.e., γ -alumina and finally to α -alumina.

The size and morphology of the boehmite alumina particles were examined by transmission electron microscopy (TEM) as shown in Fig. 4.12. TEM images of 24 h refluxed sample showed spherical nanocrystals of boehmite alumina with an average size 30.00 ± 3 nm. It is evident from the HR-TEM images that the NP's form chain like structures which may be due to the self assembly of NP's in a linear fashion (Fig. 4.13). The particle size distribution of boehmite alumina suspension, measured by photon correlation spectroscopy (PCS), is shown in Fig. 4.12D. Stable dispersion of boehmite alumina in toluene was used for the size measurements. The polydispersity index (PDI) estimates the width of the distribution. The PCS data showed the presence of NPs with z-average (D_{PCS}) 63 nm with PDI 0.38. PDI value of 0.38 does not indicate a monodisperse suspension.^[54] Careful examination of the PCS spectra reveal that the size distribution is bimodal as indicated by a sharp peak with majority of particles being 63 nm and a less intense broad peak with particles in the range 150-300 nm.

This is in accordance with the observation made by Barron et al., that unlike other forms of oxide nanoparticle, the alumoxanes are not mono-dispersed but have a range of particle sizes.

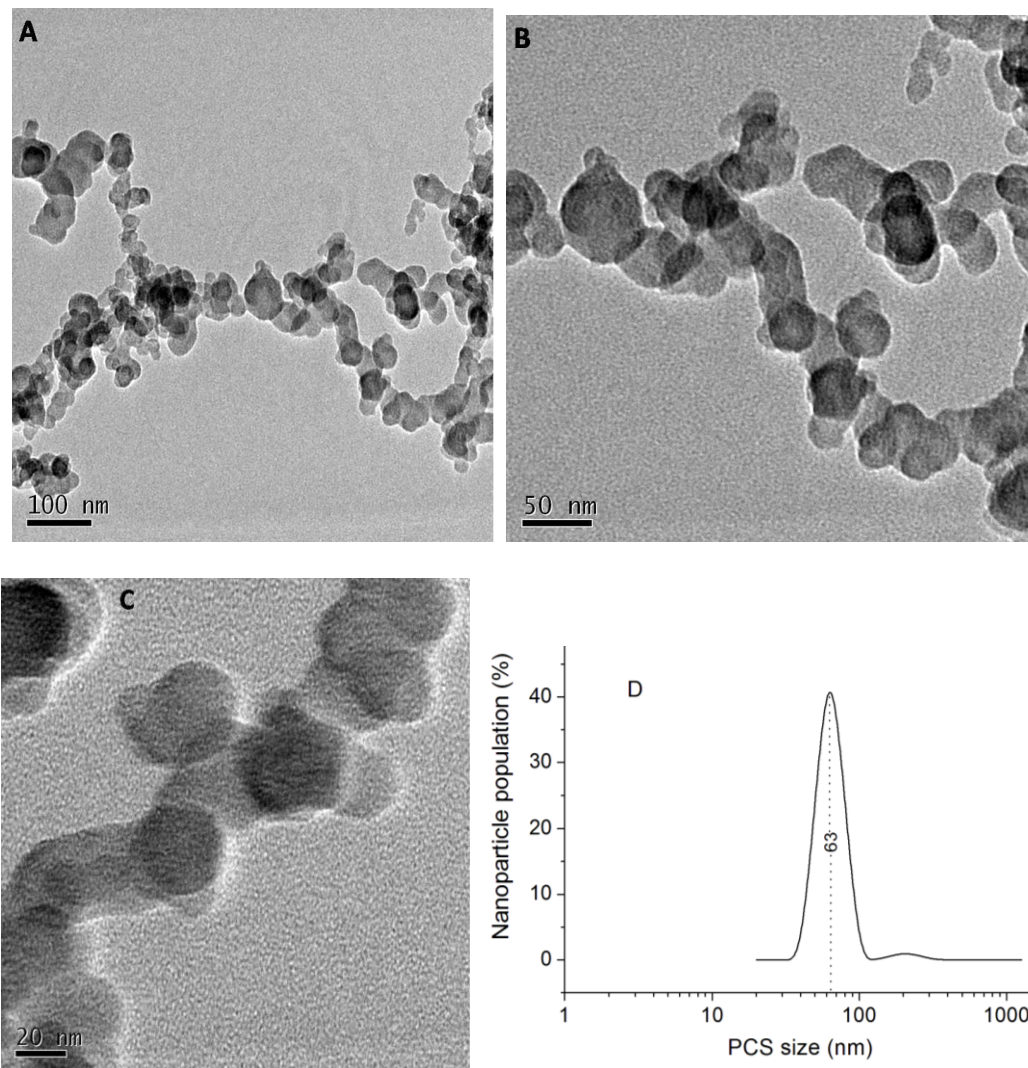


Fig. 4.12 TEM (A-C) images and particle size distribution (D) of suspensions of AIDPE24 in toluene.

The D_{PCS} of ~ 63 nm could be due to the pearl chain like nanostructure with average hydrodynamic diameter of $\sim 2 \times D_{TEM}$ which is 60 nm.

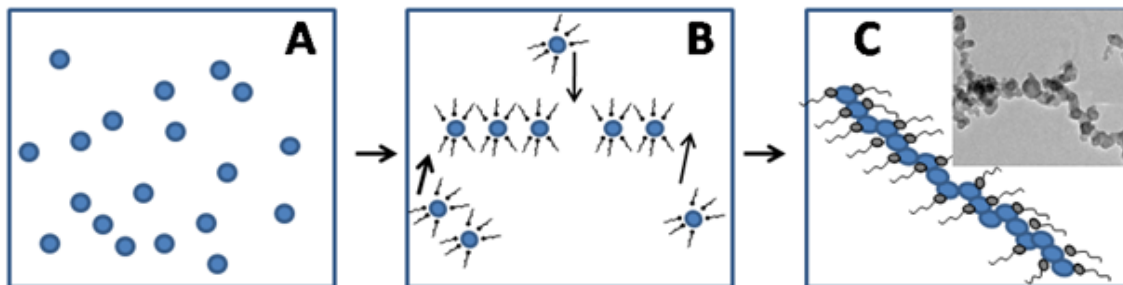


Fig. 4.13 Schematic illustration showing the formation of pearl chain like nanostructures of boehmite alumina during the reflux process.

The FT-IR measurements also provided supporting evidence for the formation of organophilic boehmite alumina nanocrystals (Fig. 4.14). FT-IR spectra contain the bands at ~ 1145 , 775 , 615 , and 490 cm^{-1} , typical of boehmite alumina.^[49, 55]

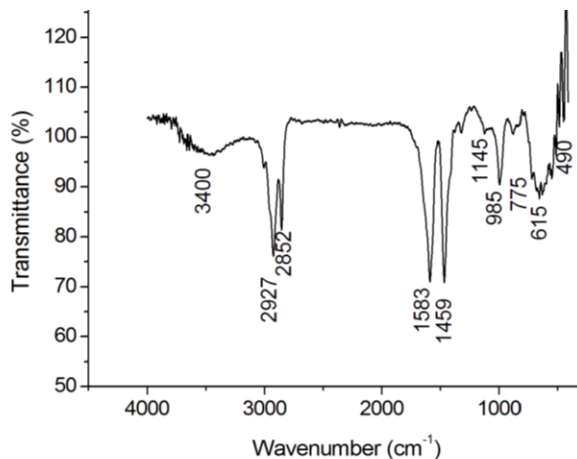


Fig. 4.14 IR spectra of AIDPE24 showing the formation of surface functionalised nanoparticles.

The absorption bands in the region between $1000\text{--}400$ cm^{-1} correspond to Al–O vibration.^[56] The characteristic bands of the oleyl group are present in the spectra. The surface modified boehmite alumina crystals showed two strong vibrational bands at 2845 and 2927 cm^{-1} due to the methyl $\nu_s(\text{CH}_3)$ and the $\nu_{\text{as}}(\text{CH})$ groups. These peaks are known to be the characteristic modes of the methylene (CH_2) chains that are present in OA. The

rocking vibration at 715 cm^{-1} is also typical of $(\text{CH}_2)_n$ chains with $n > 3$.^[5] The free carbonyl stretching mode of the acid is visible at 1711 cm^{-1} . In comparison, the intensity of this band is reduced in the capped sample, and strong absorption bands appeared at 1536 and 1413 cm^{-1} can be assigned to the asymmetric and symmetric stretching bands of the RCOO^- group respectively. Furthermore, the difference of 123 cm^{-1} between both stretching modes is characteristic for a bidentate coordination of the carboxylate to a metal atom. The broad peak at $\sim 3400\text{ cm}^{-1}$ is assigned to absorbed H_2O or OH groups. The multiple peaks in the range $1000\text{-}1700\text{ cm}^{-1}$ can be assigned to the CH, COO and H_2O modes or their mixtures.

4.4.4.2 Formation mechanism

The mechanism of formation of aluminium oxyhydroxide or simply boehmite from aluminium oleate in presence of oleic acid and oleylamine can be summarised as follows. Oleylamine performs a nucleophilic attack of one carbonyl group of the oleate ligand and generates a hydroxyl group on the metal centre with the liberation of N-oleyl oleylamide. The hydroxyl group bound to the metal atom then induces condensation with another metal centre to form a M-O-M bond. This step represents the starting point of crystallisation. In principle, condensation between two hydroxyl groups would lead to the elimination of water and presence of water in the reaction system facilitates formation of aluminum oxyhydroxide. The added oleylamine performs dual function, first it could enhance the release of carboxylate anions from oleic acid and guarantee a stronger adsorption of carboxylate anions onto the NP surfaces,^[57] second it performs a nucleophilic attack on the oleate ligand of metal precursor.

4.4.4.3 Viscosity measurements

The flow behaviour of boehmite alumina based nanofluids of different vol% prepared by dispersing boehmite NP's in TO as the basefluid are shown in Fig. 4.15. Boehmite alumina nanofluids upto 0.1 vol% showed Newtonian behaviour may be due to the much lower concentration of NP's, resulting in a relatively large separation distance between the particles and hence no significant interaction forces between the particles, which allowed it to have a negligible effect on the viscosity.

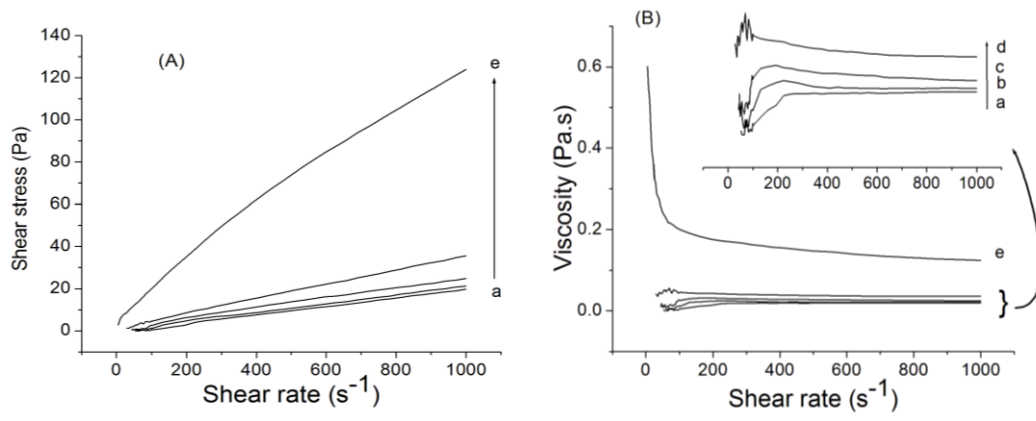


Fig. 4.15 Flow curves for a) transformer oil, b) 0.02 vol %, c) 0.07 vol %, d) 0.11 vol%, and e) 0.18 vol% boehmite alumina dispersed in oil.

Boehmite nanofluid of 0.18 vol% showed shear-thinning behaviour at low shear rates, after which ideal viscous behaviour was observed (Fig. 4.15). The viscosity of boehmite suspensions increased with increase in its loading. Shearing most likely caused the three-dimensional network of gel like suspensions to disintegrate, resulting in a decrease in the interaction forces among the particles and hence a lowering in the flow resistance.^[58] The effect of temperature on viscosity of one of the prepared nanofluids was investigated and shown in Fig. 4.16.

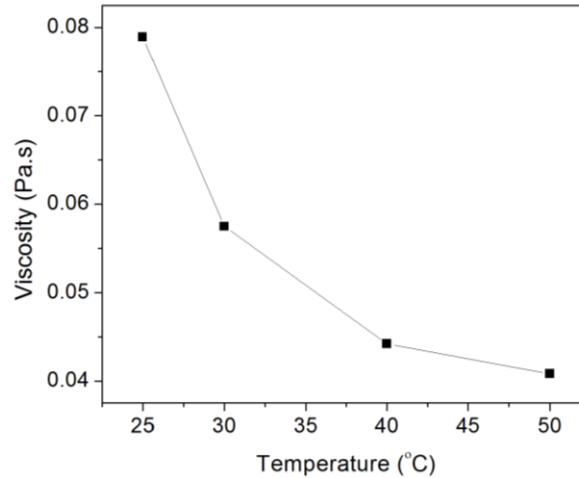


Fig. 4.16 The variation of viscosity with temperature for hydrated aluminium oxide fluid with 0.18% (volume) loading.

A drastic decrease in viscosity with an increase in temperature was observed in the case of both the basefluid (Fig. 4.8a) and nanofluid (Fig.4.16), a phenomenon similar to a typical liquid without any suspended NPs. This could possibly imply that the nanofluids are indeed true colloidal solutions.

4.4.4.4 *Thermal Conductivity of Nanofluids.*

The thermal conductivity enhancement of boehmite alumina nanofluids (k_{eff}) is calculated using eqn 4.4. Figure 4.17A shows the thermal conductivity enhancement of nanofluid with solid loading ranging from 0.02 to 0.23 vol%. It is apparent that the thermal conductivity of each boehmite alumina nanofluid was higher than that of its base fluid and increased linearly with increasing mass fraction of the NPs. A 5.8% increase in thermal conductivity was observed with 0.02 vol% boehmite alumina and 7.3% for 0.1 vol% boehmite alumina. The suspensions became more gel-like with increasing concentration of boehmite alumina. The highest concentration of boehmite alumina under

investigation was 0.23 vol% which resulted in 8.1% increase in thermal conductivity (Fig. 4.17). The maximum enhancement seen with boehmite alumina–TO samples is with the gel-like suspensions. Low wt% samples will only show small increase in thermal conductivity when compared to the higher wt% samples.

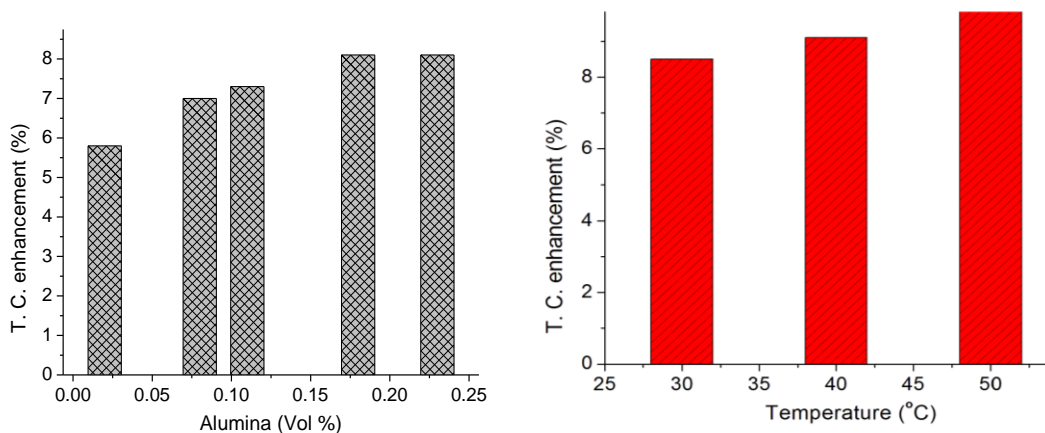
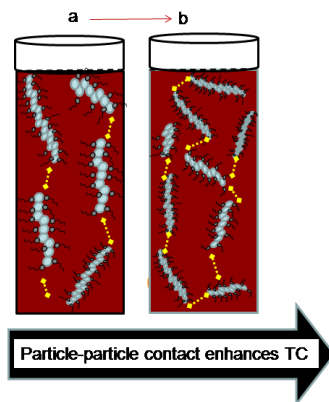


Fig. 4.17 (A) Thermal conductivity of boehmite alumina with concentrations ranging from 0.02 vol% to 0.23 vol% at 25°C. (B) The variation in thermal conductivity of 0.18 volume percent boehmite alumina fluid at temperatures 30, 40, and 50°C.

As in the case of ceria system, the predominant heat transfer mechanism may be particle-particle contact (Scheme 4.2) because Brownian motion becomes less prominent in the case of gel like suspensions.

Boehmite alumina, even at low level of loading in TO has shown reasonably high enhancement in thermal conductivity which may be due to i) small particle size, ii) extended pearl-chain like structure which helps in easy transfer of heat, and iii) enhanced dispersity offered by OA. Thermal conductivity of 0.18 vol% boehmite alumina nanofluid was measured at 30, 40 and 50°C and the corresponding TC enhancement against temperature is plotted in Fig. 4.17B.



Scheme 4.2 TC increases due to enhanced inter-particle contacts as we move from low to high concentration (a to b).

An increase in temperature leads to enhanced Brownian motion of the particles, which improves the rate of heat transfer. The Brownian motion of the particles does not contribute directly to the mass transport enhancement, but it enhances the convection currents because of an increase in the nanoscale stirring of the liquid.^[10]

4.4.5 Zirconia nanofluid

Zirconia NPs were prepared by the thermal decomposition of zirconium-oleate complex in high boiling solvent. The decomposition reaction was carried out by varying the reaction time. Sample details along with reaction conditions are provided in Table 4.2. Apparently, no ZrO_2 crystal formation was observed by holding the reaction mixtures at temperatures below the boiling point of DPE solvent (265°C). Metal carboxylates generally decompose on heating at $\geq 300^\circ\text{C}$ to form metal oxide nanocrystals along with some by-products.^[37]

Table 4.2 Sample details along with reaction conditions.

Sample code	Refluxing medium	Time of reflux (h)	Dispersibility in oil
ZDPE4	DPE	4	High
ZDPE7	DPE	7	High
ZDPE10	DPE	10	High

It was proposed that the decomposition reaction proceeds via the formation of free radicals from metal-oleates as shown in equations 4.1, 4.2 and 4.3.

4.4.5.1 Powder characterisation

The phase composition of the capped zirconia nanocrystals obtained by thermal decomposition of zirconium oleate in different solvents was determined by X-ray diffraction. The XRD profiles of zirconia crystals and FT-IR spectrum for ZPDE10 are shown in Fig. 4.18. The growth of zirconia crystals was found to increase with increasing the holding time at the reflux temperature. All the X-ray profiles show a distinct diffraction peak at $\sim 20^\circ 2\theta$ which is attributed to the presence of OA surfactant in the solids.^[35] The relative intensity of this peak at $\sim 20^\circ 2\theta$ to that of (111) reflection pertaining to monoclinic zirconia decreases with increase in reflux time indicating progressive formation of zirconia crystals. Four hour reflux treatment on Zr-oleate initiated the formation process of monoclinic zirconia crystals (ZDPE4) as indicated by the appearance of small humps corresponding to (111) and (220) crystal facets which grew sharper on further extending the reflux time to 10 h in ZDPE10. The profiles show three major finger print reflections from zirconia crystals of typical monoclinic structure

with the space group: $P2_1/c$ (according to JCPDS card No. 830943) in ZDPE10. Zirconia crystals grew larger to $\sim 2.3 \pm 1$ nm (D_{XRD}) with time through Ostwald ripening when the reflux time was extended to 10 h in ZDPE10 (>1 nm in ZDPE7).

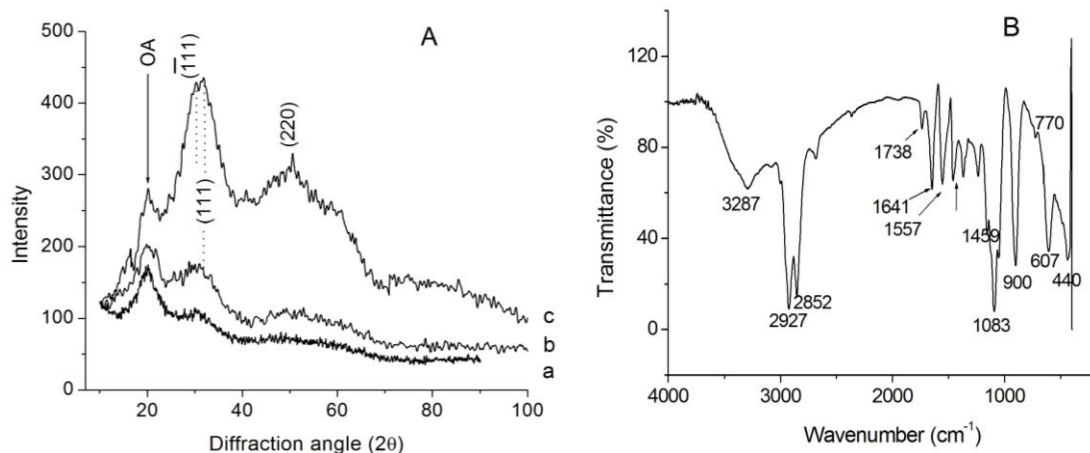


Fig. 4.18 (A) X-ray diffraction patterns of (a) ZDPE4, (b) ZDPE7, and (c) ZDPE10. (B) Fourier transform infrared spectra of ZDPE10.

The shift in the peak position from that of free oleic acid (1708 cm^{-1}) is due to the chemical interaction with the atoms on NP surfaces.^[59] The bands in the range $2800\text{--}3000\text{ cm}^{-1}$ are the CH_2 and CH_3 symmetric and asymmetric stretching vibrations. The broad peak at $\sim 3400\text{ cm}^{-1}$ is assigned to absorbed H_2O or $-\text{OH}$ groups. The multiple peaks in the range $1000\text{--}1700\text{ cm}^{-1}$ can be assigned to the CH , $-\text{COO}$ and H_2O modes or their mixtures. The strong peaks in the range $400\text{--}700\text{ cm}^{-1}$ are Zr-O vibration modes.^[59] The peak at $\sim 770\text{ cm}^{-1}$ is a typical feature for monoclinic zirconia.^[60]

The size and morphology of the zirconia NPs were examined by bright-field transmission electron microscopy (TEM) as shown in Fig. 4.19. The TEM image of ZDPE10 shows zirconia NPs of mostly ellipsoidal shape of average size ~ 4 nm along with scattered nanorods (Fig. 4.19B). The formation of well crystallised zirconia

nanocrystals in ZDPE10 (10 h refluxing in DPE) is evident from the HR-TEM images provided in Fig. 4.19.

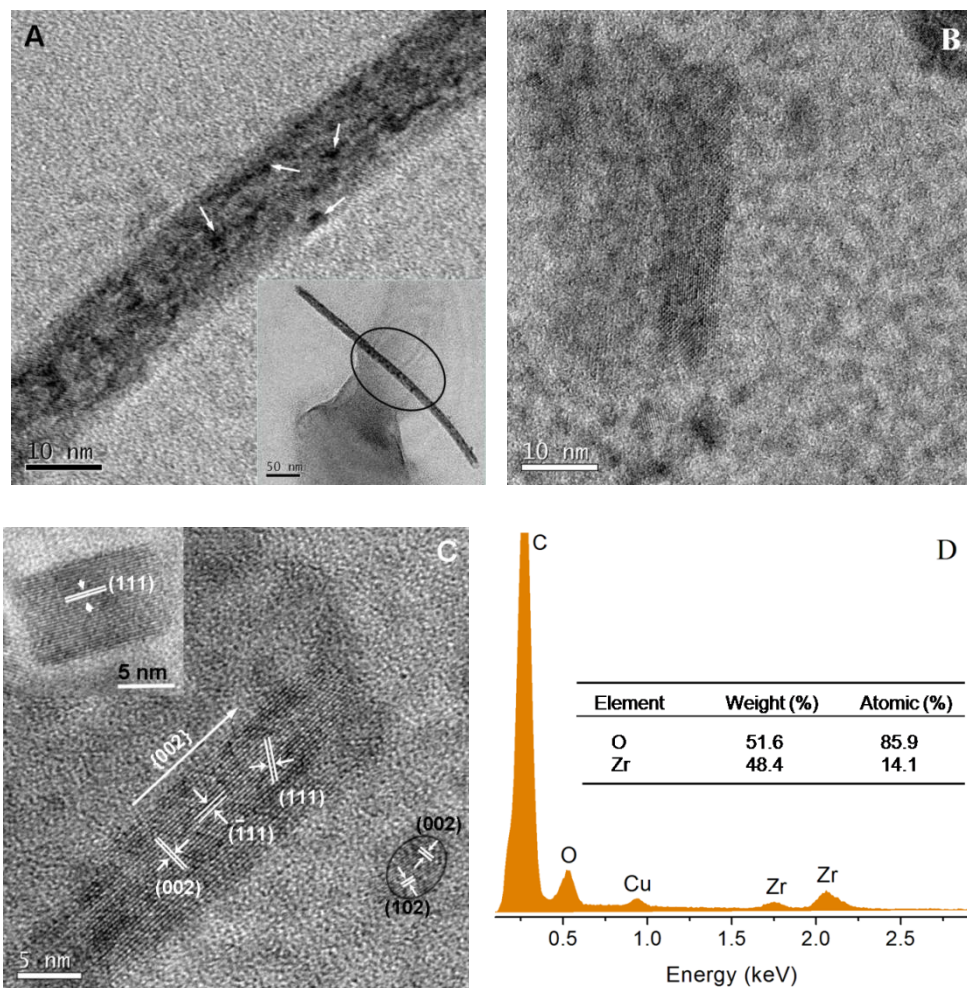


Fig. 4.19 TEM images (A and B) of monoclinic zirconia nanocrystals (ZDPE10), (C) High-resolution TEM image of ZDPE10 of mixed morphology, and (D) EDS spectrum of ZDPE10.

The predominant (111), $(\bar{1}11)$, and (002) lattice fringes with corresponding interplanar spacing of 0.31, 0.28 and 0.26 nm respectively, were observed in the HR-TEM image of the nanorods and NPs confirming that zirconia produced has monoclinic structure (JCPDS card No. 830943).^[61] A small number of NPs are sticking onto the surface of the nanorods as indicated by arrow marks in Fig. 4.19A. The nanorods have an average

length of ~ 300 nm and diameter ~ 8 nm. During the longer duration of reflux treatment (>7 h) the ellipsoidal crystals have shown 1D growth in the [002] direction. The atomic ratio of zirconium to oxygen obtained from the EDS spectrum (Fig. 4.19D) confirms that the oxygen content in the sample is slightly in excess of the stoichiometric requirement for ZrO_2 due to the presence of chemisorbed oleic acid in the sample.

The size of ZrO_2 NPs (ZDPE10) in toluene suspension was measured by photon correlation spectroscopy (PCS) and the size (hydrodynamic diameter) distribution is shown in Fig. 4.20.

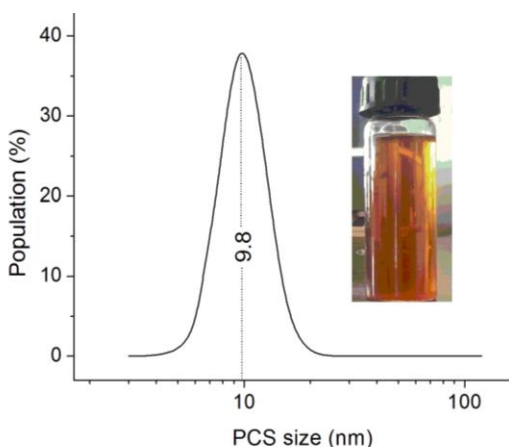


Fig. 4.20 Particle size distribution (number) of capped ZDPE10 suspension in toluene as measured by photon scattering technique. An optical image of transparent colloidal ZrO_2 dispersion in TO is shown as inset.

The polydispersity index (PDI) for the distribution is 0.35 which indicates that the distribution is relatively wide.

4.4.5.2 Rheological Properties of Nanofluids

As nanofluids for heat transport are used under continuous-flow conditions, the rheological properties play a vital role in determining its suitability in real applications. NPs suspended in nonpolar liquids, such as mineral oil and other hydrocarbons, are known to increase the viscosity of the fluid by forming transient interparticle linkages

arising out of the net attractive forces among the particles.^[42] The flow behaviour of zirconia based nanofluids as measured by viscosity is shown in Fig. 4.21.

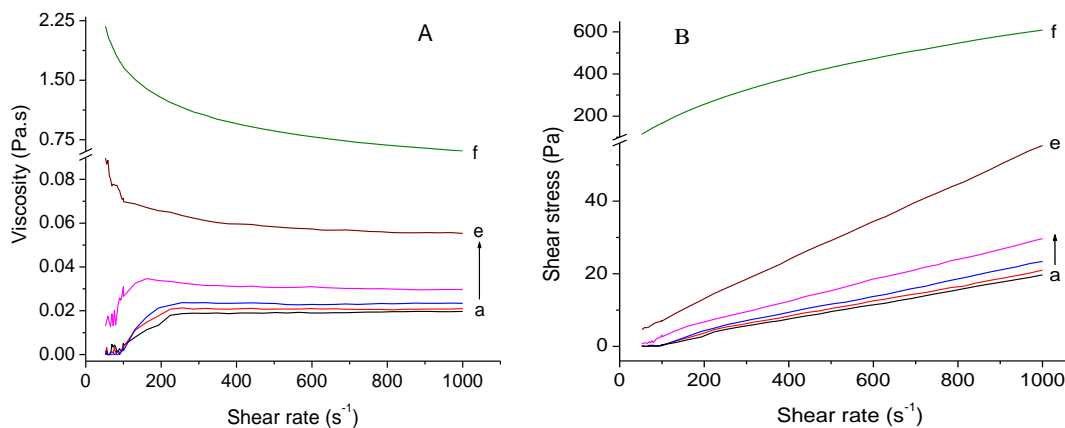


Fig. 4.21 Flow curves for transformer oil based nanofluids with a) pure oil, b) 0.03, c) 0.07, d) 0.34, e) 0.68, and f) 1.7 vol% ZDPE10.

Suspensions containing ≤ 0.8 vol% zirconia NPs displayed Newtonian behaviour with negligible effect on the viscosity against shear rate as there were no significant interactions among the particles. This is due to the large separation among the particles in lower concentration of ZrO_2 . On increasing the ZrO_2 content to 1.7 vol%, shear-thinning was observed at low shear rates, followed by ideal viscous flow behaviour (Fig. 4.21). The suspensions transformed into viscous fluid forming three-dimensional network on increasing the zirconia NP loading. Shear force is responsible for the disintegration of the gel structure, resulting in a decrease in viscosity on further increase in shear force. Breaking of the gel-structure decreases the interaction forces among the particles lowering the flow resistance.^[38]

The effect of temperature on viscosity of transformer oil containing 1.7 vol% zirconia is shown graphically in Fig. 4.22.

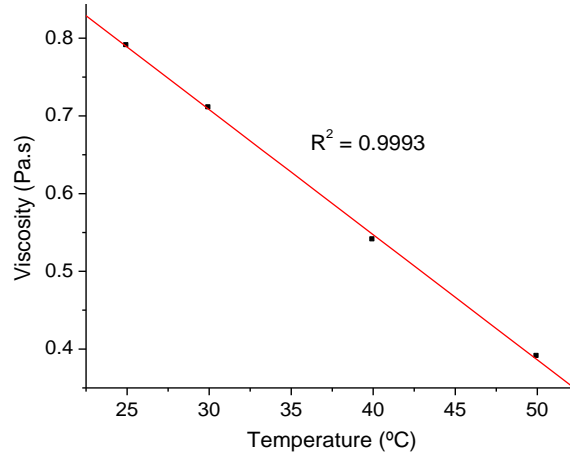


Fig. 4.22 The variation of viscosity with increase in temperature for TO fluid containing 1.7 vol% zirconia.

The viscosity of fluid containing 1.7% ZDPE10 in TO decreased linearly (goodness of linear fit is 0.9993) from initial ~0.8 Pa.s at 25 °C to ~0.4 Pa.s at 50 °C (Fig. 4.22). This phenomenon is typical to a liquid without any suspended NPs which could possibly imply that the nanofluids are indeed true colloidal suspensions.

4.4.5.3 Thermal Conductivity of Nanofluids

Fig. 4.23 shows the effective thermal conductivity enhancements in nanofluids as a function of volume fraction of ZDPE10 as well as fluid temperatures. As expected, the thermal conductivity of each zirconia nanofluid was higher than that of its base fluid and increased almost linearly with increase in NPs loading. A 5.1% increase in thermal conductivity was observed with 0.03 vol% ZrO₂ NP in TO which further increased to ~7.3% when the loading was increased to 0.68 vol%. The nanofluid with highest ZrO₂ loading in this study (1.7 vol%) resulted in a 10.3% increase in thermal conductivity (Fig. 4.23). Nanofluids with <1 vol% NP loading have shown marginal enhancements in

thermal conductivity. Most of the reports on heat transport fluids attributed Brownian motion as the main mechanism of heat transfer in nanofluid systems.

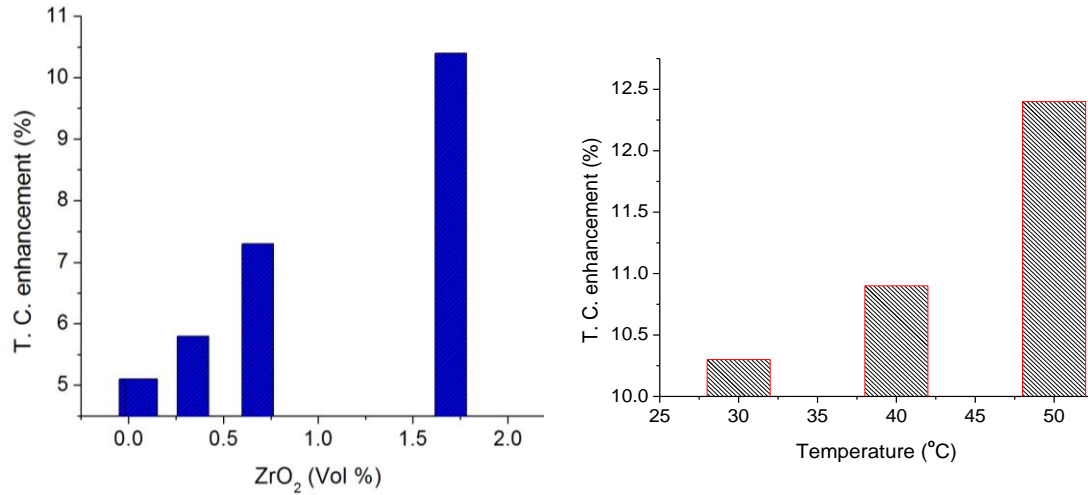
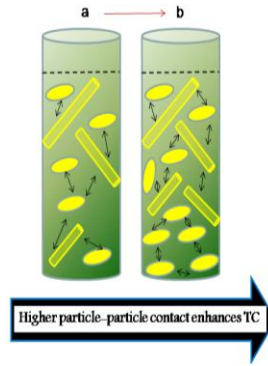


Fig. 4.23 (A) Thermal conductivity of zirconia nanofluids as a function zirconia NP (ZDPE10) loading in transformer oil measured at 25°C, (B) The variation in thermal conductivity of 1.7 vol% zirconia fluid at 30, 40, and 50°C. Accuracy in the k measurement was within $\pm 5\%$.

In the present investigation, the heat transfer is driven via particle-particle contact, in addition to Brownian motion which is less prominent in the case of gel-like suspensions (Scheme 4.3). Thermal conductivity of 1.7 vol% ZDPE10 nanofluid increased from an initial $\sim 10.35\%$ measured at 30° to $\sim 12.4\%$ when the temperature of measurement was increased to 50°C (Fig. 4.23B). An increase in temperature leads to enhancement in Brownian component of the particles, which improves the rate of heat transfer assuming the transport through contact mode remains constant.



Scheme 4.3 Enhanced TC with higher particle-particle contact in fluids from low to high loading of ZDPE10 NPs (column *a* to *b*).

The thermal conductivity of the nanofluids depends not only on the volume fraction, but also on the shape of the particles.^[62] Rod-shaped particles are reported to be more efficient in heat transfer compared to the spherical counterparts.^[6] Zirconia being a low thermal conductivity material ($TC \sim 2 \text{ W.m}^{-1}\text{k}^{-1}$), has shown reasonably high $\sim 10.3\%$ enhancement in thermal conductivity at 1.7 vol% loading. This is attributed to i) appreciable fraction of small particles, ii) rod like/elongated morphology of remaining particles, and iii) compatibility of capped particles with TO. However, the viscosity of NPs in oil suspensions increases almost exponentially with increase in NP loading creating a virtual limit.

4.4.6 *Stability of nanofluid systems*

Turbidity measurements

In addition to thermal conductivity, the most important property which decides the suitability of a nanofluid in industrial heat transport applications is its suspension stability. Some of the researchers employed turbidity measurement as a suitable method for ensuring stability of nanofluids.^[18, 62] The stability of the nanofluids was monitored by

performing turbidity measurements (transmittance of visible light) over a time period of five months and presented in Fig. 4.24. The nanoparticles dispersed in transformer oil were visibly stable at room temperature for months without changing their appearance, and no detectable precipitate could be found. The turbidity of the base transformer oil was measured as 1 NTU.

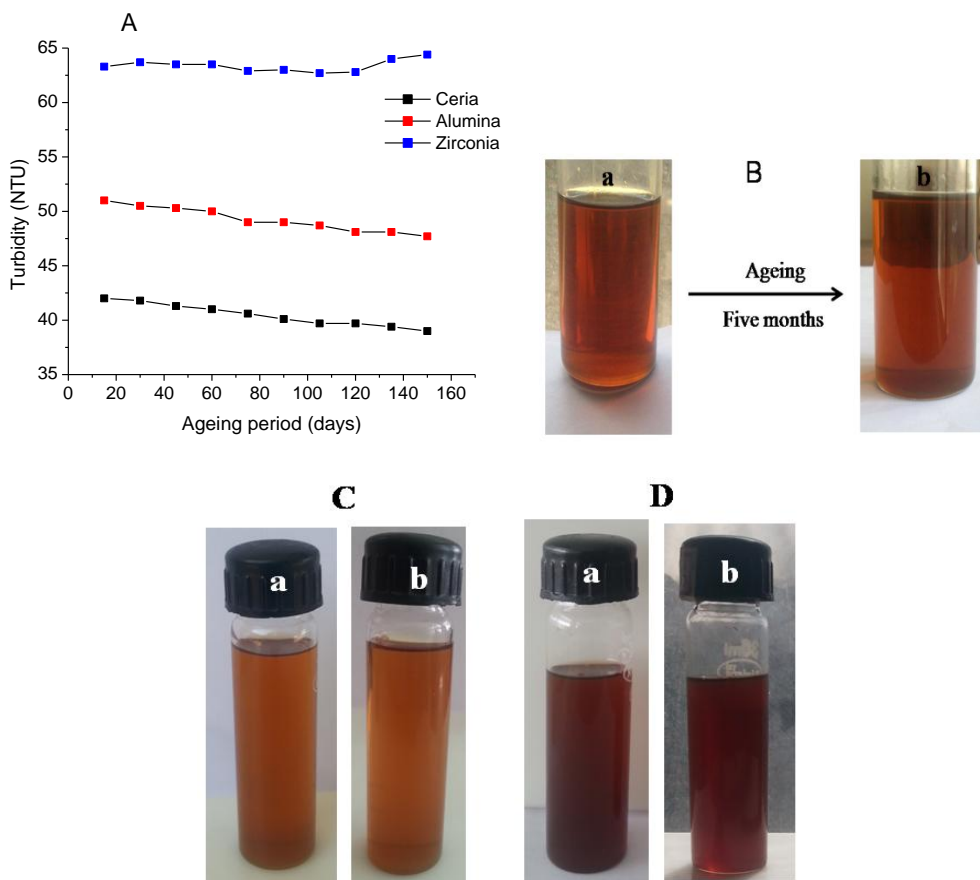


Fig. 4.24 (A) Stability of Ceria, alumina and zirconia nanofluid as a function of time. (B, C and D) Photographs of ceria, zirconia and alumina nanofluids (a) fresh and (b) after five months.

The transmittance of visible light decreased slightly by $\sim 7\%$ from initial of 42 to 39 NTU after 150 days of ageing for ceria nanofluid. The reduction in turbidity for alumina was 6% and for zirconia, turbidity remained constant during the measurement period. In this

regard the prepared nanofluids are surpassing the stability reported for oil based CeO₂ nanofluids (40 days), Cu and MoS₂ suspensions (20 days).^[7, 13, 18]

4.4.7 *Compilation of data on selected samples for comparison*

For a comparison, results on 0.08, ~0.23 and 0.7 vol% loaded nanofluids for all the three types of NPs (which was common to all systems) is tabulated below in Table 4.3. The nanofluids were found to follow the order;

A) **Thermal conductivity enhancement:** Alumina > Ceria > Zirconia

B) **Viscosity:** Alumina > Ceria > Zirconia

C) **Processing/refluxing time:** Alumina > Zirconia > Ceria

Table 4.3 Summarised data on the three nanofluid systems

System	Processing time (h)	Morphology	Thermal Conductivity (W.m ⁻¹ .k ⁻¹)					Viscosity (Pa.s)			
			Oil	Bulk oxide	Nanofluid Solid content (%)			Oil	Nanofluid Solid content (%)		
					0.08	0.23	0.7			0.08	0.23
Ceria	4	Cubic	0.137	12	6.5	7.3	10.3	0.019	0.0221	0.043	0.408
Alumina	24	Spherical		30	7	8.1	-		0.031	0.143	-
Zirconia	10	Elongated		2	5.1	5.6	7.3		0.023	0.03	0.0574

An efficient nanofluid is expected to give maximum thermal conductivity enhancement, minimum viscosity, good stability and minimum processing time for easy adaptation into industrial applications. The lower processing time (4 h reflux), low viscosity and TC enhancement comparable to that of alumina makes ceria a much better candidate in heat transport application.

4.5 Conclusions

A comparatively simple method for preparing well-dispersed NPs of ceramic oxides such as ceria, alumina and zirconia in oils is presented in this work. Surface modified NC's of cubic, spherical and rod like morphology have been successfully synthesised by the thermolysis of respective oleate precursor in ceria, alumina and zirconia systems. The particles are stabilized by oleic acid, which coordinates to the NP surface via the two oxygen atoms forming a dense layer around the particles. The surface functionalised nanocrystals are ideal for nanofluid preparation as they offer long term stability of about six months. The nanofluids showed Newtonian behaviour at low solid loading, showing the true colloidal nature of the solutions and it implies that the nanofluid is, for possible future applications, not likely to clog any flow channels in cooling devices. The thermal conductivity was measured as a function of NP concentration. An increase in thermal conductivity was observed with an increase in NP concentration. In general, the thermal conductivity of ~0.23 vol% nanofluid has shown 7.3, 8.1 and 5.6 % enhancements in thermal conductivity with respect to that of transformer oil in the case of ceria, alumina and zirconia respectively. Another interesting area of research we have attempted is the temperature dependence of thermal conductivity and viscosity of the nanofluids and it was found that thermal conductivity increased with increase in temperature whereas the viscosity decreased. The small size and compatibility of surface modified NPs with the base fluid might have contributed to the reasonably high thermal conductivity offered by nanofluids. Various characterisation techniques were employed to measure the physical, chemical, and thermal properties of the nanofluids by using TEM, XRD, particle size analyser, FT-IR, transient hot wire, and

viscometer. From the stability test, we confirmed that nanocrystals are well dispersed in TO over a long time period up to six months. It was also demonstrated that evaluation of nanofluids for a particular application requires a proper understanding of all the characteristics and thermophysical properties of nanoparticle suspensions. The transformer oil-based nanofluid containing surface modified NPs could possibly find use in transformers due to the higher thermal conductivity, good flow characteristics and the long-term stability. For the real world applications, a detailed study on the dielectric property of the nanofluids has to be carried out which is not included in the present study. For future applications, intensive research is therefore necessary in this particular field.

4.6 References

- [1] R. Si, Y. W. Zhang, L. P. You, C. H. Yan, *Angew. Chem. Int. Ed.* **2005**, *44*, 3256.
- [2] V. Sridhara, L. N. Satapathy, *Nanoscale Res. Lett.* **2011**, *6*, 1.
- [3] B. Wang, J. Hao, H. Li, *Dalton Trans.* **2013**, *42*, 5866.
- [4] T. S. Sreeremya, A. Krishnan, L. N. Satapathy, S. Ghosh, *Rsc Adv.* **2014**, *4*, 28020.
- [5] T. S. Sreeremya, A. Krishnan, A. P. Mohamed, U. S. Hareesh, S. Ghosh, *Chem. Eng. J.* **2014**, *255*, 282.
- [6] C. Choi, H. S. Yoo, J. M. Oh, *Curr. Appl. Phys.* **2008**, *8*, 710.
- [7] M. Kole, T. K. Dey, *Appl. Therm. Eng.* **2013**, *56*, 45.
- [8] Q. L. Yimin Xuan, *Int. J. Heat Fluid Fl.* **2000**, *21*, 58.
- [9] D. Li, B. Hong, W. Fang, Y. Guo, R. Lin, *Ind. Eng. Chem. Res.* **2010**, *49*, 1697.
- [10] P. D. Shima, J. Philip, B. Raj, *J. Phys. Chem. C* **2010**, *114*, 18825.
- [11] H. Q. Xie, J. C. Wang, T. G. Xi, Y. Liu, F. Ai, Q. R. Wu, *J. Appl. Phys.* **2002**, *91*, 4568.
- [12] M. S. L. Kundan, *Inter. J. Theoretical Appl. Res. Mech. Eng.* **2013**, *2*, 2319
- [13] Y.-X. Zeng, X.-W. Zhong, Z.-Q. Liu, S. Chen, N. Li, *J. Nanomater.* **2013**.
- [14] T. S. Sreeremya, A. Krishnan, S. J. Iyengar, S. Ghosh, *Ceram. Int.* **2012**, *38*, 3023.
- [15] T. S. Sreeremya, K. M. Thulasi, A. Krishnan, S. Ghosh, *Ind. Eng. Chem. Res.* **2012**, *51*, 318.

-
- [16] S. Ghosh, D. Divya, K. C. Remani, T. S. Sreeremya, *J. Nanopart. Res.* **2010**, *12*, 1905.
- [17] M. Brigante, P. C. Schulz, *Chem. Eng. J.* **2012**, *191*, 563.
- [18] D. Kim, Y. Hwang, S. I. Cheong, J. K. Lee, D. Hong, S. Moon, J. E. Lee, S. H. Kim, *J. Nanopart. Res.* **2008**, *10*, 1121.
- [19] M. P. Beck, Y. Yuan, P. Warriar, A. S. Teja, *J. Appl. Phys.* **2010**, *107*.
- [20] A. Krishnan, T. S. Sreeremya, E. Murray, S. Ghosh, *J. Colloid Interface Sci.* **2013**, *389*, 16.
- [21] F. Dang, K. Kato, H. Imai, S. Wada, H. Haneda, M. Kuwabara, *Cryst. Growth Des.* **2010**, *10*, 4537.
- [22] M. Inoue, M. Kimura, T. Inui, *Chem. Commun.* **1999**, 957.
- [23] A. Nugroho, B. Veriansyah, S. K. Kim, B. G. Lee, J. Kim, Y.-W. Lee, *Chem. Eng. J.* **2012**, *193*, 146.
- [24] H. L. Lin, C. Y. Wu, R. K. Chiang, *J. Colloid Interface Sci.* **2010**, *341*, 12.
- [25] L. M. Bronstein, X. Huang, J. Retrum, A. Schmucker, M. Pink, B. D. Stein, B. Dragnea, *Chem. Mater.* **2007**, *19*, 3624.
- [26] H. Gu, M. D. Soucek, *Chem. Mater.* **2007**, *19*, 1103.
- [27] S. Yobanny Reyes-Lopez, R. Saucedo Acuna, R. Lopez-Juarez, J. Serrato Rodriguez, *J. Ceram. Process. Res.* **2013**, *14*, 627.
- [28] S. Sakka, *Kluwer Academic Publishers*, 2.
- [29] L. F. Shen, P. E. Laibinis, T. A. Hatton, *Langmuir* **1999**, *15*, 447.
- [30] L. Zhang, R. He, H.-C. Gu, *Appl. Surf. Sci.* **2006**, *253*, 2611.
- [31] Z. L. Wang, *Kluwer Academic Plenum Publishers* **2002**.

- [32] M. Inoue, H. Tanino, Y. Kondo, T. Inui, *Clay. Clay. Miner.* **1991**, *39*, 151.
- [33] S. C. Tjong, H. Chen, *Mat. Sci. Eng. R.* **2004**, *45*, 1.
- [34] P. Dutta, S. Pal, M. S. Seehra, Y. Shi, E. M. Eyring, R. D. Ernst, *Chem. Mater.* **2006**, *18*, 5144.
- [35] A. Ahniyaz, Y. Sakamoto, L. Bergstrom, *Cryst. Growth Des.* **2008**, *8*, 1798.
- [36] A. Prakash, H. Zhu, C. J. Jones, D. N. Benoit, A. Z. Ellsworth, E. L. Bryant, V. L. Colvin, *ACS Nano* **2009**, *3*, 2139.
- [37] T. D. Schladt, T. Graf, W. Tremel, *Chem. Mater.* **2009**, *21*, 3183.
- [38] F. Kenfack, H. Langbein, *Thermochim. Acta* **2005**, *426*, 61.
- [39] M. Klokkenburg, J. Hilhorst, B. H. Erne, *Vibr. Spectrosc.* **2007**, *43*, 243.
- [40] Reiss, **1951**, *19*, 482.
- [41] D. K. Lee, Y. S. Kang, *ETRI J.* **2004**, *26*, 252.
- [42] S. S. Botha, P. Ndungu, B. J. Bladergroen, *Ind. Eng. Chem. Res.* **2011**, *50*, 3071.
- [43] P. G. Wright, *Phys. Edu.* **1977**, 323.
- [44] M. F. N. Jamshidi, D. D. Ganji, K. Sedighi, *IJE TRANSACTIONS B: Applications* **2012**, *25*, 201.
- [45] N. Shalkevich, A. Shalkevich, T. Buergi, *J. Phys. Chem. C* **2010**, *114*, 9568.
- [46] S. P. Jang, S. U. S. Choi, *Appl. Phys. Lett.* **2004**, *84*, 4316.
- [47] L. Chen, H. Xie, *Colloids Surf. A* **2009**, *352*, 136.
- [48] S. J. Obrey, A. R. Barron, *Macromolecules* **2002**, *35*, 1499.
- [49] Q. Liu, A. Wang, X. Wang, P. Gao, X. Wang, T. Zhang, *Microporous Mesoporous Mater.* **2008**, *111*, 323.

-
- [50] R. T. Tettenhorst, *Clay. Clay. Miner.* **1988**, *36*, 181.
- [51] S. Zhou, M. Antonietti, M. Niederberger, *Small* **2007**, *3*, 763.
- [52] Y. Q. Wu, Y. F. Zhang, X. X. Huang, J. K. Guo, *Ceram. Int.* **2001**, *27*, 265.
- [53] F. Mirjalili, M. Hasmaliza, L. C. Abdullah, *Ceram. Int.* **2010**, *36*, 1253.
- [54] J. K. Stolarczyk, S. Ghosh, D. F. Brougham, *Angew. Chem. Int. Ed.* **2009**, *48*, 175.
- [55] G. Stefanic, S. Music, *Croat. Chem. Acta* **2011**, *84*, 481.
- [56] J. Chandradass, K. H. Kim, *Mater. Manuf. Process.* **2009**, *24*, 541.
- [57] W. B. Bu, Z. Hua, H. R. Chen, J. L. Shi, *J. Phys. Chem. B* **2005**, *109*, 14461.
- [58] S. K. Chen, G. Oye, J. Sjoblom, *J. Disper. Sci. Technol.* **2005**, *26*, 791.
- [59] X. Xu, X. Wang, *Nano Res.* **2009**, *2*, 891.
- [60] E. F. Lopez, V. S. Escribano, M. Panizza, M. M. Carnasciali, G. Busca, *J. Mater. Chem.* **2001**, *11*, 1891.
- [61] P. Tartaj, O. Bomati-Miguel, A. F. Rebolledo, T. Valdes-Solis, *J. Mater. Chem.* **2007**, *17*, 1958.
- [62] M. Janus, M. Inagaki, B. Tryba, M. Toyoda, A. W. Morawski, *Appl. Catal. B* **2006**, *63*, 272.

Instrumental methods

Introduction: In this section the basic principles and instrumental details of various characterization techniques which are applied throughout the thesis will be described. Details of the syntheses are given in the relevant chapters.

Characterisation techniques

X-Ray diffraction (XRD): X-rays are electromagnetic radiation of wavelength $\sim 1\text{\AA}$ (10^{-10} m). X-rays are produced when high energy charged particles, e.g. electrons collide with matter. X-ray diffraction (XRD) is a versatile, non-destructive technique that reveals detailed information about the crystallographic structure, phases, in polycrystalline samples and other structural parameters such as average grain size, crystallinity, strain and crystal defects and chemical composition, and physical properties of materials and thin films. X-ray diffraction is based on constructive interference of monochromatic X-rays and a crystalline sample. The peak intensities are determined by the atomic arrangement within the lattice planes. The interaction of the incident rays with the sample produces constructive interference when conditions satisfy Bragg's Law,

$$n\lambda = 2d \sin \theta \quad (1)$$

where n is the order of diffraction, d is the interplanar spacing and θ is the angle of diffraction.

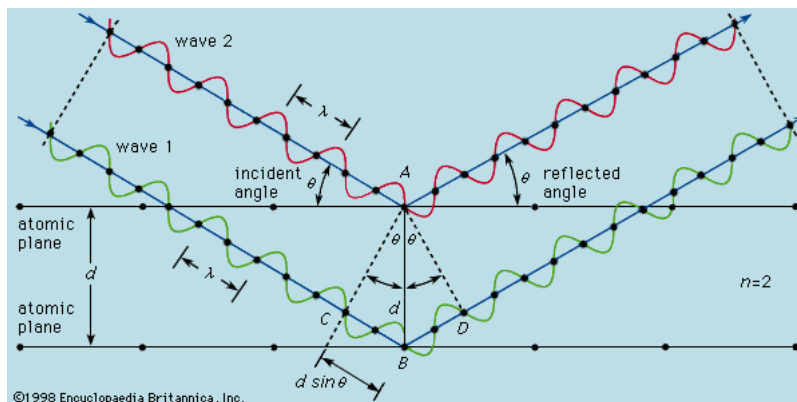


Fig. 1 A simplified view of the interaction of X-ray radiation and crystal planes to demonstrate Bragg's law.

By scanning the sample through a range of 2θ angles, all possible diffraction directions of the lattice should be attained due to the random orientation of the powdered material. Conversion of the diffraction peaks to d-spacings allows identification of the mineral because each mineral has a set of unique d-spacings. The crystallite size of the ceria powders was calculated from the Scherrer equation

$$D = \frac{0.9\lambda}{\beta \cos\theta} \quad (2)$$

The lattice parameter of the cubic crystal can be calculated from the position of the observed diffraction lines in the XRD pattern, according to the following relation,

$$a = \lambda \frac{\sqrt{(h^2 + k^2 + l^2)}}{2 \sin \theta} \quad (3)$$

where a is the lattice parameter and h, k, l are the Miller indices of the considered Bragg reflection. The phase composition of the solid products were determined from the powder X-ray diffraction patterns collected at room temperature using a Philips X'PERT PRO diffractometer with Ni-filtered $\text{Cu K}\alpha_1$ radiation ($\lambda = 1.5406 \text{ \AA}$). The X-ray data was

Instrumental methods

collected on oven dried powders in the 2θ range 20–100 degree at a scanning rate 2° min^{-1} with a step size 0.04° . Broadening of the X-ray diffraction peaks (Bragg peaks) is related to the average grain size and microstrain in the crystal lattice originating from defects. Particle size information was obtained by analysing the XRD peak widths using the Williamson-Hall (also known as Cauchy–Cauchy) procedure. This is in preference to the Scherrer approach, which underestimates grain size when there is significant microstrain in the lattice.

Surface area analysis: Gas sorption is a technique used for characterizing porous materials. With this method, specific surface area, pore volume and pore size distribution of powders and surfaces can be determined. The physisorption data is presented in sorption isotherms with the amount of gas adsorbed on the solid plotted versus the relative pressure. The surface area measurements were carried out by nitrogen adsorption using Micromeritics Gemini 2375 surface area analyzer, after degassing the sample at 200°C for 2h. Surface area values calculated by The Brunauer–Emmett–Teller (BET) method were reported.

Thermogravimetric analysis (TGA) is used to study mass changes in a material due to changes in temperature. TGA is commonly used to determine polymer degradation temperatures, residual solvent levels, absorbed moisture content, and to characterize both inorganic and organic materials. It is also often used to estimate the corrosion kinetics in high temperature oxidation. The sample is placed on a high-precision balance and subsequently heated following a given temperature program. Varying atmospheres such as air, argon or helium can be used depending on the purpose of the measurement. During the heating, the sample weight is plotted against temperature. Thermogravimetric studies

of the powders were carried out using a Perkin Elmer, STA 6000 thermogravimetric analyser (TGA) in ambient atmosphere heated at a constant rate of $10\text{ }^{\circ}\text{C min}^{-1}$ under air purge.

Infrared spectroscopy (IR spectroscopy) is the subset of spectroscopy that deals with the infrared region of the electromagnetic spectrum. Fourier transformed infrared spectroscopy (FT-IR) is used to study functional groups in compounds using the discrete energy levels for vibrations of atoms in these groups. When light with a specific energy is transmitted through the sample it can be absorbed by groups of atoms in the material. This occurs when the frequency of the incoming light corresponds to the frequency of vibrations in bonds between atoms. The vibration energy depends on the masses, chemical environment of the atoms and the type of vibration. By scanning over a range of wavelengths (in this case $400\text{-}4000\text{ cm}^{-1}$) and recording the amount of transmitted light for each wavelength it is possible to determine which functional groups are present on the surface of the material. Fourier transform infrared (FTIR) spectra of the as prepared products were recorded at room temperature using the KBr (Sigma Aldrich, g 99%) pellet method on a Nicolet Magna IR-560 spectrometer ranging from $400\text{ to }4000\text{ cm}^{-1}$ with 50 scans.

Transmission electron microscopy is used to characterize the microstructure of materials with very high spatial resolution ($\sim 1\text{ \AA}$). Information about the morphology, crystal structure and defects, crystal phases and composition, and magnetic microstructure can be obtained by a combination of electron-optical imaging, electron diffraction, and small probe capabilities. A beam of electrons is transmitted through a thin sample and the electrons are scattered in the specimen. The transmitted electrons are

focused on a fluorescent screen or CCD camera by electromagnetic coils and the image is formed. The image contrast originates from mass-thickness differences where thicker regions of the specimen (in this case the silica walls) absorb or scatter more electrons compared to thinner regions. The morphology and average size of the ceria NPs were observed by TEM carried out in HR-TEM (FEI Tecnai 30 G² S-Twin) operated at 300 kV. Samples for TEM study were prepared by dropping a micro droplet of suspension of nanopowder in acetone on to a 400 mesh carbon-coated copper grid and drying the excess solvent naturally. In the case of surface modified NPs, instead of acetone, a small amount of capped NPs was dispersed in toluene and ultrasonicated to get a stable suspension.

Scanning electron microscope (SEM) is used to study the topography of glass slides included in the polishing study. An electron probe is scanning over the surface of the material and these electrons interact with the material. Secondary electrons emitted from the surface of the specimen were recorded. The height differences in the sample give contrast in the image. The surface quality of glass slides were examined using scanning electron microscope (JEOL-JSM-5600LV, Japan) operated at 15 kV.

Atomic force microscopy (AFM) is a very high-resolution type of scanning probe microscopy, with demonstrated resolution of fractions of a nanometer, more than 1000 times better than the optical diffraction limit. The AFM consists of a cantilever with a sharp tip (probe) at its end that is used to scan the specimen surface. This tip is scanned over a surface with feedback mechanisms that enable the piezo-electric scanners to maintain the tip at a constant force (to obtain height information), or height (to obtain force information) above the sample surface. Tips are typically made from Si₃N₄ or Si, and extended down from the end of a cantilever. The nanoscope AFM head employs an

optical detection system in which the tip is attached to the underside of a reflective cantilever. A diode laser is focused onto the back of a reflective cantilever. As the tip scans the surface of the sample, moving up and down with the contour of the surface, the laser beam is deflected off the attached cantilever into a dual element photodiode. The photo detector measures the difference in light intensities between the upper and lower photo detectors, and then converts to voltage. Feedback from the photodiode difference signal, through software control from the computer, enables the tip to maintain either a constant force or constant height above the sample. In the constant force mode the piezoelectric transducer monitors real time height deviation. In the constant height mode the deflection force on the sample is recorded. The latter mode of operation requires calibration parameters of the scanning tip to be inserted in the sensitivity of the AFM head during force calibration of the microscope. The surface roughness analyses of the glass slide before and after polishing were done with a I120 Taylor Hobson surface profilometer and the AFM analysis was carried out using an AFM instrument NTEGRA (NTMDT) using microfabricated TiN cantilever tips (NSG-10) with a resonating frequency of 299 kHz and a spring constant of 20–80 N m⁻¹ and a multimode scanning probe microscope (Nanoscope IV controller, digital instruments), using tapping mode techniques. 2D surface roughness analysis was performed using the raw AFM images obtained. Five measurements were used to compute the average surface roughness of each sample.

Raman spectroscopy is a spectroscopic technique based on inelastic scattering of monochromatic light, usually from a laser source. Inelastic scattering means that the frequency of photons in monochromatic light changes upon interaction with a sample.

Instrumental methods

Photons of the laser light are absorbed by the sample and then reemitted. Frequency of the reemitted photons is shifted up or down in comparison with original monochromatic frequency, which is called the Raman effect. This shift provides information about vibrational, rotational and other low frequency transitions in molecules. Raman spectroscopy can be used to study solid, liquid and gaseous samples. Raman spectra were taken using a HR800 LabRAM confocal Raman spectrometer having excitations by a 20 mW, 633 nm He–Ne laser. The spectrum was recorded using a Peltier cooled CCD detector with an acquisition time of 10 s using a 5× objective.

X-ray Photoelectron Spectroscopy (XPS), also known as ESCA, is the most widely used surface analysis technique because of its relative simplicity in use and data interpretation. The sample is irradiated with mono-energetic x-rays causing photoelectrons to be emitted from the sample surface. An electron energy analyzer determines the binding energy of the photoelectrons. From the binding energy and intensity of a photoelectron peak, the elemental identity, chemical state, and quantity of an element are determined. The information XPS provides about surface layers or thin film structures is of value in many industrial applications including: polymer surface modification, catalysis, corrosion, adhesion, semiconductor and dielectric materials, electronics packaging, magnetic media, and thin film coatings used in a number of industries. X-ray photoelectron spectra (XPS) for nanosized CeO₂ powders were recorded on VG Microtech Multilab ESCA 3000 spectrometer maintaining a base pressure of the analysis chamber in the range of 3–6×10⁻¹⁰ Torr. Mg Kα (1253.6 eV) was used as the X-ray sources. Selected spectra, especially N 1s and valence band spectra were recorded to eliminate the overlap between different Auger and/or core levels. Binding energy (BE)

Instrumental methods

calibration was performed with Au $4f_{7/2}$ core level at 83.9 eV. The spectrum was recorded using a Peltier cooled CCD detector with an acquisition time of 10 s using a 5× objective.

Nephelometer is an instrument for measuring concentration of suspended particulates in a liquid or gas colloid. A nephelometer measures suspended particulates by employing a light beam (source beam) and a light detector set to one side (often 90°) of the source beam. Particle density is then a function of the light reflected into the detector from the particles. To some extent, how much light reflects for a given density of particles is dependent upon properties of the particles such as their shape, colour, and reflectivity. The colloidal stability of the polishing slurry was monitored with a nephelometer (CL 52D, ELICO, India) as intensity of transmitted visible light through the fluid against of time. The colloidal stability of the nanofluids was also monitored with the nephelometer by measuring turbidity as a function of time.

Photon Correlation Spectroscopy (PCS) Laser diffraction is used to measure particle size distribution by measuring the angular variation in intensity of light scattered as a laser beam passes through a dispersed particulate sample. Large particles scatter light at small angles relative to the laser beam and small particles scatter light at large angles. The angular scattering intensity data is then analyzed to calculate the size of the particles responsible for creating the scattering pattern, using the Mie theory of light scattering. The particle size is reported as a volume equivalent sphere diameter. For hydrodynamic size measurement, a small amount of CeO₂ powder was ground well with few drops of water, dispersed in water, stirred mechanically and ultrasonicated to produce a

Instrumental methods

suspension. The pH of the CeO₂ suspension was raised above 10 for achieving a stable suspension (Zeta potential > -35 mV).

Contact angle measurements: The dynamic water contact angle of the polished glass slides and powders were measured using Data Physics DCAT 21 Dynamic contact angle meter and Tensiometer. The dynamic contact angle analyzer operates by holding a glass slide in a fixed vertical position attached to a microbalance and moving a test liquid (water) contained in a vessel at constant rate up.

Thermal conductivity: The nanofluid effective thermal conductivity (k_{eff}) was measured using a thermal property analyzer (model KD2pro, Decagon Devices, Inc.) based on the transient hot wire method. Accuracy in the k measurement is within 5%.



Fig. 2 Optical photograph of a KD2 Pro thermal conductivity meter in which a platinum hot wire is immersed in the nanofluid which acts as both the heater and temperature sensor.

Instrumental methods

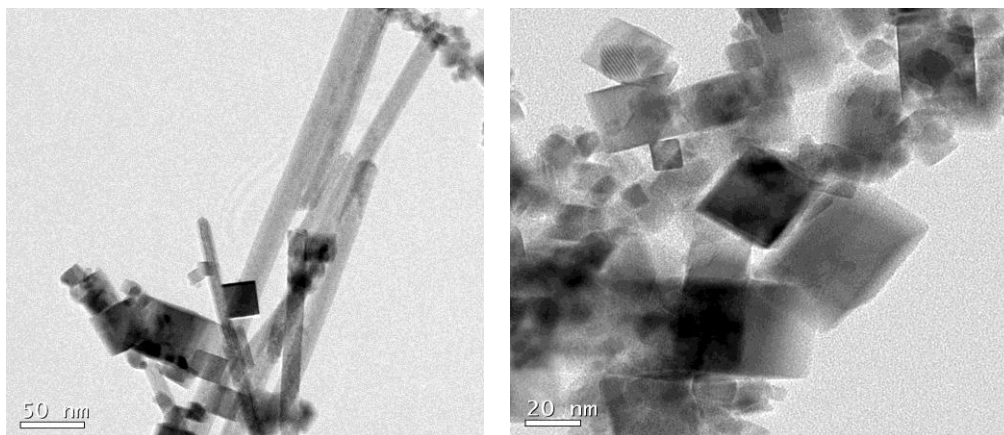
To measure the thermal conductivity at different temperatures, the sample vial with the thermal conductivity probe was immersed in a circulating water bath and the temperature of the water bath was maintained within 0.1 °C. The entire sample assembly was insulated for temperature gradient and vibrations. The thermal conductivity measurements were made 10 min after achieving the desired temperature for better temperature equilibrium.

Viscosity measurements: The apparent viscosity of nanofluids was measured using a Physica rotational-type viscometer with the SC4–18 spindle (Rheolab_ MC1vt2 rheometer) employing the concentric cylinder/bob and cup method.

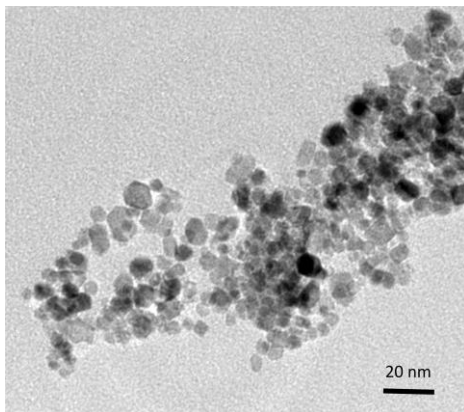
Summary

Summary of investigations

Nano cerium dioxide is an efficient inorganic oxide by virtue of its applications in vivid areas. Cerium dioxide or ceria, CeO_2 , has been widely used in industry as catalyst for automotive exhaust controls, chemical mechanical polishing (CMP) slurries, and high temperature fuel cells because of its unique metal oxide properties. This well-known rare metal oxide has high thermal stability, electrical conductivity and chemical diffusivity. Proper synthesis method requires knowledge of reaction temperature, concentration, and time effects on the synthesis. The present thesis employed hydrothermal cum precipitation approach starting from cerium nitrate hexahydrate for the synthesis of morphologically diverse nanostructures of cerium dioxide. Further, a facile reflux method in presence of oleic acid surfactant was utilized for the synthesis of oleophilic/surface modified ceria nanoparticles.



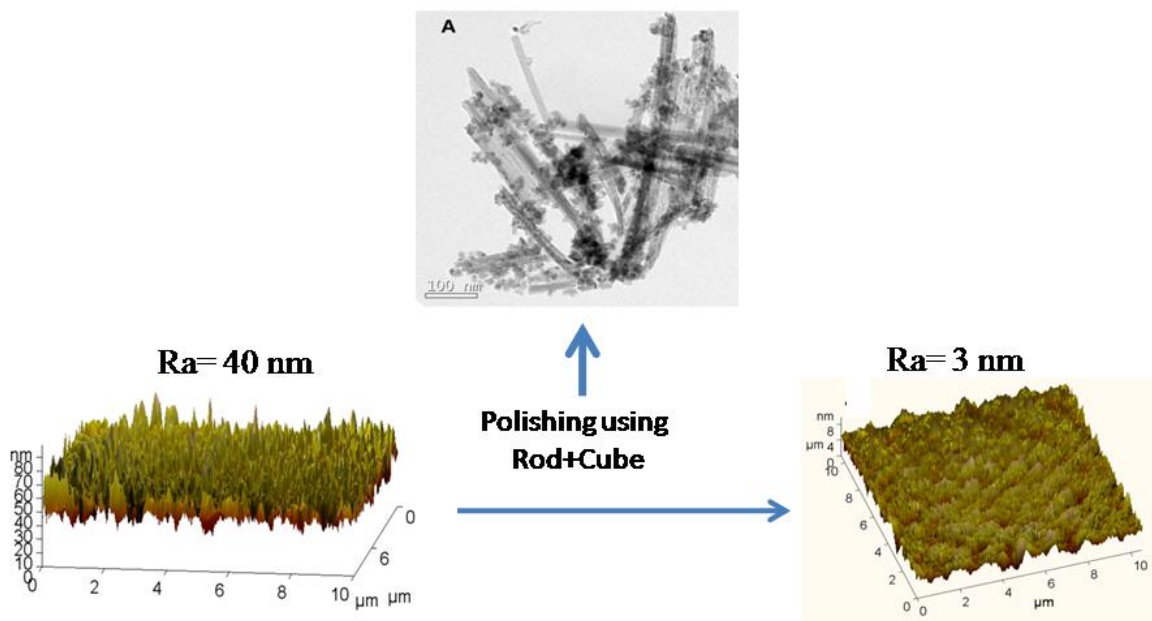
Summary



TEM images of rods, cubes and spherical particles of ceria synthesized by varying reaction parameters in hydrothermal cum precipitation approach.

In the present thesis, the effect of nanoparticle morphology on multifunctional applications such as glass polishing and also in oxidation catalysis is studied in detail. The use of ceria NPs in glass polishing and effect of several parameters such as crystallite size, abrasive solid content in slurry, pH etc has been studied earlier. Here, we have made an attempt to unravel the effect of particle morphology and the underlying mechanisms in glass polishing, an area which is not well covered in literature. The prepared nanoparticles were utilised for the fine polishing of silicate glass with an initial surface roughness of 40 nm and observed a strong morphology dependence of abrasive in glass polishing. Surface roughness analysis by Atomic Force Microscopy reveals that the ceria nanostructure with mixed morphology of rods and cubes could produce a surface finish of ~3 nm.

Summary



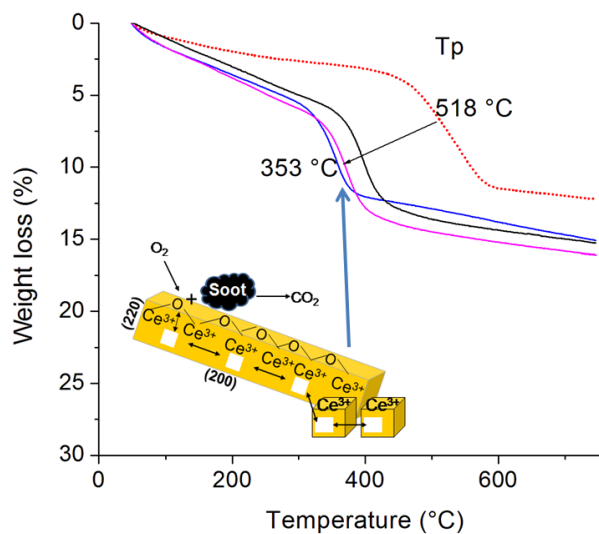
AFM images of glass before ($R_a=40$ nm) and after polishing using a mixed morphology abrasive of rod and cube ($R_a=3$ nm).

The surface properties of abrasive were found to play a key role in polishing as evidenced by X-ray Photoelectron Spectroscopy and Raman spectral analysis. The powder contact angle/hydrophilicity of the nanopowders followed the same trend as that of dipolar (200) plane and $[\text{Ce}^{3+}]$. This work has shown the promise for polishing efficiency with nano CeO_2 slurry in achieving nanolevel planarity on glass substrates which is desirable for the global planarisation of complex device topography.

Further the catalytic performance of a range of nanocrystalline CeO_2 samples, prepared to have different morphologies, was measured using two accepted indicators; oxygen storage and diesel soot combustion. The same powders were characterised in detail by HR-TEM, XRD, XPS and Raman methods. The study demonstrates that activity

Summary

is determined by the relative fraction of the active crystallographic planes, not by the specific surface area of the powders.



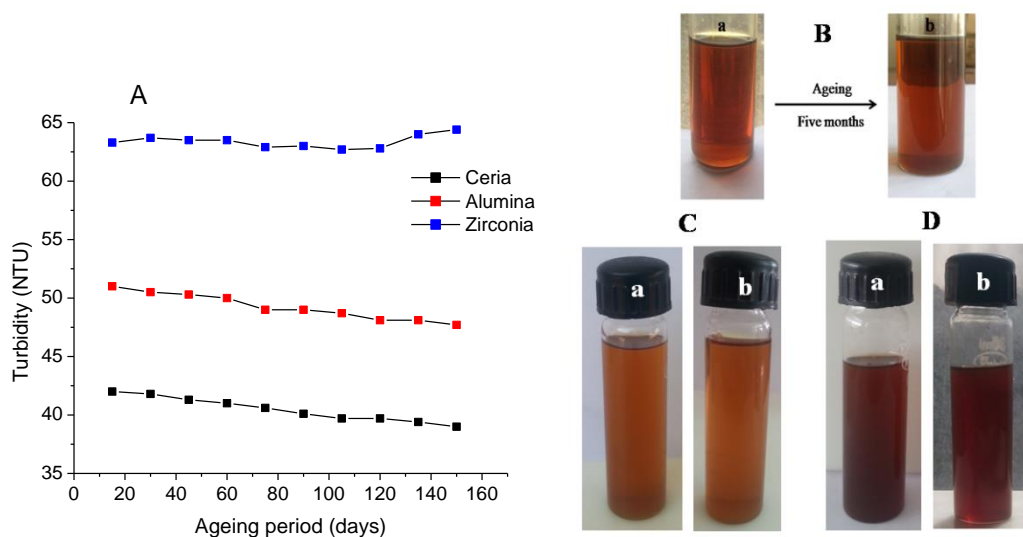
Thermogravimetric profiles of diesel soot with and without ceria nanocatalysts of various morphologies. The mixed morphology catalyst could reduce the soot oxidation temperature from 518 to 353°C.

The physical study is a step towards quantitative evaluation of the relative contribution to activity of the different facets. The synthetic protocol permits fabrication of CeO₂ nanostructures with preferentially grown active planes, and so has potential in developing catalytic applications and in nano-compositing.

In the last chapter, a comparatively simple method for preparing well-dispersed NPs of ceramic oxides such as ceria, alumina and zirconia in oils was presented. Surface modified NC's of cubic, spherical and rod like morphology have been successfully synthesized by the thermolysis of respective oleate precursor in the case of ceria, alumina and zirconia respectively. The particles are stabilized by oleic acid, which coordinates to

Summary

the NP surface via the two oxygen atoms forming a dense layer around the particles. The surface functionalized nanocrystals are ideal for nanofluid preparation as they offer long term stability of about five months. The nanofluids showed Newtonian behavior at low solid loading, showing the true colloidal nature of the solutions and it implies that the nanofluid is, for possible future applications, not likely to clog any flow channels in cooling equipment. The thermal conductivity was measured as a function of NP concentration. An increase in thermal conductivity was observed with an increase in NP concentration. In general, the thermal conductivity of 0.23 vol% nanofluid has shown 7.3, 8.1 and 5.6 % enhancement in thermal conductivity with respect to that of transformer oil in the case of ceria, alumina and zirconia respectively.



(A) Ageing studies which involve the measurement of turbidity over a time period of five months. Optical photographs of ceria, alumina and zirconia nanofluids initially and after five months is also shown indicating the extreme stability.

Another interesting area of research we have attempted is the temperature dependence of thermal conductivity and viscosity of the nanofluids and it was found that thermal conductivity increased with increase in temperature whereas the viscosity decreased. The

Summary

small size and compatibility of surface modified NPs with the base fluid may have contributed to the reasonably high thermal conductivity offered by nanofluids. From the stability test, we confirmed that nanocrystals are well dispersed in TO over a long time period up to six months. It was also demonstrated that evaluation of nanofluids for a particular application requires a proper understanding of all the characteristics and thermophysical properties of nanoparticle suspensions. The transformer oil-based nanofluid containing surface modified NPs could possibly find use in transformers due to the higher thermal conductivity, good flow characteristics and the long-term stability. For real world applications, a detailed study on the dielectric property of the nanofluids has to be carried out which is not included in the present study. For future applications, more intensive research is therefore necessary in this particular field.

LIST OF PUBLICATIONS

1. Synthesis and characterization of cerium oxide based nanofluids: An efficient coolant in heat transport Applications, Thadathil S. Sreeremya et al., **Chem. Eng. J.** (2014), DOI: 10.1016/j.cej.2014.06.061.
2. Facile synthetic strategy of oleophilic zirconia nanoparticles allows preparation of highly stable thermo-conductive coolant, Thadathil S. Sreeremya, et al., **RSC Adv.**, (2014), DOI: 10.1039/c4ra03270e.
3. One-pot synthesis of ultra-small cerium oxide nanodots exhibiting multi-colored fluorescence, Asha Krishnan, Thadathil S. Sreeremya et al., **J. Colloid Interf. Sci.** 389 (2013) 16–22.
4. A Novel Aqueous Route To Fabricate Ultrasmall Monodisperse Lipophilic Cerium Oxide Nanoparticles, Thadathil S. Sreeremya et al., **Ind. Eng. Chem. Res.** 2012.
5. Ultra-thin cerium oxide nanostructures through a facile aqueous synthetic strategy, Thadathil S. Sreeremya, et al., **Ceram. Int.**, 38 (2012) 3023–3028.
6. Growth of monodisperse nanocrystals of cerium oxide during synthesis and annealing, S. Ghosh, D. Divya, K. C. Remani and T. S. Sreeremya, **J. Nanopart. Res.**, 12 (5) (2010) 1905-11.
7. Shape Selective Oriented Cerium Oxide Nanocrystals Permit Assessment of the Effect of the Exposed Facets on Catalytic Activity and Oxygen Storage Capacity, Thadathil S. Sreeremya et al. (**Communicated**)
8. Tailoring the surface properties of ceria nanoabrasives for silica glass CMP through morphology controlled synthesis, Thadathil S. Sreeremya et al. (**Communicated**)

Patent Filed

1. Lakshmi Narayan Satapathy, Sadanand Achari, Ceramic Technological Institute, Bharat Heavy Electrical Limited and Swapankumar Ghosh, **Ms T. S. Sree Remya** “*A novel method of producing stable zirconia based nanofluids in non-polar solvent*”, **File No: 1584/Kol/2011, Filing date 23-12-2011.**

Conference Proceedings

1. Poster entitled “Zirconia nanofluid: An efficient coolant in transformers” **Thadathil S. Sreeremya** et al. presented in the International Conference on Advanced Functional Materials, February 2014, Trivandrum.
2. Poster entitled “Cerium oxide nanoplates and nanoribbons through green synthetic strategy”, **Thadathil S. Sreeremya**, et al., presented in the ‘National Conference on Science, Technology and Applications of Rare Earths 2011, during August 19-20, 2011 (STAR 2011), Munnar.
3. Oral presentation entitled “Cerium Oxide Based Slurry for CMP Applications”, **Thadathil S. Sreeremya**, et al., presented in the 74th ICS Conference, January 11-13th 2011, Kolkata.
4. Oral presentation entitled “Shape controlled synthesis of nanosized cerium oxide crystals and its characterization” **Thadathil S. Sreeremya**, et al., 73rd InCerS Conference, India, December 11-12, 2010, Trivandrum.
5. Oral presentation entitled “Surfactant capped monodisperse ceria nanoparticles by facile aqueous precipitation method, **Thadathil S. Sreeremya**, et al., International Conference on Recent Trends in Materials Science and Technology, October 29-31, 2010, Trivandrum.
6. Poster entitled “Particle size measurements: Importance and difficulties with particles in nanorange”, Kottayilpadi C. Remani, **Thadathil S. Sreeremya** and Swapankumar Ghosh, 97th Indian Science Congress, January 3-7, 2010, Trivandrum.
7. Poster entitled “Combustion Synthesis and Characterization of Nanocrystalline cerium oxide”, **Thadathil S. Sreeremya**, et al., International Conference on Advanced Functional Materials (ICAFM), December 9-10, 2009, Trivandrum.